REMOTE SENSING FOR ATMOSPHERIC OBSERVATION AND WIND ENERGY: OVER-LAND BOUNDARY LAYER AND OFF-SHORE ATMOSPHERIC STABILITY

Thesis submitted to the Universitat Politècnica de Catalunya
in partial fulfilment for the degree of

Doctor of Philosophy

Marcos Paulo Araújo da Silva

CommSensLab – Remote Sensing Lab.
Department of Signal Theory and Communications

Doctorate program in Signal Theory and Communications

Supervisor: Prof. Francesc Rocadenbosch Burillo

Barcelona, June 2023

Dedicado a mi muy amada familia.

First of all, thanks God for standing my spirit and for giving me strength to overcome the life's obstacles.

My immense gratitude to my family, in particular, Dona Liu, Cassiana, Marcello, Mácio and Andria, for their continuous and unconditional support during my whole life. I specially acknowledge my mother, Cassiana, who always encouraged me to pursue a Ph.D. abroad and my grandmother, Dona Liu, for her wise advises. With you two I learned the essential principles for living, something that no University in the world can teach.

My special gratitude and apologies to my wife, Ana, for tolerating my frequent absences due to work-related travels and deadlines. Furthermore, thanks for leaving everything behind to move to Barcelona with me, and also for drawing some figures used in this thesis.

My sincere thanks to my Ph.D. advisor Prof. Francesc Rocadenbosch for providing continuous support, guidance, and motivation throughout the duration of this Ph.D. His role has been fundamental at every stage of this Ph.D. thesis to keep me focused and productive.

Special thanks to my friend Andreu Salcedo Bosch for his great help throughout my Ph.D, and for his essential partnership inside and outside the academic world. Lastly, thanks to my colleagues Paulo and Simara, who gifted me a very useful office desk.

En primer lugar, agradezco a Dios por sostener mi espíritu y por darme fuerzas para superar los obstáculos de la vida.

Mi inmensa gratitud a mi familia, en particular a Dona Liu, Cassiana, Marcello, Mácio y Andria, por su continuo e incondicional apoyo durante toda mi vida. Agradezco especialmente a mi madre, Cassiana, que siempre me animó a realizar un Ph.D. en el extranjero y a mi abuela, Dona Liu, por sus sabios consejos. Con ustedes dos aprendí los principios esenciales para vivir, algo que ninguna universidad en el mundo puede enseñar.

Mi especial gratitud y disculpas a mi esposa, Ana, por tolerar mis frecuentes ausencias debido a viajes y fechas de entrega relacionadas con el trabajo. Además, gracias por dejar todo atrás para mudarse a Barcelona conmigo, y también por dibujar algunas figuras utilizadas en esta tesis.

Mi más sincero agradecimiento a mi orientador Prof. Francesc Rocadenbosch por brindar apoyo, orientación y motivación continuos a lo largo de la duración de este doctorado. Su papel ha sido fundamental en todas las etapas de este Ph.D. para mantenerme concentrado y productivo.

Un agradecimiento especial a mi amigo Andreu Salcedo Bosch por su gran ayuda a lo largo de mi doctorado y por su colaboración esencial dentro y fuera del mundo académico. Por último, gracias a mis colegas Paulo y Simara, que me regalaron una mesa de oficina muy útil.

Acknowledgements

The following institutions are gratefully acknowledged for their contribution to this work:

- This research project was part of projects PID2021-126436OB-C21 and PGC20 18-094132-B-I00 funded by Ministerio de Ciencia e Investigación (MCIN)/Agencia Estatal de Investigación (AEI) / 10.13 039/501100011033 / FEDER "Una manera de hacer Europa" and MDM-2016-0600 by MCIN/AEI.
- CommSensLab-UPC was awarded María-de-Maeztu (MDM) Excellence Unit (MDM-2016-0600, 1/7/2017-30/6/2021) funded by the Agencia Estatal de Investigación, Spain.
- The work of M.P Araújo da Silva was supported under MDM Grant PRE2018-086054 funded by MCIN/AEI/10.13039/5011000 11033, and FSE "El FSE invierte en tu futuro".
- The European Commission collaborated under projects H2020 ATMO-ACCESS (GA-101008004) and H2020 ACTRIS-IMP (GA-8711-15). The European Institute of Innovation and Technology (EIT), KIC InnoEnergy project NEPTUNE (Offshore Metocean Data Measuring Equipment and Wind, Wave and Current Analysis and Forecasting Software, call FP7), supported the PdP and Ijmuiden offshore measurement campaigns.
- Prof. Jakob Mann and Senior Scientist Alfredo Peña (Denmark Technical University, DTU; Department of Wind and Energy Systems · Meteorology and Remote Sensing · Wind Energy Systems Division) are gratefully acknowledged for hosting M. P. Araújo da Silva during his Ph.D. secondments.
- UPC-LIM lead PdP and Ijmuiden offshore measurement campaigns in the framework of European project NEPTUNE (partners: Catalonia Energy Research Institute (IREC), Remote Sensing

Lab. (RSLAB, today CommSensLab - UPC), Maritime Engineering Laboratory (LIM, UPC), Gas Natural Fenosa, CIEMAT, University of Stuttgart, Soluciones de Ingeniería Marítima Operacional, S.L. (SIMO)). EOLOS Floating Lidar Solutions is a sucessful spin-off from NEPTUNE.

- Dr. Robin L. Tanamachi, Department of Earth, Atmospheric, and Planetary Sciences, Purdue University, IN, USA contributed scientific assessment to the "over-land boundary-layer" research part of this Ph.D.
- Dr. Dave Turner (Global Systems Laboratory/Earth System Research Laboratories/NOAA, Boulder, CO, USA) provided key scientific insights regarding the Doppler Wind lidar and the AERI instrument.
- Over-land data were provided by Jülich Observatory for Cloud Evolution (JOYCE-CF), a core facility (CF) funded by Deutsche Forschungsgemeinschaft via Grant DFG LO 901/7-1. Dr. J. H. Schween and Prof. S. Crewell are thanked for the stay of U. Saeed at the Institute for Geophysics and Meteorology, University of Cologne, and data provision.

Abstract

Monitoring the atmospheric boundary layer (ABL) is a matter of interest for many applications, such as weather forecasting, pollutant-dispersion models and wind energy. The ABL is the most turbulent part of the troposphere, and it is directly affected by the earth's surface characteristics. Thus, monitoring the ABL is a complex task that requires continuous improvement of the remote sensing techniques.

This PhD thesis tackles remote sensing as the key technology to assess different ABL parameters in both over-land and over-sea dimensions. The over-land dimension is oriented to the study of the ABL height (ABLH), whereas the over-sea dimension is focused in assessment of surface-layer atmospheric stability from solely wind profiles in the context of wind energy.

In the over-land dimension, a synergistic ABLH estimation method via a combination of microwave-radiometer and lidar-ceilometer-based estimates is presented. The synergistic method uses these two instruments in a cooperative way with the aim of providing an enhanced high-resolution ABLH estimation. Data gathered by multiple remote-sensing instruments during the HOPE campaign at Jülich, Germany, are used to outline the robustness of the synergistic method in relation to estimates which rely on a single instrument.

In the over-sea dimension, the 2D parametric-solver algorithm is presented as an alternative method to assess surface-layer parameters from solely floating Doppler wind lidar measurements. Comparative results with reference retrievals from the IJmuiden meteorological mast show that the 2D accurately estimates the friction velocity, and it correctly determines atmospheric stability via its Obukhov length estimation. Accordingly, the 2D algorithm corroborates to stand the floating Doppler wind lidar as the wind-energy-industry preferred solution to replace the off-shore metmast.

Resumen

La observación de la capa límite de la atmósfera es de interés en diferentes aplicaciones como predicciones meteorológicas, energía eólica y modelos de dispersión de partículas contaminantes. Esta capa es la más turbulenta de la troposfera y recibe el efecto directo de la superficie terrestre. Por lo tanto, su observación es una tarea compleja y requiere una mejora continua de las herramientas de teledetección.

Esta tesis doctoral explota la teledetección como tecnología clave para estimar diferentes parámetros de la capa límite tanto en zonas marítimas como terrestres. En el contexto terrestre se investiga la medida de la altura de la capa límite y en el marítimo se estudia la estimación de la estabilidad atmosférica con solo medidas de perfiles verticales de viento.

En cuanto al contexto terrestre, se propone un método sinergético para estimar la altura de la capa límite combinando radiómetros de microondas y ceilómetros lidar. El método sinergético utiliza estos dos instrumentos cooperativamente para conseguir estimaciones de alta resolución de la altura de la capa límite. Para validar la robustez del método se han empleado datos medidos por instrumentos de teledetección durante la campaña de medidas HOPE en Jülich, Alemania, utilizando radiosondeos como referencia.

En cuanto al contexto marítimo, se presenta el algoritmo paramétrico ”2D” como método alternativo para estimar diferentes parámetros de la capa superficial de la atmósfera a partir de medidas del perfil vertical de viento de LiDARs Doppler flotantes. Usando como referencia medidas del mástil meteorológico IJmuiden, se ha podido validar la capacidad del método 2D para poder estimar con precisión la ”friction velocity” así como para clasificar la estabilidad atmosférica a partir de estimaciones de la longitud de ”Obukhov”. Así pues, el algoritmo 2D refuerza la posición de los LiDAR Doppler flotantes como tecnología clave para reemplazar los mástiles meteorológicos marítimos.

Resum

L'observació de la capa límit de l'atmosfera és d'interès per diferents aplicacions com ara en prediccions meteorològiques, en energia eòlica i en models de dispersió de partícules contaminants. Aquesta capa és la més turbulenta de la troposfera i rep l'efecte directe de la superfície terrestre. Per tant, la seva observació és una tasca complexa i requereix una millora contínua de les eines de teledetecció.

Aquesta tesi doctoral explota la teledetecció com a tecnologia clau per estimar diferents paràmetres de la capa límit tant en zones marítimes com terrestres. En el context terrestre s'estudia la mesura de l'alçada de la capa límit i en el marítim s'adreça l'estimació de l'estabilitat atmosfèrica amb només mesures de perfils verticals de vent.

Pel que fa al context terrestre, es proposa un mètode sinergètic per estimar l'alçada de la capa límit combinant radiòmetres de microones i ceilòmetres lidar. El mètode sinergètic utilitza aquests dos instruments cooperativament per aconseguir estimacions d'alta resolució de l'alçada de la capa límit. Per validar la robustesa del mètode s'han emprat dades mesurades per instruments de teledetecció durant la campanya de mesures HOPE a Jülich, Alemanya, utilitzant radio sondejos com a referència.

Pel que fa al context marítim, es presenta l'algorisme paramètric "2D" com a mètode alternatiu per estimar diferents paràmetres de la capa superficial de l'atmosfera a partir de mesures del perfil vertical de vent de LiDARs Doppler flotants. Fent servir com a referència mesures del màstil meteorològic IJmuiden, s'ha pogut validar la capacitat del mètode 2D per poder estimar amb precisió la "friction velocity" així com per classificar l'estabilitat atmosfèrica a partir d'estimacions de la longitud d'"Obukhov". Així doncs, l'algorisme 2D reforça la posició dels LiDAR Doppler flotants com a tecnologia clau per a reemplaçar els màstils meteorològics marítims.

Contents

List of Figures

List of Tables

List of Symbols

α	Charnock's constant
κ	Von Kármán constant
ρ	Coefficient of correlation
ρ^2	Coefficient of determination
θ	Potential temperature
θ_v	Virtual potential temperature
g	Gravitational acceleration
L	Obukhov length
P	Pressure
q	Mixing ratio
T	Temperature
T_b	Brightness temperature
U	Horizontal wind speed
u_*	Friction velocity
z	Height
z_0	Roughness length

Abbreviations and Acronyms

ABL Atmospheric Boundary Layer. xxviii

ABLH Atmospheric Boundary Layer Height. xxviii

CBH Cloud base height. xxviii

CBL Convective boundary layer. xxviii

DBS Doppler Beam Swing. xxviii, 17

DoF Degrees of Freedom. xxviii

DTU Denmark Technical University. xxviii, 1

DWL Doppler Wind LiDAR. xxviii

EKF Extended Kalman filter. xxviii, 18

ETT Evening transition time. xxviii

EZ Entrainment zone. xxviii

FDWL Floating Doppler Wind LiDAR. xxviii

FT Free troposphere. xxviii

HOPE HD(CP)^2 Observational Prototype Experiment. xxviii

HWS Horizontal Wind Speed. xxviii, 26

IEA International Energy Agency. xxviii

IEA Wind TCP IEA Wind Technology Collaboration Programme. xxviii, 4

IMU Inertial Measurement Unit. xxviii, 30

ITARS Initial Training for Atmospheric Remote Sensing. xxviii, 1

JOYCE Jülich ObservatorY for Cloud Evolution. xxviii

KPI Key Performance Indicators. xxviii

LAT Lowest Astronomical Tide. xxviii, 28

LC Lidar ceilometer. xxviii

LCoE Levelized Cost of Energy. xxviii

LiDAR Light Detection and Ranging. xxviii

LoS Line of Sight. xxviii, 25, 31

metmast Meteorological Mast. xxviii, 4

ML Mixed layer. xxviii

MLH Mixed layer height. xxviii

MTT Morning transition time. xxviii

MWR Microwave radiometer. xxviii, 14

PdP Pont del Petroli. xxviii

PSD Power Spectral Density. xxviii

RL Residual layer. xxviii

RS Root-mean-squared error. xxviii

RS Radiosonde. xxviii, 2, 14

SNR signal-to-noise ratio. xxviii

SYN Synergistic method. xxviii

VAD Velocity Azimuth Display. xxviii, 17, 26

VVSTD Vertical Velocity Standard Deviation. xxviii

VWS Vertical wind speed. xxv, xxviii, 31

WD Wind Direction. xxviii

WRS Weather Research and Forecasting. xxviii

WTG Wind Turbine Generator. xxviii

Chapter 1

Introduction

This chapter gives an overview of the Ph.D. topic and related research objectives in the state-of-the-art context.

1.1 State-of-the-art context

This PhD thesis tackles atmospheric observation in both over-land and over-sea dimensions from a multi-sensor and multidisciplinary perspective thanks to CommSensLab-UPC's background knowledge acquired in the EU Initial Training for Atmospheric Remote Sensing (ITARS) (over-land) and the EU NEPTUNE (over-sea) European projects. And, more recently, through national project ARS (PGC2018-094132-B-I00) and present project GENESIS (PID2021-126436OB-C21). In addition, the Ph.D aims to contribute to CommSensLab's ongoing collaboration with the Denmark Technical University (DTU) Wind and Energy Systems - Meteorology and Remote Sensing Section, and University of Massachusetts, Microwave Remote Sensing Lab. and Purdue University, Department of Earth, Atmospheric and Planetary Sciences in the US.

The over-land and over-sea dimensions share atmospheric stability as common topic, however, it is tackled with different approaches for each case. In the over-land dimension, atmospheric stability is related to atmospheric boundary layer height assessment, and in the over-sea dimension, it is related to wind profile modelling within the surface boundary layer. Next, Sect. 1.1.1 and Sect. 1.1.2 introduce the over-land and over-sea research fields, respectively.

1.1.1 Over-land dimension

*In the land-atmosphere dimension, the PhD thesis is oriented to the study of the **atmospheric boundary layer (ABL) height (ABLH)** in diurnal conditions.*

The Earth's surface is the bottom boundary of the atmosphere. The portion of the atmosphere most affected by that boundary is called ABL (Wallace & Hobbs, 2006b). Most of the interactions between the Earth's surface and atmosphere, such as, exchange of momentum, heat, humidity, and atmospheric gases, as well as aerosols transportation, occur in the ABL (Stull, 1988; Fisher, 1998; Kotthaus et al., 2022). Accordingly, the ABLH is a matter of interest for many applications with high societal and economic impacts, which include numerical weather prediction, assessment of air quality, aviation, and wind energy (Kotthaus et al., 2022).

Despite its importance, observational knowledge of the ABL is still scarce (Cimini et al., 2020). Historically, since the 1930s, sensing the boundary-layer vertical profiles of pressure, temperature, water vapour and wind, has been mostly achieved by means of radiosonde (RS) (Dirksen et al., 2014; Rocadenbosch et al., 2020). However, although RS launches provide a wealth of information about the atmosphere, their limited temporal resolution is usually insufficient to monitor the whole diurnal evolution of the boundary layer. Since each launch relies on an expensive balloon-borne package of sensors, most of the meteorological stations only perform RS launches twice daily. Furthermore, the launches are impacted by a significant horizontal drift of the balloon during its ascent, therefore, the observations are affected by spatial variations which can lead to challenging data interpretation (Kotthaus et al., 2022).

In contrast, the drawbacks of ABL monitoring through RS can be reduced by increasing the use of existing ground-based remote sensing technologies, such as, e.g., Radio Detection and Ranging (hereafter, radar), Sound Detection and Ranging, (hereafter, sodar), and Light Detection and Ranging (hereafter, lidar) (Cimini et al., 2020; Wagner et al., 2019). Remote-sensing profilers enable monitoring variations in atmospheric conditions that are key to describing the ABL dynamics and structure at a given location, hence providing a better comprehension of the atmospheric exchange processes (Cimini et al., 2020).

During the day, the warm air near the earth's surface produces vertical plumes (thermals) that create convective circulations, producing the so-called mixed layer (ML). Different kinds of ground-based remote-sensing instruments such as lidar,

radar, sodar and microwave radiometer (MWR) are employed to monitor atmospheric parameters, namely, aerosol concentration, temperature, or vertical wind velocity, in which characteristic structures are used as tracers of the ML height (MLH) (Collaud Coen et al., 2014). Such MLH estimates derived from remote-sensing technologies are often validated using MLH estimates from radiosonde (RS) observations, which are usually taken as the standard reference (de Arruda Moreira et al., 2018).

Collaud Coen et al. (2014) and de Arruda Moreira et al. (2018) have shown successful results when comparing MLH estimations from MWR- and RS-retrieved potential-temperature profiles by applying the parcel method (Seibert et al., 2000) over both. However, the MWR is a passive remote sensing instrument whose spatial resolution becomes coarser with height, thus inserting uncertainty to its measurements

In contrast to the MWR, the lidar ceilometer (LC) is able to retrieve aerosol-backscatter profiles with high and constant spatial resolution (15 or 30 m). The MLH retrieval by means of an extended Kalman filter (EKF) applied to aerosol-backscatter profiles from the LC (hereafter, MLH-LC-EKF) has proven to be an extremely reliable method. Lange et al. (2014) showed that, when the BL is convective due to insolation (e.g., in the afternoon), MLH-LC-EKF produced more accurate results than classical MLH retrieval approaches such as the threshold and gradient methods (Seibert et al., 2000). However, outside the convective regime, the MLH-LC-EKF usually tracked the top of the non-convective residual layer (RL).

PhD over-land-dimension focus

Given the importance and complexity of the ML, and the successful results of MLH tracking obtained from MWR and LC observations in previous works, *this PhD aims to study a synergistic method that combines the MLH-MWR and MLH-LC-EKF.* This synergistic method is aimed at combining the best MLH estimates from MWR and LC using a maximum likelihood criterion, in order to provide a more robust MLH estimate at all times of the day. Radiosonde and Doppler wind lidar (DWL)-derived MLH estimates will be used as references.

The over-land dimension of this PhD benefits from measurements that have already been carried out during long-term Intensive Observation Periods (IOP) in the context of European Union (EU)-based measurements campaign. This is contextualised and exploited in Saeed (2016) PhD guided by Prof. Rocadenbosch,

which has served as a first step in the present PhD and given rise to different International peer-review conference papers (Araujo da Silva et al., 2021; Muñoz-Porcar et al., 2021; Araújo da Silva et al., 2022b; Araújo da Silva et al., 2022b). Departing from this background, this PhD specifically focuses on EU campaign HOPE, an acronym for HD(CP)^2 Observational Prototype Experiment (HOPE, Sect. 2.1.4). The HOPE campaign took place at the Jülich Observatory for Cloud Evolution (JOYCE), located in Jülich, Germany, which is a super-site equipped with a unique array of state-of-the-art in situ and remote sensing instruments (Löhnert et al., 2015a).

1.1.2 Over-sea dimension

The sea-atmosphere dimension of the PhD tackles the floating DWL (FDWL) as key technology to the assessment of off-shore wind-energy resource and, specifically, atmospheric stability in the surface layer.

Wind energy is one of the most promising solutions to achieve the worldwide shift from fossil fuel-based to cleaner energy (Msigwa et al., 2022). With 21.1 GW commissioned, 2021 was the best-ever year for the global offshore wind market. The new installations in 2021 led the world's offshore capacity to 57 GW, which represents 7% of global installations. Furthermore, it is expected a worldwide growth of more than 90 GW of offshore capacity from 2022 to 2026 (GWEC, 2022). Europe and Asia have been the regions with the highest investments in off-shore wind energy over the last years (GWEC, 2019, 2022). China, United Kingdom, Denmark, Vietnam, and the Netherlands are the world's top five markets in 2021 for new offshore installations (GWEC, 2022).

However, off-shore wind farms still have higher production costs than onshore ones. Besides, costly meteorological masts (metmasts) installed on the seabed have traditionally been employed for assessing the wind resource in potential wind-farm deployment sites. In contrast with the metmast, the FDWL emerges as a very competitive alternative that offers key benefits to the off-shore wind industry such as lower costs of installation and maintenance, and easier re-deployment (Carbon Trust, 2018). For these reasons, several researchers and scientists around the world have joined efforts to convert the FDWL into the preferred atmospheric sensing tool for wind energy applications. For instance, the International Energy Agency Wind Technology Collaboration Programme (IEA Wind TCP) has launched the

Task 32 and Task 52 Missions in 2012 and 2022, respectively. Those are international research collaboration projects aimed at improving different DWL applications and integrating both industry and academia in search of the most innovative solutions (IEA-Wind, 2023). The Task 52, for example, is divided in four topics:

- Universal inflow characterisation
- Replacing met masts
- Connecting wind lidar
- Accelerating offshore wind deployment

During the last years, the FDWL has primarily been used to measure mean wind speed and direction. However, overall, FDWLs cannot assess atmospheric parameters, such as atmospheric stability, friction velocity and turbulence intensity, with the same accuracy as masts. The study of atmospheric stability has been a subject of interest to the wind energy industry (Holtslag et al., 2014). It can affect different aspects of the wind power generation, e.g., turbine power performance, wind shear, and wakes (Subramanian et al., 2018; Kim et al., 2021). Furthermore, vertical distribution of momentum and hub height wind speed are impacted by atmospheric stability which is usually classified as convective, neutral or stable (Holtslag et al., 2014; Archer et al., 2016). Fatigue loads in wind turbines, induced by turbulence intensity magnitudes variations, are also related to stability regime. According to atmospheric stability type, turbulence and wind speed can greatly vary affecting the turbines performance (Wharton & Lundquist, 2012; Holtslag et al., 2014; Archer et al., 2016).

PhD over-sea-dimension focus

A state-of-the-art report and recommended practices have been developed by the IEA Wind-Task 32 and 52 (Clifton et al., 2018) to mitigate barriers to the adoption of wind lidar for wind-energy purposes. *In the present PhD, this wide area of research is focused on the study of the influence of the atmospheric stability on wind profiles by using over-sea surface-layer observations.*

This topic is according to state-of-the-art research interests at leading Universities in the field such as Denmark Technical University (DTU) in Europe (DTU-Wind, 2023), and Cornell University (Sibley School of Mechanical and Aerospace

Engineering) (Cornel-Engineering, 2023) and UMASS Wind Energy Center (UMass, 2023) in the US.

In 2018 the Carbon Trust published the roadmap for commercial acceptance of lidar technology in the wind industry (Carbon Trust, 2018). Accordingly, it has been shown that the FDWL offers the capability to monitor wind direction and vertical wind profile. However, so far other parameters for turbine siting have not been well explored from FDWL measurements (Peña et al., 2022). The over-sea dimension of this PhD thesis tackles the potential of FDWL as key enabling technology to the assessment of off-shore wind-energy resource with focus on atmospheric-stability estimation. Therefore, corroborating the best competitiveness of the FDWL in relation to the metmast. Towards this end, this thesis investigates methods for estimating surface boundary layer parameters from FDWL-measured wind profile, namely, friction velocity and Obukhov length. The latter is often used to assess atmospheric stability.

1.2 PhD Objectives

The PhD tackles over-land and over-sea atmospheric remote sensing through these objectives:

1.2.1 Objective 1. Intelligent estimation and time tracking of the MLH over the daily cycle

This objective aims to investigate a synergistic method to optimize the retrieval of MLH from individual remote-sensing and in-situ sensors, as well as to intelligently combine the observations from multiple sensors, namely, the MWR and the lidar ceilometer, to improve the overall retrieval. The measurement data used to accomplish this objective is part of the HD(CP)^2 Observational Prototype Experiment (HOPE) campaign carried out at JOYCE (see Sect. 2.1.4). This objective comprise the following tasks:

T1.1. Development of the synergistic MLH-estimation method

- Familiarisation, improvement and development of Matlab routines for MLH estimation using DWL, RS, MWR and lidar-ceilometer HOPE data and the existing background at CommSensLab-UPC (Saeed, 2016).
- Development of the ceilometer-MWR synergistic method.

- Validation of the ceilometer-MWR synergistic method against the RS-reference estimations as well as comparison with other stand-alone methods.

T1.2. Development of statistical tools to assess the performance of the synergistic method.

This objective will be in part carried out in collaboration with Dr. Robin Tanamachi, Department of Earth, Atmospheric, and Planetary Sciences, Purdue University.

1.2.2 Objective 2. Off-shore DWL estimation of atmospheric stability

The final objective of the over-sea dimension is to obtain a consistent algorithm based solely on the observed wind profiles in order to retrieve surface-boundary-layer parameters, namely, the friction velocity, heat flux, and Obukhov length. The latter will be used to assess atmospheric stability. Algorithm performance is studied using data from floating Doppler wind lidar (FDWL) observations close to the reference mast of IJmuiden in the North Sea (see Sect. 2.2.3). This objective is to be achieved in collaboration with DTU Wind and Wind Energy Systems - Meteorology and Remote Sensing Section (see Sect. 1.3). Obj. 2 is divided in three tasks:

T2.1. Numerical estimation of wind profile models in neutral and non-neutral conditions

- Development of a parametric Matlab solver: estimation of model of friction velocity, heat flux and Obukhov's length parameters.
- Numerical estimation of wind profile model.

T2.2. Sensitivity to model parameter errors

- Computation of upper and lower-bound error envelopes in response to model parameters errors.

T2.3. Application to off-shore measurement campaign data

- FDWL data outlier rejection based on the lidar internal parameters such as backscatter coefficient, bearing and spatial variation.

- Reference anemometer data screening in order to avoid metmast shadow effects.
- Computation of 1-h binned histograms of atmospheric stability classes over the whole IJmuiden campaign.
- Validation of model parameters (e.g., roughness length, friction velocity and Obukhov's length) with reference to metmast-derived parameters.

1.2.3 Objective 3. Transversal tools for big-data statistical analysis

Obj. 3 provides the statistical tools in support of Objs.1 and 2 above. Descriptive statistics will be used to type derive Key Performance Indicators and features from the big-data measurement databases available. Besides, descriptive statistics provide simple summaries about the sample and the measures. Together with graphics analysis, they form the basis of virtually every quantitative analysis of data.

T3.1. Selection of key descriptive statistics indicators

- Central tendency and variability indicators for analysing observational campaign data (over-land and over-sea measurement campaigns).
- Development of methods for measurements uncertainty assessment and comparison over large observational periods (e.g., HOPE, Ijmuiden).

T3.2. Database querying tools

- Familiarization with existing Matlab's Structured Query Language (SQL) tools in the research group.
- Development of tools to access large databases ($\sim$ 50 GB).

1.3 PhD mobility context

DTU Wind and Energy Systems is a department recognised worldwide in the field of wind energy because of its extensive integration of research and innovation as well as its embracing of public-private sector consulting. Marcos P. Araújo da Silva was hosted for 99 days at **Denmark Technical University (DTU)** - Wind and Energy Systems through three secondments. During these stays he was under the

supervision of Senior Scientists Profs. Alfredo Peña and Jakob Mann, who hosted him at the Meteorology and Remote Sensing Section. In the following, a summary of each visit is given:

- **From 15 November 2020 to 13 December 2020** an assessment of the sensitivity of surface layer variables to the Monin-Obukhov wind profile model was initiated. Furthermore, the PhD candidate attended the insightful *PhD Summer School: Remote Sensing for Wind Energy.*
- **From 9 January 2022 to 13 March 2022** the topic of friction-velocity and Obukhov-length retrieval was tackled (Araújo da Silva et al., 2022a). In addition, the development of a methodology to retrieve vertical wind speed gradient (or simply wind-shear) and dimensionless wind-shear from solely floating-lidar-measured wind profiles was started.
- **From 19 September 2022 to 27 September 2022** a short-term scientific mission to revisit the limitations of the surface-layer parameter-retrieval methods previously developed as part of the secondments above was done.

1.4 Structure of the PhD thesis

This PhD thesis is structured as follows:

Chapter 1 gives the overall context of this PhD thesis and describes its main objectives for the over-land and over-sea dimensions.

Chapter 2 reviews atmospheric boundary layer concepts and describes the remote sensing instruments employed.

Chapter 3 presents the synergistic MWR-ceilometer algorithm for MLH retrieval and cross-examines it in relation to stand-alone MLH-estimation methods. This chapter is in line with Obj. 1 (Sect. 1.2.1)

Chapter 4 presents the so-called 2D parametric solver algorithm to assess offshore atmospheric stability relying on FDWL-measured wind profiles only. The acronym "2D" stands for two-dimensional retrieval, i.e., simultaneous retrieval of the Obukhov length and friction velocity. This chapter is in line with Objs. 2 and 3 (Sect. 1.2.2).

Chapter 5 revisits the 2D algorithm by comparing it to the well-known Hybrid Wind algorithm in the state of the art (Basu, 2018) across the IJmuiden test site in the North Sea. This chapter is in line with Objs. 2 and 3 (Sect. 1.2.2).

Chapter 6 gives concluding remarks and outlook of work.

Chapter 2

Remote sensing foundations relevant to this PhD thesis

This chapter introduces basic over-land boundary-layer and over-sea surface-layer foundations as well as related remote-sensing instruments and methods relevant to this Ph.D. thesis. A short overview of the key measurement campaigns sustaining this thesis is also presented.

2.1 Over-land atmospheric boundary-layer sensing

2.1.1 Atmospheric boundary-layer review

The thickness of the ABL is quite variable in space and time. Normally, it is 1-to-2 km thick, i.e., occupying the bottom 10 to 20% of the troposphere. It can range from tens of meters to 4 km or more (Wallace & Hobbs, 2006b). The ABL structure depends deeply on the environmental conditions, one example is the big difference between the ABL over the land and over the ocean, or the difference between day and night.

Over land, the ABL has overall a well-defined structure which evolves during the day due to the change in the Earth's surface temperature caused by the absorption of solar radiation. During fair weather days, the ABL behaviour is generally described by a diurnal cycle with three main structural components:

1. The mixing layer (ML), which develops during the daytime as a result of turbulence generated by solar heating of the land surface. Under this condition the atmosphere interacts directly with the Earth's surface through turbulent mixing. Consequently, chemicals are generally well mixed.

2. The residual layer (RL), which forms around half an hour before local sunset as turbulence intensity decays, maintaining residual moisture and heat character of the ML; and

3. The stable boundary layer (SBL), which is formed by the cold air yielded in response to the surface cooling throughout the night progress. The SBL is normally characterized by static stable air that leads to suppress the turbulence (Stull, 1988; Wallace & Hobbs, 2006b).

In Fig. 2.1, a conceptual model of the ABL diurnal cycle representing the structural components mentioned above is depicted. At the top of the ML, the Entrainment Zone (EZ) acts as a buffer between the ML and the Free Troposphere (FT) above.

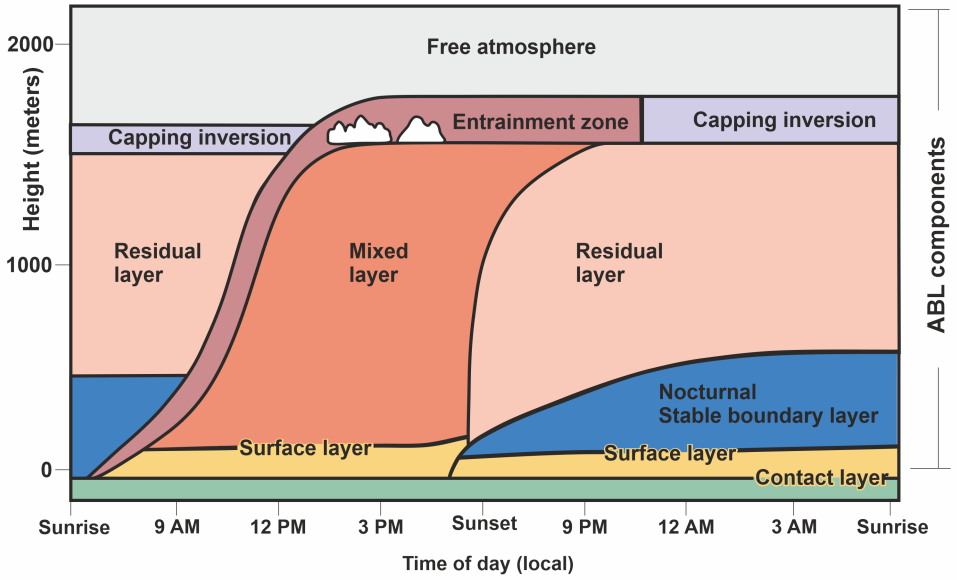

Figure 2.1: Typical diurnal cycle of the ABL over land. Adapted from the daily cycle models presented in Tanamachi et al. (2019) and Stull (1988).

2.1.2 Review of instruments and methods

Due to the ML complexity, there is no remote sensing instrument that can directly derive the MLH. Instead, a proxy or tracer for the top of the ABL must be used. Such proxies include aerosols, temperature or wind profiles as well as energy fluxes (Seibert et al., 2000; Emeis, 2010).

Most of the methods to estimate ABLH are based on proxies for the mixing process, such as temperature, humidity or wind speed. Fig. 2.2 depicts idealized vertical profiles of such kinds of proxies. These parameters are frequently used in radiosonde-based retrievals, which are often considered to be the most reliable as they are based on in situ measured parameters, and are therefore used as reference in several studies (Löhnert & Maier, 2012; Belegante et al., 2014; Schween et al., 2014; de Arruda Moreira et al., 2018).

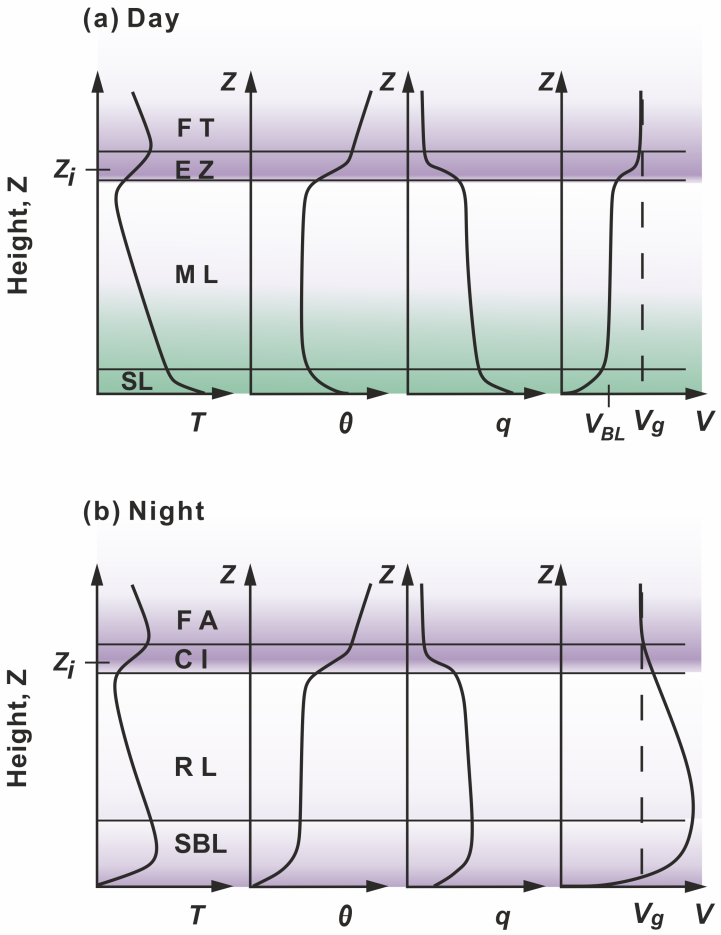

Figure 2.2: Sketch of typical vertical profiles of temperature (T), potential temperature (θ), specific humidity (q), and wind speed (V) in the bottom of the troposphere. FT, free atmosphere; EZ, entrainment zone; ML, mixed layer; SL, surface layer; CI, capping inversion; RL, residual layer; SBL, stable boundary layer; z_i, height of the capping inversion, which equals top of the boundary layer (BL); V_p, geostrophic wind speed. Adapted from Fig. 9.16 in Wallace & Hobbs (2006b).

However, radiosondes measure properties along their flight path and their data

might not be representative for the atmospheric column above the measurement site. Due to the fact that a radiosonde follows the horizontal wind during its ascent, it tends to move into regions with convergence and avoids regions with divergence. As a result radiosonde profiles are biased towards properties of rising plumes in convective situations. In addition, a major shortcoming of radiosondes for MLH estimation is their coarse temporal resolution.

Many of the radiosonde drawbacks can be overcome by continuously operating ground-based remote sensing instruments. Combined atmospheric observations from multiple remote-sensing systems and appropriate data-processing techniques offer insights in to atmospheric phenomena that single instruments cannot (Wulfmeyer et al., 2015).

The following Sects. 2.1.2 - 2.1.2 briefly review the sensors and retrieval methods that will be used in this thesis:

Radiosonde

The **radiosonde (RS)** is a *de facto* standard for reference in the atmospheric sciences (Eresmaa et al., 2006; Münkel et al., 2007; O'Connor et al., 2010). Radiosondes measure *in situ* profiles of the atmospheric thermodynamic state (temperature, pressure, water vapour and wind), and are usually launched attached to a large balloon. A radiosonde can rise up to 40 km in height over the course of several hours, though most water-vapour sensors usually cease to operate properly below the tropopause ($\sim$ 15 km in the mid-latitudes). The main drawbacks of using radiosondes for MLH determinations are the sparse temporal resolution (owing to the expense associated with each launch) and horizontal drift on ascent.

Microwave radiometer

The function of a microwave radiometer (MWR) instrument is to receive the brightness intensity in terms of antenna temperature, transduce it in the receiver as detector voltage and then convert the detector voltage to the source brightness temperature through appropriate calibration. The measured source brightness temperature can then be used to retrieve the atmospheric parameters of interest (Saeed, 2016). Fig. 2.3 shows a schematic layout of the internal structure of a RPG HATPRO MWR. A parabolic scanning antenna collects the incident brightness power from atmosphere which is split by a beam splitter into the two receivers. The two

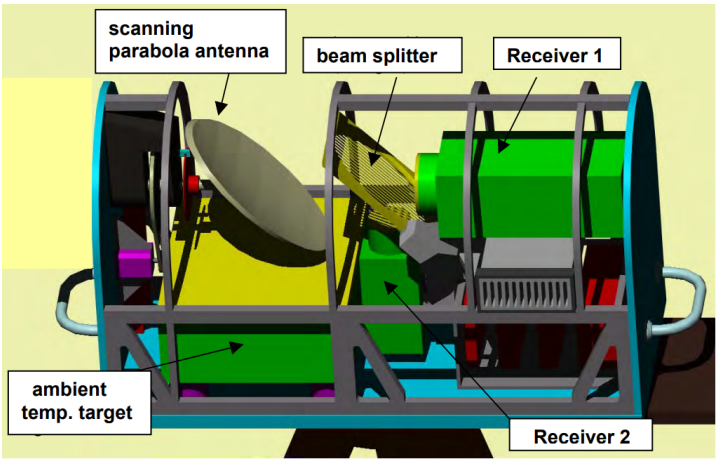

Figure 2.3: Schematic internal structure of RPG HATPRO radiometers. Source: Fig 2.1 in RPG (2023).

receivers correspond to the K (20-30 [GHz]) and V (50-60 [GHz]) bands for temperature and water-vapour retrievals, respectively.

A MWR measures the radiative emission of atmospheric gases. The emissions from molecular oxygen, in particular, are proportional to atmospheric temperature when the water vapor mixing ratio remains constant. Measurements at different frequency bands and elevation angles can be used to derive several physical quantities such as temperature, water vapor, integrated water vapor, and liquid water path.

The MWR-derived temperature profile exhibits a coarse ($\geq$ 50 m) vertical resolution that increases with height (Crewell & Löhnert, 2007; Löhnert & Maier, 2012), and which is specific to the retrieval algorithm and to the number of measurement channels (sounding frequencies) being used. Because the number of independent pieces of information contained in the brightness temperature measurements at different frequencies and scanning angles is limited, the resulting Degree of Freedom (DoF) is low (≈ 4 for temperature boundary-layer profiling) (Löhnert & Maier, 2012). As a result, the vertical resolution of the retrieved quantities substantially decreases (i.e., becomes coarser) with height. As a general rule, the vertical resolution is approximately equal to the height above the surface. For example, the vertical resolution at 1 km AGL is roughly 1 km (i.e., the retrieved temperature at 1 km AGL is valid for the 500 – 1500 m layer).

Lidar ceilometer

A **lidar ceilometer** is a single-wavelength elastic-backscatter lidar characterised by a low energy-aperture product. Ceilometers rely on the principle of lidar technology, essentially measuring the backscattered light by the aerosols, after the emission of a laser pulse (Saeed, 2016). Under moderate-to-clear-air atmospheres (optical thickness, $\tau < 1$) and, particularly, towards the near-infrared, the profile of the attenuated-backscatter coefficient is essentially proportional to the aerosol concentration in the ABL (Lange et al., 2014; Measures, 1992; Schween et al., 2014).

A lidar ceilometer has three main hardware modules, namely, the laser, the telescope, and the detection and processing system as shown in Fig. 2.4. First, short light pulses with lengths of a few to several hundred nanoseconds are generated by the laser and transmitted to the atmosphere. At the detection stage, a telescope collects the photons backscattered from the atmosphere. Then, the collected radiation is directed onto an optical detection hardware, where the received optical signal is converted into an electrical signal. Finally, the received signal is electronically organised by the acquisition hardware and then, it is stored in a computer (Weitkamp, 2006).

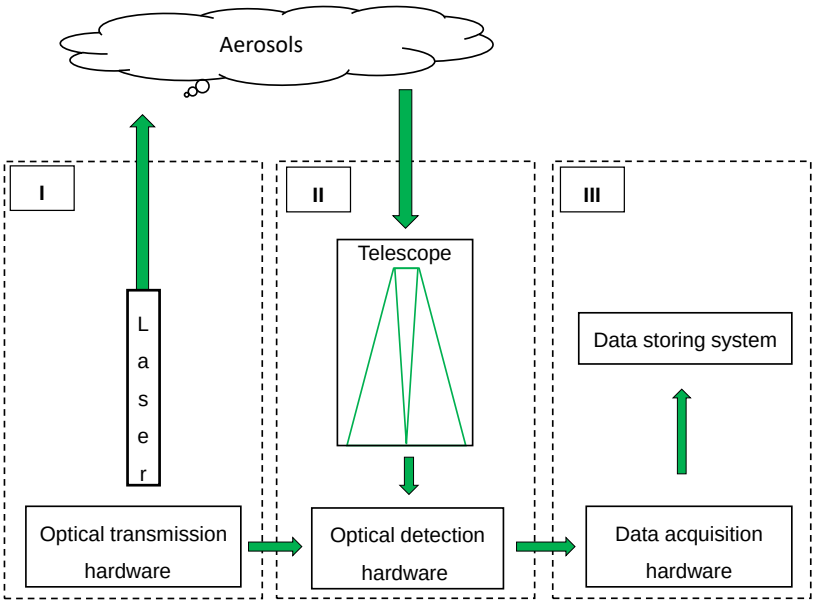

Figure 2.4: Block diagram of a basic lidar setup.

Doppler wind lidar

Driven by the technological progress in the wind energy industry in the last couple of decades, economical and useful **Doppler Wind Lidar (DWL)** systems have been developed (Pearson et al., 2010). DWL provides a wealth of information about the wind flow and also allows measurement in places which are inaccessible for standard in-situ anemometry (Tzadok et al., 2022). The DWL measures the velocity of air particles by knowing the frequency shift between the emitted beam and the received backscattered. This frequency shift is related to particle velocity by the Doppler effect

$$f_d = -\frac{2v_r}{c} f_0, \tag{2.1}$$

where f_d is the Doppler-shift frequency between the received $f_r = f_0 + f_d$, and the emitted frequencies, f_0, v_r is the radial velocity of the target relative to the lidar (positive when the target moves away from the lidar), and c is the speed of light (Villalonga, 2020; Salcedo-Bosch, 2020).

Since DWL provide only the wind component of the radial direction, some data processing based on mathematical manipulations is required to solve the whole wind vector. There are different scanning methods for performing measurements with DWL, such as the velocity azimuth display (VAD), and the Doppler beam swing (DBS). The DBS is based on a vertical measurement followed by tilted beams in two perpendicular directions (Tzadok et al., 2022).

The DWL indirectly measures the ABL mixing process by using vertical wind velocity variance as a tracer of the ML (Schween et al., 2014; Rose et al., 2005). Because the Free Troposphere (FT) is generally not as turbulent as the ML, vertical gradients in the standard deviation of velocity can be used as a tracer of the ML (Cohn & Angevine, 2000; Hogan et al., 2009).

Finally, it is important to clarify that the over-sea dimension of this PhD will benefit from the ZephIR™ 300 DWL performing the VAD scan, which is further discussed in Sect. 2.2.2, whereas the over-land dimension here will use a Halo StreamLine-XR DWL which can perform three types of scan: VAD, DBS and "stare" scan in the vertical direction.

2.1.3 MLH estimation from sensors in isolation

Estimation from RS and MWR data

The **parcel method** is commonly used for MLH estimation using potential temperature data (Holzworth, 1964; Seibert et al., 2000). For a given profile of physical temperature, $T(z)$, which can be retrieved from both MWR or RS measurements, the first step is to convert it to potential temperature profile, $\theta(z)$. The MLH is defined as the lowest point in a given potential temperature profile for which, $\theta(z) > \theta(0)$, where $\theta(0)$ is the surface value of the potential temperature. The gradient of potential temperature profile with respect to height, $\frac{d\theta}{dz}$, is indicative of the stability of the atmosphere as follows:

- The atmosphere is stable when $\frac{d\theta}{dz} > 0$;
- Neutral when $\frac{d\theta}{dz} = 0$;
- Unstable when $\frac{d\theta}{dz} < 0$.

Because the parcel method is very sensitive to the surface temperature, we used temperature observations from the JOYCE tower at 2 m as reference. The MLH estimation uncertainty was estimated by perturbing the surface temperature by ± 0.5 K (Collaud Coen et al., 2014). Next, Fig. 2.5 shows a case example of potential temperature profiles and MLH estimates obtained from RS.

Estimation from ceilometer data

The **Extended Kalman filter (EKF)** estimation method (Rocadenbosch et al., 1999; Lange et al., 2015, 2014) was applied over measurements obtained by the Jenoptik CHM-15k ceilometer (see Table 3.2). The EKF is a time-adaptive method based on Kalman filtering that uses time-successive LC attenuated-backscatter profiles to track the sharp aerosol gradient occurring in the ML-to-free troposphere (FT) transition. As a result, the EKF provided an MLH estimate with the same time resolution as the LC data (15 s) (Araújo da Silva et al., 2022b). Fig. 2.6 depicts a colour-plot case example of attenuated backscattering measured by a ceilometer along with MLH estimates obtained through EKF.

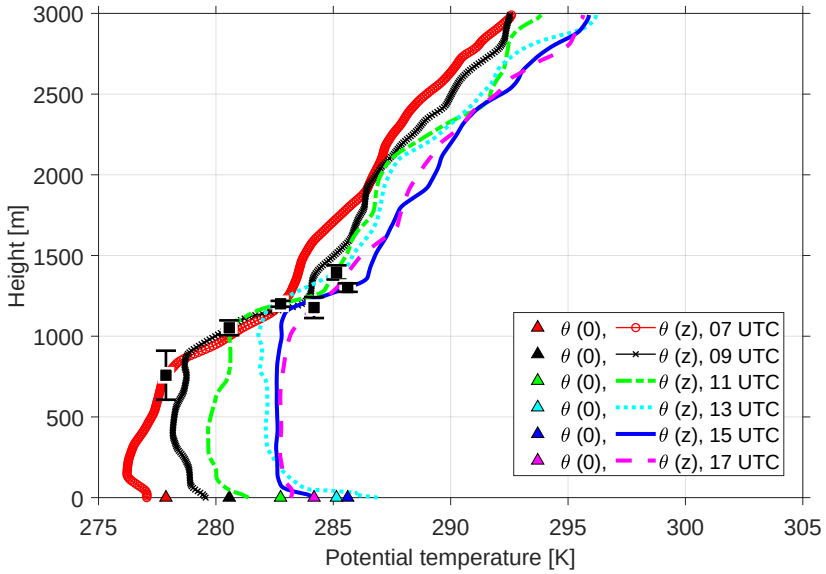

Figure 2.5: Profiles of the potential temperature along with MLH estimates (black squares) retrieved via parcel method in response to radio-soundings at 07:00, 09:00, 11:00, 13:00, 15:00, and 17:00 UTC, on 20 April 2013, JOYCE, Germany. The coloured triangles stand for surface potential temperature measurements.

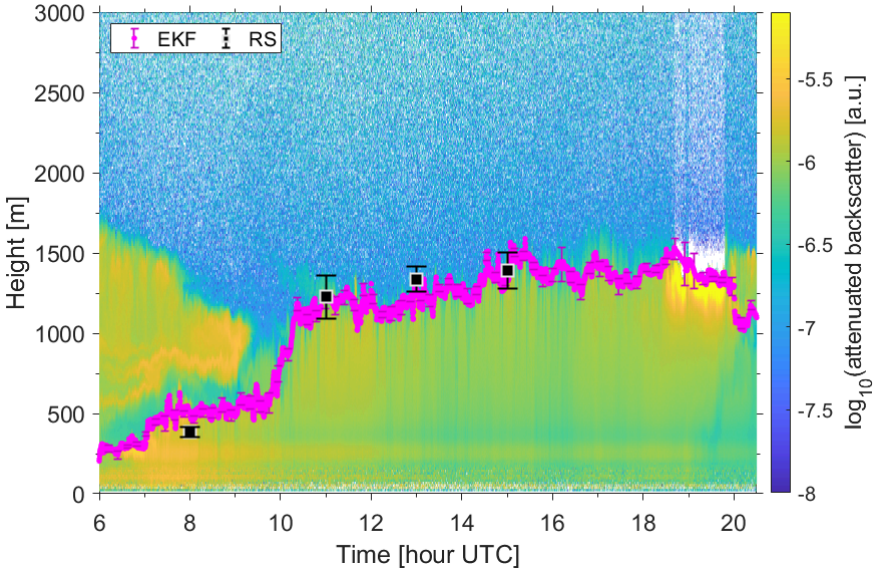

Figure 2.6: Colour-plot of the attenuated backscatter measured by a Jenoptik CHM-15 ceilometer on 04 May 2013, JOYCE. Magenta dots (along with noise-related error bars) represent MLH estimates retrieved through EKF. Black squares are MLH-RS.

Estimation from DWL data

In order to retrieve the MLH from DWL measurements, the standard deviation of time-height profiles of vertical velocity are calculated every 5 min by using a ± 15

min window. Second, the standard deviation is corrected for instrumental noise as described in (Lenschow et al., 1980). Finally, the MLH is calculated as the first height at which the standard deviation of the vertical velocity falls below a predetermined threshold (Tucker et al., 2009). We follow (Schween et al., 2014), who studied the sensitivity of the mixing layer height derived from different thresholds, and we use a 0.4 m/s threshold. Fig. 2.7 depicts a colour-plot case example of vertical-wind-velocity standard deviation measured by the Doppler lidar along with MLH estimates.

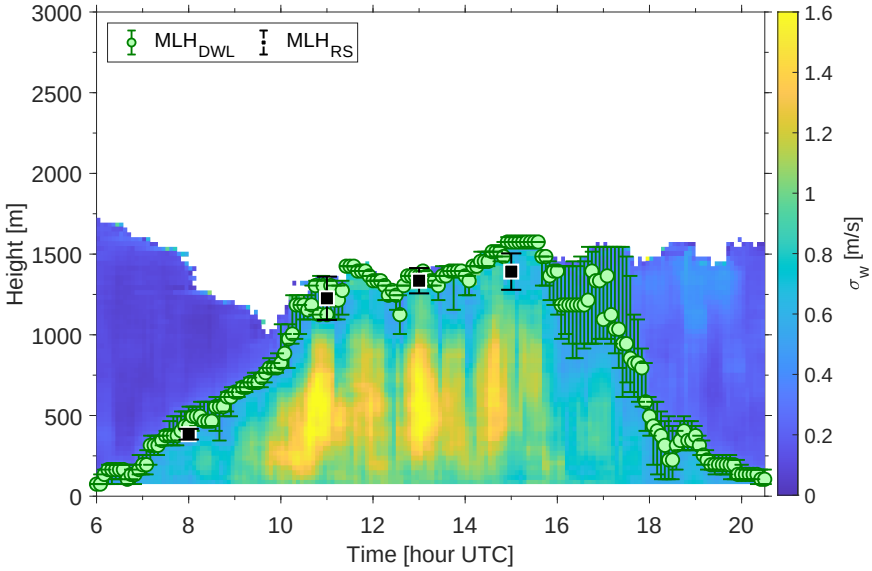

Figure 2.7: Colour-plot of the standard deviation of the vertical wind velocity, σ_w, measured by the Doppler lidar on 04 May 2013 at JOYCE. Green circles on are MLH-DWL, and black squares are MLH-RS.

2.1.4 HOPE measurement campaign

Data used in the over-land dimension of this PhD was collected at the Jülich ObservatorY for Cloud Evolution (JOYCE), which is located in Forschungszentrum, Jülich, Germany (50°54′31″ N, 6°24′49″ E, 111 m MSL). The topography in the area of JOYCE is generally flat apart from large lignite open pit mines. Farming, opencast coal mining areas with major power plants and patchy settlements characterised the 50-km periphery. The climate is characterised by a temperate, humid climate with warm summers (Löhnert et al., 2015b). JOYCE contains a number of active and passive permanently installed remote sensing, and in-situ instruments aimed to the study of clouds and atmosphere. The HOPE campaign (Macke et al.,

2017) was conducted at JOYCE from April 2013 to May 2013. One of the principal aims of HOPE was to characterize the evolution of the ABL over JOYCE for forecasting applications. We chose to examine the data from this campaign because they contain long-duration, simultaneous observation of MLH tracers by multiple independent instruments, a situation ideal for validation. For brevity, only those JOYCE instruments used in HOPE are described below. The reader is referred to (Löhnert et al., 2015b; CPEX-LAB, 2023) for a complete listing.

Ceilometers

Two LCs are used in this work. The first is a Jenoptik CHM-15k Nimbus (Fig. 2.8b), an $8-\mu$J, 1064-nm wavelength, 5-ns-pulse duration, 5-to-7-kHz repetition-rate ceilometer. Under clear-sky conditions, the maximum sounding range is about 15 km with a range resolution of 15 m. The temporal resolution of the instrument is 15 s. The Jenoptik ceilometer is a bi-axial system with separate optics for the transmitter and receiver so that the optical overlap is reached at about 350 m. The instrument provides range- and overlap-corrected profiles of the normalized backscattered power (i.e., the attenuated backscatter-coefficient profile).

The second LC used in the HOPE campaign was a Vaisala CT25K (Fig. 2.8a), used to monitor cloud-base height (CBH) and precipitation, and to complement Jenoptik's observations below 350 m (night-time and morning/afternoon transition periods). The Vaisala CT25K is a $1.6-\mu$J, 905-nm wavelength, 100-ns pulse duration, 5.6-kHz repetition-rate LC designed to retrieve profiles of the attenuated-backscatter coefficient in the sounding range from 60 m to 7 km, with a range resolution of approximately 30 m. The temporal resolution of the instrument is 15 s (including 3.3 s for processing and data transmission). Because of the lower pulse energy of the Vaisala LC as compared to the Jenoptik (and because both systems operate in similar, near-infrared wavelengths), Jenoptik's vertical profiles of the attenuated backscatter coefficient exhibit a comparatively high SNR.

HATPRO MWR

The Humidity And Temperature PROfiler (HATPRO) MWR (Fig. 2.8c) manufactured by Radiometer Physics GmbH (RPG) (Löhnert et al., 2015b; Rose et al., 2005) measures the atmospheric brightness temperature at 14 frequencies in two bands and at six angles (depending on user's settings). Measurements in the K-band (7 channels), $22-31$ GHz, are used for water vapor and liquid water retrieval, and in

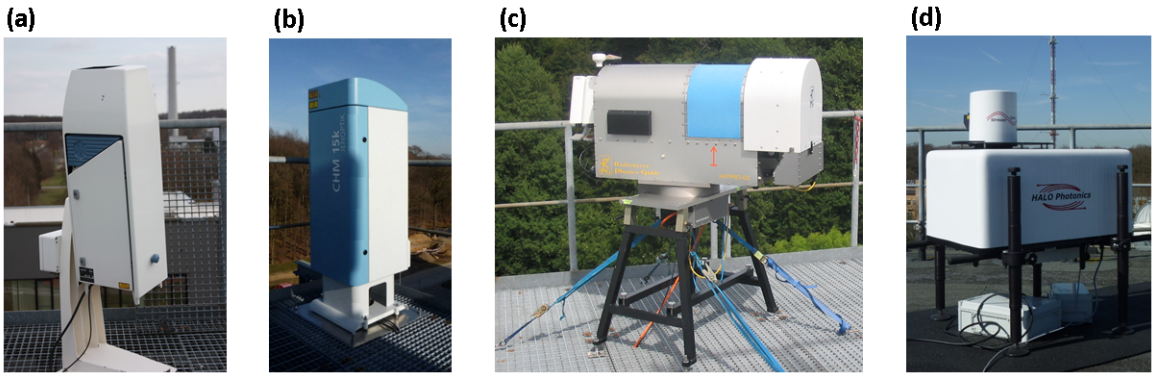

Figure 2.8: Instruments of JOYCE site used in this PhD thesis. (a) Vaisala CT25k ceilometer. (b) Jenoptik CHM15k Nimbus ceilometer. (c) HATPRO MWR. (d) Halo StreamLine XR DWL.

the V-band, $51 - 58$ GHz, for temperature retrieval. The MWR instrument exhibits good temporal resolution (about 2.7 minutes). In principle, MWR can operate in all conditions except for rain, when the radiation measured is dominated by the emission and scattering from raindrops.

Brightness-temperature measurements are converted into a temperature profile by means of a statistical retrieval algorithm (Güldner & Spänkuch, 2001; Cimini et al., 2006; Crewell & Löhnert, 2007; Löhnert et al., 2004) together with auxiliary atmospheric temperature and pressure data. The latter are measured separately by surface-based *in situ* sensors. Ultimately, the retrieved potential temperature profile is used to estimate the MLH. In this formulation, two main error sources are delineated: (i) MLH estimation errors, Δz_T, originating as a total uncertainty in the retrieved temperature profile ($\Delta T(z)$) and (ii) MLH errors due to uncertainties in the auxiliary measurement of surface temperature, Δz_{T_0}. MLH estimates and related errors are computed according to the different spatial resolutions of each instrument.

HALO Photonics Streamline DWL

The DWL used in the HOPE campaign is the HALO Photonics Streamline Wind Lidar (Fig. 2.8d) (Schween et al., 2014; Pearson et al., 2010; Pearson & Collier, 1999), a coherent system with an average pulse energy of 100 μJ and a frequency of 15 kHz. The vertical resolution of this system is 30 m, and the maximum range is about 8 km. However, in practice, its effective maximum range becomes limited by the reduced aerosol content above the ABL.

Radiosonde

The radiosonde used in this work is the Graw DFM-09 manufactured by Graw GmbH, which includes temperature, pressure, humidity and GPS sensors (20 channels). Wind speed and direction are determined from the changes in the GPS position and GPS velocity vector. The transmission rate is one full set of observations per second. During HOPE campaign, 226 soundings were launched up to a maximum of six per day (07:00, 09:00, 11:00, 13:00, 15:00, and 17:00 UTC; local time, LT=UTC+1h) from a site located 3.8 km southeast of JOYCE.

2.2 Over-sea surface-layer sensing

2.2.1 Surface boundary-layer review

The **surface layer** is the region at the bottom of the atmospheric boundary layer where turbulent fluxes and stress vary by less than 10% of their magnitude. Regardless of whether it is part of a mixed layer or stable boundary layer, the bottom 10% of the boundary layer is called the surface layer (Stull, 1988). Drag at the ground always causes the wind speed to be reduced, while aloft the winds are stronger (Wallace & Hobbs, 2006b). Hence, in general, the wind speed profile within the surface layer is nearly logarithmic with height and can be modelled through three surface layer parameters, namely, **aerodynamic roughness**, **friction velocity**, and **Obukhov length** (Stull, 1988; Wallace & Hobbs, 2006b) (see Chapter 4 for detailed formulation). These parameters are introduced next:

- The **aerodynamic roughness length** is defined as the height of zero wind speed as extrapolated down logarithmically from the stronger winds (Wallace & Hobbs, 2006b). The drag laws over the sea are easier to parameterize than over the land, because the roughness length associated with ocean wave height is a known function of surface stress or wind speed, which is called Charnock's relationship.

- The frictional force between the air and the ground is called drag. The **friction velocity** is a measure of the drag force per unit surface area of the ground (Stull, 2017). Accordingly, the friction velocity is a velocity scale that represents the surface stress. Furthermore, it is most applicable to statically neutral conditions within the surface layer, where the turbulence is mostly mechanically generated (Wallace & Hobbs, 2006b; Stull, 2017).

- Besides the friction velocity and roughness length, there is an additional length scale that is crucial to describe the wind profile under statically non-neutral conditions in the surface layer, which is the well-known **Obukhov length**. The Obukhov length can be physically understood as the height above the surface at which buoyant factors first dominate over mechanical (shear) production of turbulence (Stull, 1988).

2.2.2 Review of instruments and methods

Offshore atmospheric stability assessment

There are different techniques to study atmospheric stability such as the vertical profiles of potential temperature, the Obukhov length, turbulence intensity (TI), and wind-shear exponent (Wharton & Lundquist, 2012). Among them, Obukhov length, L, is widely used because it relates both temperature and wind parameters. The stability classification based on L can be, for instance, as described in Table 2.1. Other classification ranges are further discussed in Chapter 4.

Table 2.1: Stability classes based on the Obukhov length, L (Araújo da Silva et al., 2022a).

Atmospheric Stability	Obukhov length range (m)
Stable	$10 < L < 500$
Neutral	$\|L\| > 500$
Unstable	$-500 < L < -50$

Recently, the companion paper by Araújo da Silva et al. (2022a) has introduced a 2D parametric algorithm along with data screening criteria as a method to assess the atmospheric stability from solely FDWL-measured wind profiles. Differently from Beljaars et al. (1989), the 2D algorithm retrieves the stability without using temperature observations. Moreover, it can be extended to an unlimited number of measurement heights, which is complementary to Basu (2018). The 2D algorithm estimates Obukhov length and friction velocity by minimising the norm of residuals between the MOST wind-profile vector and the observed wind-profile vector via a constrained least-squares optimisation. The 2D method is discussed in detail in Chapters 4 and 5.

Continuous-wave Doppler wind lidar

The over-sea dimension of this PhD relies on the **continuous-wave DWL** technology. In continuous-wave lidar systems, light is continuously emitted and focused around a specific height or volume (Gutiérrez-Antuñano, 2019). Thus, a single lidar Line-of-Sight (LoS) measurement can only measure the radial component of the target velocity along the lidar pointing direction. Thereby, in order to retrieve the three components of the wind vector, $\vec{U} = [u, v, w]$, the continuous-wave DWL takes multiple LoS measurements following a conically-shaped scan. For instance, the ZephIR ™ 300 DWL model performs 50 LoS measurements per 1-s long scan.

The redundancy of the number of measured LoSs permits the use of the velocity-azimuth-display (VAD) algorithm. Fig. 2.9 depicts a geometrical representation of the VAD scanning. According to Fujii & Fukuchi (2005); Gutiérrez-Antuñano (2019) and Salcedo-Bosch (2020), the VAD algorithm can be explained as follows:

Each LoS measurement of the radial velocity, v_r, can be expressed as the dot product between the lidar pointing direction unitary vector $\hat{r}$ and the wind vector $\vec{U} = [u, v, w]$:

$$v_r(\phi(t)) = \hat{r}(t) \cdot \vec{U} = v_h \, sin(\theta_0) \, cos\left[\phi(t) - \phi_0\right] + w \, cos(\theta_0), \tag{2.2}$$

where θ_0 is the lidar 30 deg aperture angle from zenith, v_h is the horizontal wind speed (HWS), $\phi(t)$ is the azimuth angle as a function of time, and ϕ_0 is the azimuth angle of the wind vector. The three components of the wind vector can be obtained from Eq. 2.2 as

$$u = A \, cos(\phi_0) \, csc(\theta_0), \tag{2.3}$$

$$v = A \, sin(\phi_0) \, csc(\theta_0), \tag{2.4}$$

$$w = A_{OS} \, sec(\theta_0), \tag{2.5}$$

where $v_h = \sqrt{u^2 + v^2}$, $A = v_h \, sin(\theta_0)$, and $A_{OS} = w \, cos(\theta_0)$. Therefore, by knowing A, A_{OS} and ϕ_0, the wind vector can be retrieved.

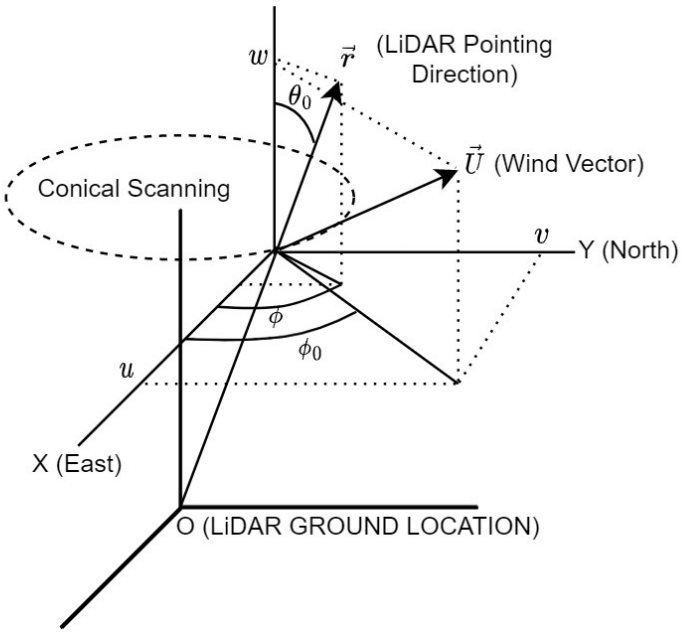

Figure 2.9: Geometrical scheme of the coherent lidar VAD scanning. Adapted from Rocadenbosch (2003).

Finally, the parameters A, A_{OS}, and ϕ_0 are retrieved via a least-squares algorithm that fits the model function (Eq. 2.2) to the LoS ($v_r^{meas.}$), thereby

$$[A, A_{OS}, \phi_0] = \underset{A, A_{OS}, \phi_0}{\operatorname{argmax}} ||v_r(\phi(t)) - v_r^{meas.}(\phi(t))||^2. \tag{2.6}$$

2.2.3 The IJmuiden measurement campaign

The IJmuiden observational campaign was carried during 82 days, from April to June 2015 aimed at validating EOLOS^{TM} FDWL against the metmast reference (Araújo da Silva et al., 2022a). Fig. 2.10 shows the IJmuiden's mast and FDWL geographical positions in the North Sea. Fig. 2.11 shows the instrumental set-up of the campaign, depicting the instruments location and measurement heights. The FDWL was collocated 200 m far from the metmast.

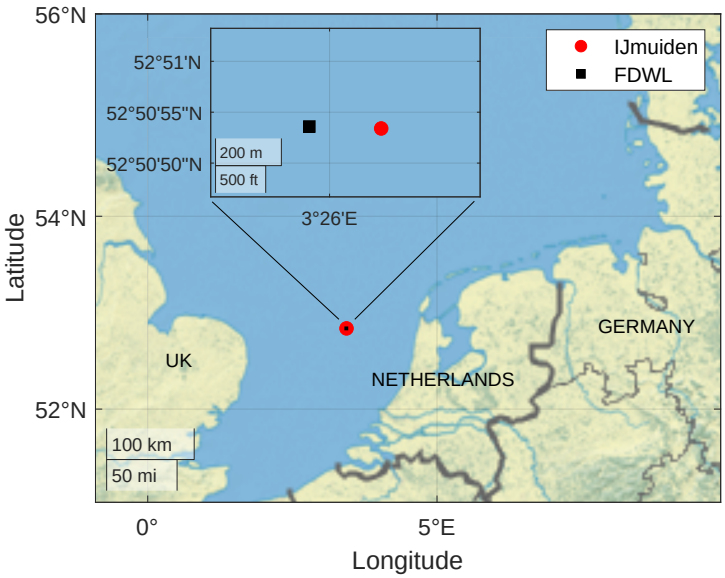

Figure 2.10: Map showing the location of the IJmuiden mast in the North sea. The zoom plot in the upper part of the map shows the FDWL location.

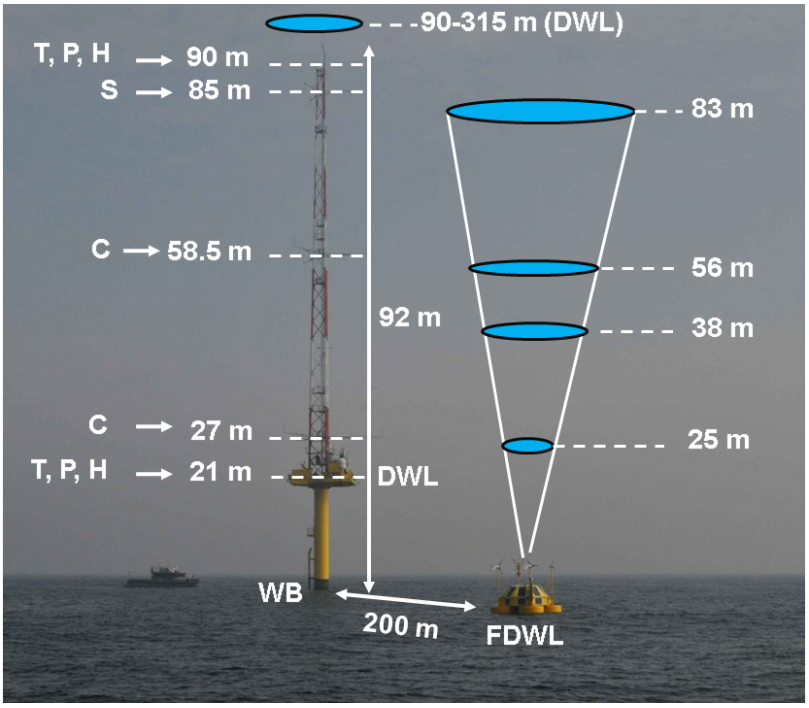

Figure 2.11: Instrument set-up at the IJmuiden test site. The FDWL is in the foreground and the metmast is in the background. Labels: S, Metek^{TM} sonic anemometer; C, Thies^{TM} cup anemometer; DWL, fixed-to-mast DWL; T, temperature sensor; P, pressure sensor; H, humidity sensor; WB, TRIAXYS^{TM} wave buoy.

The IJmuiden metmast was installed 85 km far from the coast of The Netherlands, where the water depth is about 28 meters. Its top was 92 m above the Lowest Astronomical Tide (LAT), and its structure consisted of three booms pointing 46.5°, 166.5°, and 286.5°, clockwise from cardinal north. Hereafter, all height values will be assumed as height above LAT. Three Thies^{TM} First Class Advanced cup anemometers were installed at 27 and 58.5 m in height (one on each boom), as well as three Metek^{TM} USA-1 sonic anemometers at 85 m. Wind direction observations were recorded at 26.2, 57.7 and 87 m by Thies^{TM} First Class windvanes (one on each boom). HWS and wind direction at ten different measurement heights (from 90 to 315 m) were measured by a ZephIR^{TM}300 DWL installed on a platform at 20.88 m in height (hereafter called the mast-DWL). This lidar measured 50 LoSs at equally spaced azimuth angles (7.2° azimuth step between LoSs) at a sampling rate of 50 Hz along a conical scan with elevation of 30° (Salcedo-Bosch et al., 2021c; Werkhoven & Verhoef, 2012). Two Vaisala^{TM} HMP155D were installed at 21 and 90 m, which provided temperature and humidity observations every 0.25 s. Air pressure measurements were recorded at 21 and 90 m by two Vaisala^{TM} PTB210

every 0.25 s as well. A TRIAXYS™ wave-and-current buoy located near the met-mast provided measurements of average wave height, wave period, current direction, and water temperature. The wave-buoy-derived observations were stored as hourly averaged measurements.

Relevant instruments of the IJmuiden's mast used in the over-sea dimension are listed in Table 2.2. The EOLOS™, ZephIR™300 and TRIAXYS™ are described with more details next.

Table 2.2: Main specifications of the instruments from the IJmuiden test site. Detailed information about the sensors arrangement and specification can be found in (Werkhoven & Verhoef, 2012).

Sensor	**Parameter**	**Unit**	**Sampling Rate**	**Height** [(1)]	**Orientation**
3 × Metek USA-1 Sonic Anemometer	Wind speed	m/s	4 Hz	85 m	46.5°, 166.5° and 286.5°
6 × Thies First Class Advanced Anemometer	Wind Speed	m/s	4 Hz	27 and 58.5 m	
9 × First Class Wind Vane	Wind Direction	deg	4 Hz	26.2, 57.7 and 87 m	
2 × Vaisala PTB210	Air pressure	hPa	4 Hz	21 and 90 m	N (21 m) and N-E (90 m)
2 × Vaisala HMP155D	Air temperature	°C	4 Hz	21 and 90 m	N (21 m) and N-W (90 m)
	Relative humidity	%	4Hz		
TRYAXIS wave buoy	Water temperature	°C	60 min	sea level	
2 × ZephIR 300 (mast-DWL and FDWL)	Wind speed	m/s	1 Hz[(2)]	90-315 m, every 25 m (mast-DWL)	S-W
				25, 38, 56 and 83 m (FDWL)	200-m from the mast

[1] Notes: [(1)] Measurement heights above the LAT. [(2)] Averaging rate of the conical scanning performed at each height. (N, N-E, N-W and S-W) stand for North, North-East, North-West, and South-West, respectively.

EOLOS Floating Lidar System

The EOLOS^{TM} Floating Lidar System is prepared for higher endurance during longer measurement campaigns and harsher conditions. In addition, it is designed to host a ZephIR^{TM} 300 lidar. It had 3.77 m width, weighed 3 tons, and had a similar modular four-floater structure design as shown in Fig. 2.12 (Gutiérrez-Antuñano, 2019; Salcedo-Bosch, 2020). The EOLOS^{TM} system hosted three wind generators and multiple solar panels generating a maximum of 2200 W to ensure energy autonomy for long measurement periods. Furthermore, the cover of the buoy cover was constructed with aluminum-reinforced fiberglass to safeguard the internal electronic hardware (Salcedo-Bosch, 2020). The system accounted with data acquisition and communication systems able to store and send the measurements from its different sensors (Gutiérrez-Antuñano, 2019). The data could be acquired through Iridium satellite and through WiFi communications in a 100-m range. In the EOLOS^{TM} system design, the lidar was integrated in the buoy structure without a cardanic frame, being the whole structure a rigid body. Therefore, a single 3DM-GX2-45 IMU was needed to track the buoy's motion (Gutiérrez-Antuñano, 2019).

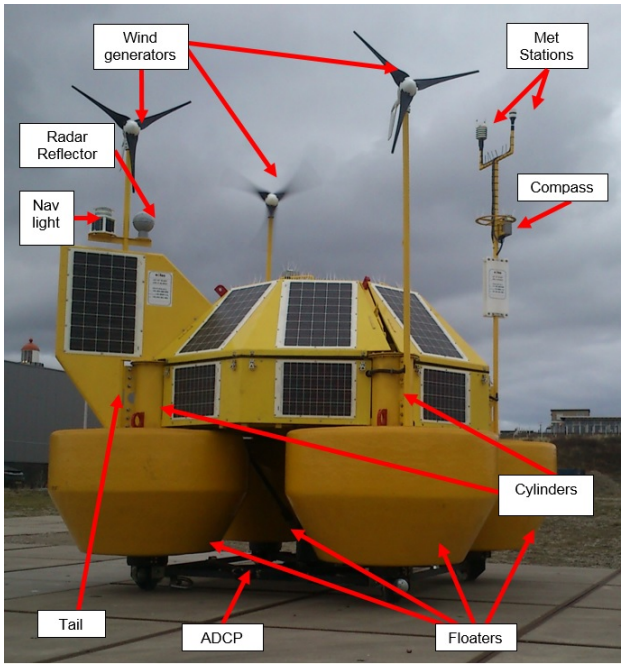

Figure 2.12: The EOLOS lidar buoy. Source: Fig 5.2 in Gutiérrez-Antuñano (2019).

ZephIR 300 DWL

The ZephIR^{TM} 300 is a continuous-wave focused Doppler lidar manufactured by ZX Lidars Ltd. (previously called ZephIR), United Kingdom, which was designed to be also operated at offshore environment (Salcedo-Bosch, 2020; ZX-Lidars, 2023). This lidar system can sense the wind speed and direction at user-defined heights between 10 m to 200 m. Furthermore, it uses the VAD algorithm to retrieve the wind vector by measuring 50 LoS at equally spaced azimuth angles (7.2deg azimuth step between LoSs) along a conical scan of 30-deg aperture width from zenith (ZX-Lidars, 2023). Fig. 2.13 shows a ZephIR^{TM} 300 model and its location at the IJmuiden metmast. Table 2.3 lists its data products during the campaign.

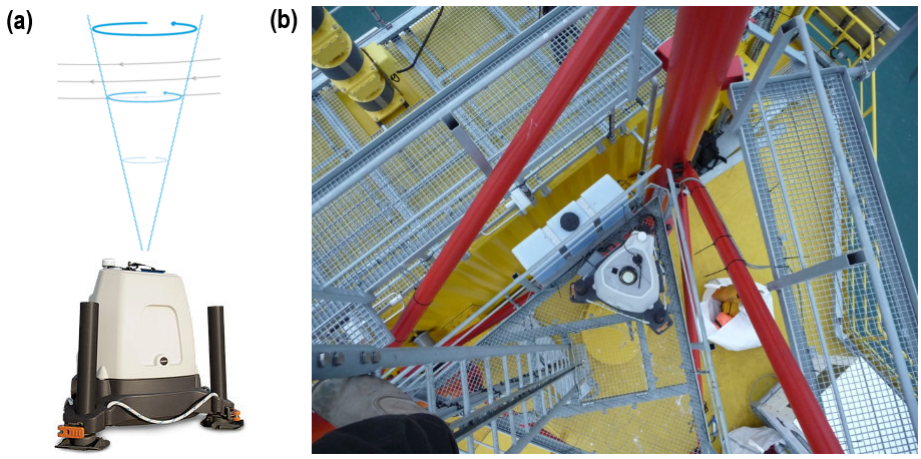

Figure 2.13: (a) ZephIR^{TM} 300 DWL system. (b) Top view of DWL lidar at the IJmuiden metmast. Source: Fig 4.3 and 4.4 in Werkhoven & Verhoef (2012).

Variable	Sampling rate	Height [m]	Units
Measuring points			-
Missed points			-
Packets in fit			-
Wind direction			deg
HWS average	1Hz	90 to 315	m/s
VWS average			m/s
Spatial variation			-
Backscatter			-
Horizontal confidence			-

Table 2.3: Products summary of the ZephIR^{TM} 300 installed at the IJmuiden metmast (Werkhoven & Verhoef, 2012). Vertical wind speed (VWS).

TRIAXYS Wave Buoy

The TRIAXYS™ Wave & Current Buoy is a 1-metre buoy system that measures directional waves and currents at a sampling period of 60 min (Fig. 2.14) (TRIAXYS, 2018). The buoy hosts 3 accelerometers, 3 gyroscopes, and a compass in order to measure the most relevant directional and nondirectional wave parameters. Its products include water temperature, wave height, wave period and mean direction (TRIAXYS, 2018). Table 2.4 summarises the wave buoy data products.

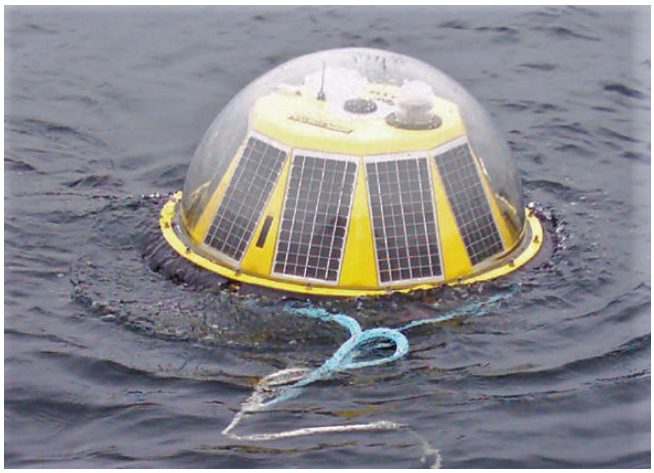

Figure 2.14: TRIAXYS™ wave & current buoy. Source: Fig 4.6 in Werkhoven & Verhoef (2012).

Variable	Sampling rate	Height [m]	Units
Latitude			deg
Longitude			deg
Water depth		sea level	m/s
Water temperature	60 min		deg C
Speed of sound			m/s
Velocity		1 to $-50^{(1)}$	m/s
Direction			deg

Table 2.4: Products summary of the TRIAXYS™ buoy (Werkhoven & Verhoef, 2012). (1) 50 levels of depth.

Chapter 3

Motivating a synergistic mixing-layer height retrieval method using lidar and microwave-radiometer observations

This Chapter introduces the synergistic Mixing-Layer-Height (MLH) retrieval approach that combines both ceilometer and MWR estimates in order to optimize the benefits of both. MLH retrieval methods using backscattered lidar signals from a ceilometer and temperature profiles from a Microwave Radiometer (MWR) are compared in terms of their complementary capabilities and associated uncertainties. The Extended Kalman Filter (EKF) is used for MLH retrieval from backscattered lidar signals and the parcel method is used for MLH retrieval from MWR-derived potential-temperature profiles.

3.1 Introduction

Accurate monitoring of the atmospheric boundary layer (ABL) is a subject of wide interest. The ABL, by definition is directly affected by interactions with the surface of the Earth on a time scale of an hour or less (Stull, 1988), and it is also the layer of the atmosphere within which humans live. The mixed layer height (MLH) is a parameter of interest for many applications, including weather forecasting, air quality and chemical dispersion models, and aviation. In fair weather conditions,

the interior of the ABL is well-mixed by convective turbulence (hence the term "mixed layer", or ML), and exhibits near-constant potential temperature (θ) and water vapor mixing ratio (r) throughout most of its depth. However, no remote or *in situ* instrument exists that can directly measure MLH. Instead, a proxy or tracer for the top of the ML must be used. Such tracers include gradients of aerosols, temperature, wind characteristics, or energy fluxes (Emeis, 2010; Seibert et al., 2000). Ground-based remote-sensing instruments that can detect these tracers include lidar, radar, and sodar, which are active, and microwave radiometer (MWR), which is passive.

Because of the varying properties of these MLH tracers and estimation methods, their accuracy varies widely. Different studies have proven the reliability of MWR retrievals by comparison with radiosoundings. Radiosondes, usually comprising an expendable, balloon-borne package of sensors, are a recognized reference instrument for boundary layer monitoring. Xu et al. (2015) compared MWR-derived temperature profiles averaged over a 30-min (full-span) window centered around the radiosonde profiles. Analysing 403 (760) radiosonde launches from clear-sky (cloudy) days, they obtained correlation coefficients ≥ 0.85 up to ~ 7 km AGL. Good agreement between MWR- and radiosonde-derived temperatures is also described by Löhnert & Maier (2012), who reported differences lower than 0.5 K between the profiles up to 4 km AGL. In relation to MLH assessment, Collaud Coen et al. (2014) applied the parcel method (Holzworth, 1964) to MWR- and radiosonde-retrieved θ profiles, obtaining median bias of -25.5 m and coefficient of determination $\rho^2 = 0.75$ ($\rho = 0.87$) over 100 samples. In a related study, de Arruda Moreira et al. (2018) found excellent agreement during convective conditions, with a root mean square error (RMSE) $= 190$ m and $\rho = 0.96$.

The MWR has higher temporal resolution (e.g., a few minutes) than the radiosonde, whose operational frequency may be as low as two launches per day. However, its vertical resolution decreases with height, hence increasing uncertainty in retrieved quantities. In contrast, the lidar is an active remote sensing instrument designed to measure vertical profiles of aerosol backscattering with high spatiotemporal resolution. Aerosol concentrations are usually relatively high and constant throughout the ML and much lower aloft, thereby enabling lidar-based MLH estimation. In a fair-weather convective boundary layer (CBL), MLH-lidar and MLH-MWR tend to converge. Belegante et al. (2014) compared MLH estimates retrieved from elastic-lidar range-corrected-signal (RCS) profiles averaged over 30-min intervals with those from MWR-derived virtual potential tem-

perature, finding high correlation ($\rho \approx 0.98$) in CBL conditions. However, during evening transition times (ETT; i.e., at and after sunset, when thermally-driven turbulent mixing ceases), MLH-MWR is more accurate than MLH-lidar, which generally tended to track the RL (i.e., a remnant layer left over from earlier turbulent mixing) height (Belegante et al., 2014). Cimini et al. (2013), using training data from multi-frequency, multi-angle MWR and lidar observations, designed a multivariate linear regression method to assess the mixing-layer height (MLH) directly from MWR brightness-temperature observations instead of retrieved profiles.

Lange et al. (2014) (CommSensLab-UPC) estimated MLH by applying an extended Kalman filter (EKF) (Kalman, 1960) to backscattered lidar returns (hereafter, MLH-LC-EKF). They showed that, for a CBL with moderate-to-low signal-to-noise ratio (SNR > 5), MLH-LC-EKF was more accurate than classical approaches such as the threshold (Melfi et al., 1985), gradient (Endlich et al., 1967), logarithmic gradient (Senff et al., 1996), inflection point (Menut et al., 1999), and variance methods (Hooper & Eloranta, 1986). Additionally, Banks et al. (2015) showed the MLH-LC-EKF reliability against radiosonde-derived Bulk Richardson Number profiles and against Weather Research and Forecasting (WRF) model predictions for clear-air and pre- convective storm cases. Based upon these works, de Arruda Moreira et al. (2018) found correlated results among MLH estimates in the CBL derived from LC-EKF, MWR and Doppler Wind Lidar (DWL) combinations. The EKF has also been used as an MLH retrieval method when applied to S-band radar returns (Lange et al., 2015; Tanamachi et al., 2019). In a different context, Barrera-Verdejo et al. (2016), combined brightness-temperature information from a MWR and water-vapour mixing-ratio Raman lidar profiles in order to derive absolute humidity vertical profiles.

Most of the previous work done for ML retrieval using backscattered lidar signals or temperature profiles has been focused on "stand-alone" retrieval methods only. However, tentative derivation of a synergistic algorithm spanning the full diurnal cycle and the study of the uncertainty sources associated to MLH estimation and their statistical impact on the retrievals has not received much attention (LeMone et al., 2018).

To fill this void, this paper focuses on synergistic retrieval of MLH estimates with low uncertainty by combining ceilometer and MWR MLH-based retrievals using the EKF and the parcel method as respective estimators. Towards this end, this paper aims to study: (i) the performance of these two commonly-used algorithms under different atmospheric scenarios, (ii) the impact of key error sources,

namely, measurement and retrieval errors, on MLH estimates and (iii) evaluate the performance of the proposed synergistic ceilometer-MWR method. The simplified processing chain of the ceilometer and MWR data is summarised in Fig. 3.1.

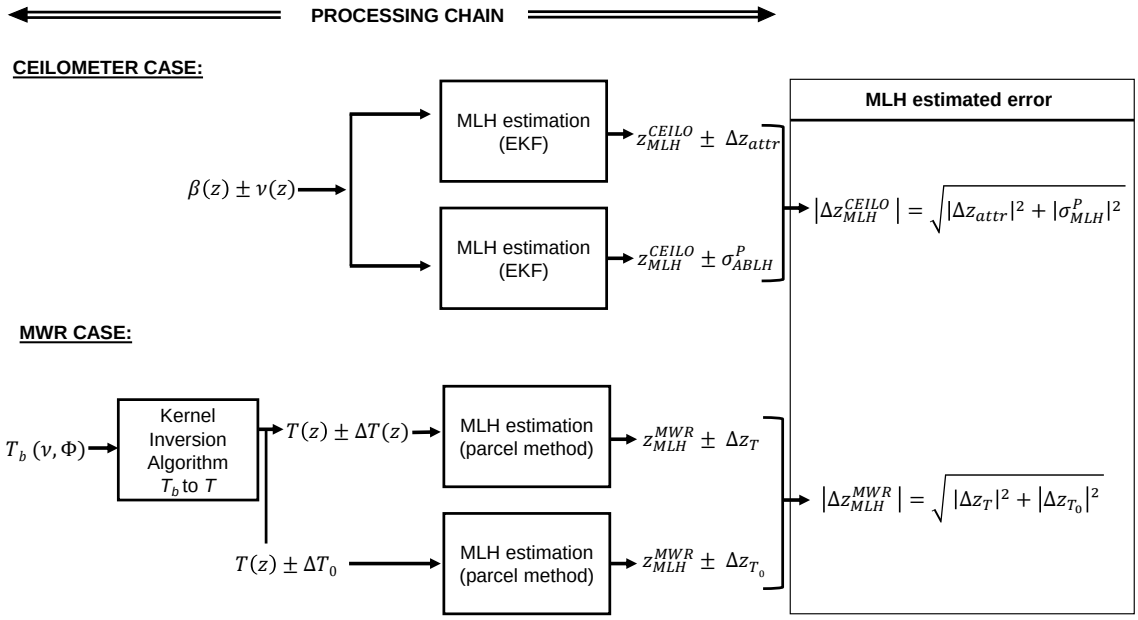

Figure 3.1: Block diagram illustrating the ceilometer (top) and MWR (bottom) processing chains used to estimate the mixing-layer height (MLH) and related error estimates. z is the vertical coordinate (height). $\beta(z)$ is the attenuated backscatter, $\nu(z)$ is the related corrupting noise, z_{MLH}^{CEILO} is MLH-LC-EKF, Δz_{attr} is the uncertainty of MLH-LC-EKF due to incorrect layer attribution, and σ_{MLH}^{P} is the MLH error component due to noise. $T_b(\nu, \phi)$ is the MWR brightness temperature measured at frequency ν and elevation angle ϕ, $T(z)$ is the retrieved temperature profile, Δz_T is the MLH-MWR error component due to the total uncertainty of $T(z)$, Δz_{T_0} is the MLH-MWR error component due to uncertainty in the auxiliary measured surface temperature T_0. Δz_{MLH}^{CEILO} and Δz_{MLH}^{MWR} stand for the total estimated error for MLH-LC-EKF and MLH-MWR, respectively.

This paper is organised as follows: Sect. 3.2 introduces instruments and data sets. Sect. 3.3 revisits the proposed MLH estimation methods and related error sources, assesses their uncertainties on the MLH estimates via error propagation from both ceilometer- and MWR-based methods, and introduces the synergistic method. Sect. 3.4 presents statistical analysis and discussion of results based on 20 days selected from the HD(CP)^2 Observational Prototype Experiment (HOPE) (Macke et al., 2017) campaign. Finally, Sect. 3.5 gives concluding remarks.

Owing to the various combinations of boundary layer terminology, instruments, and methods used in this paper, we provide an acronym table for ease of reference

(Table 3.1).

Table 3.1: List of acronyms and abbreviations used throughout this Chapter.

Acronym	Definition
ABL	Atmospheric boundary layer
CBL	Convective boundary layer
ML	(Well-)mixed layer
FT	Free troposphere
EZ	Entrainment zone
RL	Residual layer
MLH	Mixed layer height
CBH	Cloud base height
MTT	Morning transition time
ETT	Evening transition time
JOYCE	Jülich ObservatorY for Cloud Evolution
HOPE	HD(CP)^2 Observational Prototype Experiment
MWR	Microwave radiometer
LC	Lidar ceilometer
DWL	Doppler wind lidar
RS	Radiosonde
EKF	Extended Kalman filter
VVSTD	Vertical Velocity Standard Deviation
MLH-MWR	MLH estimated by application of the parcel method to MWR measurements
MLH-LC-EKF	MLH estimated by application of the EKF method to LC measurements
MLH-DWL	MLH estimated by application of the VVSTD method to DWL measurements
MLH-RS	MLH estimated by application of the parcel method to RS measurements
SYN	Synergistic method optimally combining MLH-MWR and MLH-LC-EKF
MLH-SYN	MLH estimated by the SYN method

3.2 Instruments and data set

This Chapter uses data from the HOPE campaign. For brevity, the instruments and parameters used here are summarised in Table 3.2. Refer to Sect. 2.1.4 for a detailed review of the related instruments.

Table 3.2: Main specifications of the instruments from the HOPE campaign which will be used in this PhD. (1) Humidity And Temperature PROfiler. (2) 50 m adjacent to the surface and 500 m above 5000 m.

Instrument	Measured Parameter	Sounding range	Wave-length	Raw spatial resolu-tion	Raw temporal resolution
Jenoptik CHM-15k ceilometer	Attenuated backscat-ter $[m^{-1}sr^{-1}]$	350-1000 m	1064 mm	15 m	15 s
Vaisala CT25K ceilometer		60-7000 m	1064 nm	30 m	15 s
DWL (Halo Stream Line XR)	Vertical air velocity [m/s]	15-10000 m	1500 nm	30 m	2 s
HATPRO MWR (1)	Brightness tempera-ture [ºC]	0-10000 m	$6 \sim 5$ mm (V-band, 51-58 GHz)	50-500 m (2)	∼2.7 min

3.3 Methods and uncertainties of MLH estimation

When comparing ceilometers and MWRs, the instruments at the focus of this paper, ceilometers typically have higher vertical resolution (e.g., 15 m for the Jenoptik CHM-15k Nimbus ceilometer versus 50 m or greater for the MWR). Because the ceilometer relies on attenuated backscatter returns from atmospheric aerosols and molecules, which are proxies of the thermodynamic state of the atmosphere, to identify the MLH, layer-attribution problems are very common. On the other hand, MWR-derived temperature profiles have a much coarser vertical resolution than profiles from LCs (Sect. 3.2). Additionally, parcel method-based MLH estimates suffer from uncertainties associated with surface temperature Δz_{T_0}. We now explore these sources of uncertainty in greater detail.

3.3.1 MLH estimation from ceilometer data

MLH estimation method

Several classical methods for LC-based MLH estimation, such as the gradient method (Endlich et al., 1967; Flamant et al., 1997), the inflection-point method (Menut et al., 1999) and the variance method (Hooper & Eloranta, 1986), among others (Melfi et al., 1985; Boers & Eloranta, 1986), are based on the detection of a meaningful ML-to-FT sharp transition in the vertical profile of the attenuated backscatter coefficient. However, thermal updrafts, intermittent turbulence, and measurement noise often lead to time-inconsistent MLH retrievals even in single aerosol layer scenarios. Apart from noise, these fluctuations represent real physical processes in the atmosphere, but they can complicate MLH tracking. To counteract detrimental effects of these fluctuations on MLH tracking, backscatter profiles are often time and/or height averaged (Lange et al., 2014). Therefore, temporal resolution of LC-based MLH estimates is usually relatively low ($\sim$ 30 min). LC-based algorithms for MLH estimation (in convective and stable regimes) in recent literature (Collaud Coen et al., 2014; de Bruine et al., 2017; Poltera et al., 2017) use time-continuity and morphological criteria based on a combination of empirically-tuned gradient and variance criteria, signal and SNR conditions, and climatological data.

In this study, we apply the EKF MLH estimation method (Lange et al., 2014, 2015), which departs from previous works of (Rocadenbosch et al., 1999), using a time-adaptive, optimal predictive model to delineate the shape of the sharp ML-to-FT transition (Fig. 3.2a). The Kalman filter is essentially the Wiener solution (Wiener, 1964) of the optimal filter problem in which one wants to compute a statistical estimate of an unknown signal (the MLH as a function of time) using a related signal (i.e., the ceilometer attenuated backscatter height profile as a function of time) to produce the estimate as an output. The two main distinguishing features of the Kalman filter formulation are: (i) vector modelling of the random processes under study (i.e., the MLH and shape parameters defining the ML-to-FT transition as a function of time), and (ii) recursive processing of the input noisy measurements (the ceilometer's) at each successive discrete time. This time-adaptive behaviour of the filter is based on minimization of the mean squared error over time of the so-called *a posteriori* error covariance matrix (the term *a posteriori* meaning "once the filter is updated with the present-time measurement", i.e., from the ceilometer). The reader is referred to (Lange et al., 2014, 2015) for a complete derivation of the EKF-based method for MLH tracking in LC data (hereafter,

MLH-LC-EKF), particularly Appendix A of (Lange et al., 2014) for a summary of the filter's constitutive equations and proof of its optimality. In following Sect. 3.3.1 the MLH-LC-EKF is briefly summarised for self-contained purposes and notation definition.

As a result, MLH-LC-EKF (Lange et al., 2014) enables consistent time-tracking of the MLH without need of averaging techniques or training from ancillary climatological records. Because the filter estimates are generated at the same temporal and spatial resolution of the input measurement data, the filter can even be implemented as a real-time processor. Best performance of the EKF with reference to the classical methods above has been shown in (Lange et al., 2014; Banks et al., 2015, 2016) with reference to different parameterizations of the WRF model.

Review of the MLH-LC-EKF

Central to the MLH-LC-EKF method is the assumption of the erf-like ML-to-FT model,

$$h(z; z_{MLH}, a, A, c) = \frac{A}{2}\left\{1 - erf\left[\frac{a}{\sqrt{2}}(z - z_{MLH})\right]\right\} + c, \tag{3.1}$$

where z_{MLH} is the MLH, a is a scaling factor related to the entrainment zone (EZ) thickness ($2.77a^{-1}$) (Flamant et al., 1997; Cohn & Angevine, 2000), A is the total backscatter coefficient, and c is the free troposphere (FT) molecular backscatter background, which acts as an offset term to the filter.

The erf model depicted in Fig. 3.2a models the ML-to-FT transition of the attenuated backscatter coefficient measured by the ceilometer. This model is used as a proxy of the total atmospheric backscatter coefficient under the assumption of clear-to-moderately cloudy sky conditions (optical thickness, $\tau < 1$). The shape parameters of this model profile along with the MLH parameter itself give rise to the formulation of the state vector (to be estimated),

$$\boldsymbol{x}_k = [z_{MLH,k}, a_k, A_k, c_k]^T, \tag{3.2}$$

where subscript k is a discrete time. $z_{MLH,k}$ is the key parameter of interest, and a_k, A_k, and c_k are auxiliary parameters determining the change in shape of the ML-to-FT interface with time.

The *state-vector model* represents the transition of the state vector from time t_k to t_{k+1}. It is formulated as

$$\boldsymbol{x}_{k+1} = \boldsymbol{x}_k + \boldsymbol{w}_k, \tag{3.3}$$

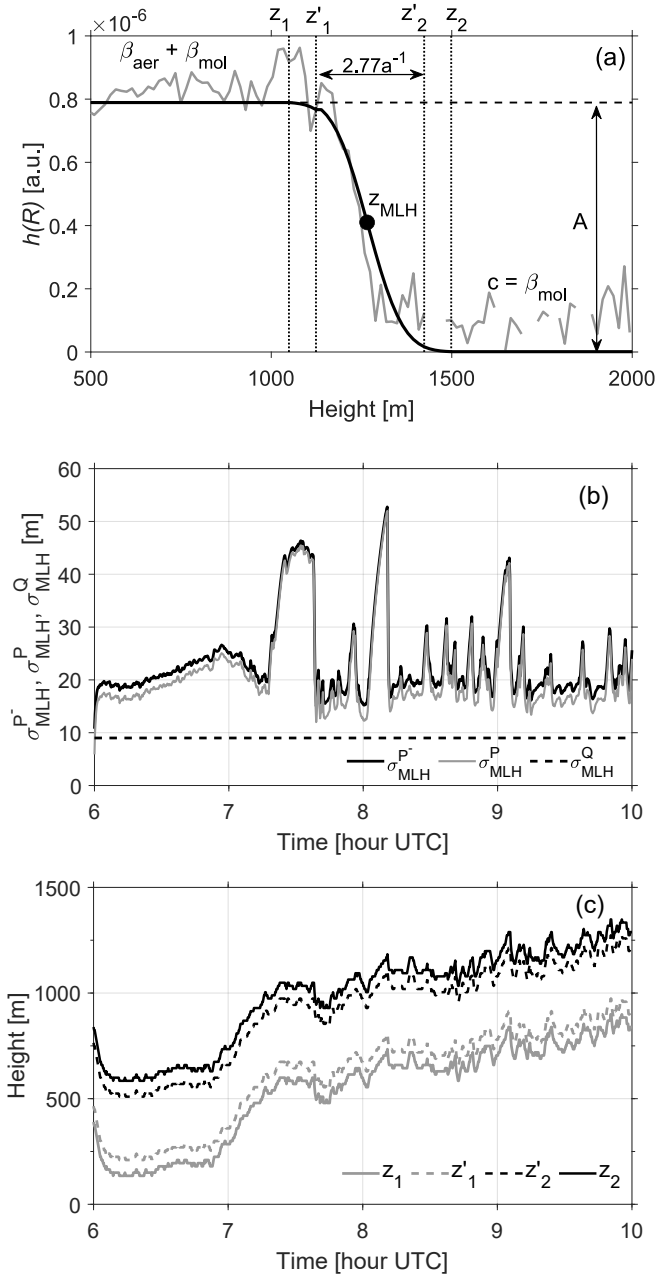

Figure 3.2: Example of the MLH-LC-EKF estimation technique (20 April 2013, 0600-1000 UTC). (a) The ML-to-FT transition model. (Grey trace) Example of background-subtracted attenuated backscatter-coefficient profile measured by the LC. (Black curve) Fitted erf-model profile described in (Lange et al., 2014). (b) MLH-LC-EKF *a priori* error, σ^{P-}_{MLH}, *a posteriori* error, σ^{P}_{MLH}, and state-noise standard deviation, σ^{Q}_{MLH} as a function of time. (c) Temporal evolution of search boundaries z_1, z'_1, z'_2 and z_2.

where $\boldsymbol{w}_k$ is the state-noise vector with diagonal covariance matrix, $\boldsymbol{Q}_k = \boldsymbol{E}[\boldsymbol{w}_k \boldsymbol{w}_k^T]$, where $\boldsymbol{E}$ denotes the ensemble mean (or expectation) operator (Barlow, 1989).

For enhanced filter stability (Reif et al., 1999), $\boldsymbol{Q}_k$ is modelled in stationary diagonal form as $\boldsymbol{Q} = diag[\boldsymbol{\sigma_Q^2}], \boldsymbol{\sigma_Q} = [\sigma_{z_{MLH}}, \sigma_a, \sigma_A, \sigma_c]$, where $\sigma_{z_{MLH}}, \sigma_a, \sigma_A$ and σ_c are the guessed standard deviations associated with the state-vector components, $z_{MLH},\ a,\ A$ and c, respectively. For example, $\sigma_{z_{MLH}}$ models the standard deviation of the MLH (a random variable) around its mean value. In practice, for simplicity, the input vector $\boldsymbol{\sigma_Q}$ is constructed as

$$\boldsymbol{\sigma_Q} = \mu_Q \hat{\boldsymbol{x}}_{\boldsymbol{0}}^{-}, \tag{3.4}$$

where μ_Q is the so-called Q-intensity factor (a scalar) and $\hat{\boldsymbol{x}}_{\boldsymbol{0}}^{-}$ denotes the initial guess of the state vector at filter start-up, to be specified by the user. In what follows, we have used $\mu_Q = 0.1$ (10%). This means that if we assume an initialization $z_{MLH,0} = 1500$ m then we expect MLH fluctuations of approximately ± 150 m (10%) at 1σ.

Because the state vector is recursively recomputed at each filter step, an intensity factor $\mu_Q = 0.1$ is usually more than sufficient to search the full ML height span. Increasing this factor above 10% increases the search "nervousness" of the filter. This effect is usually not beneficial because it may lead the filter to jump between different aerosol layers and, hence, be more prone to divergence. The initial guess vector $\hat{\boldsymbol{x}}_{\boldsymbol{0}}^{-}$ can easily be estimated by plotting the erf model against one measured ceilometer attenuated backscatter profile as in Fig. 3.2a.

The *measurement model* relates the ceilometer measurement vector, $\boldsymbol{y_k}$, to the state-vector as

$$\boldsymbol{y_k} = h(\boldsymbol{x_k}) + \boldsymbol{v_k}, \tag{3.5}$$

where h is the erf-like ML-to-FT function model given by Eq. 3.5 above, $\boldsymbol{v_k}$ is the observation noise at time t_k with noise covariance matrix, $\boldsymbol{R}_k = \boldsymbol{E}\left[\boldsymbol{v_k}\boldsymbol{v_k^T}\right]$, and z is the vertical range. The measurement vector, $\boldsymbol{y_k} = (y_{1,k}, y_{2,k}, \ldots, y_{N,k})$ is the noise-corrupted ceilometer attenuated backscatter signal at discrete ranges, $z = z_i, i = 1 \ldots N$. Because there is only one single measurement realization available at each time $\boldsymbol{t_k}$, the instantaneous noise covariance matrix $\boldsymbol{R}_k$ is estimated in piece-wise form over range cells instead of time cells as described in (Lange et al., 2015), Eq. (19). The nonlinear model of Eq. 3.5 is linearised through its Jacobian, which is passed to the filter.

Error sources

There are two key sources of uncertainty concerning MLH estimation from ceilometer data: (i) layer-attribution errors and (ii) noise-induced errors.

(i) Impact of layer-attribution errors on the estimated MLH, Δz_{attr}

Layer-attribution errors arise from the existence of multiple layers or gradients in the attenuated backscatter profile. Depending upon the number of layers and their separation, the estimated MLH can be significantly different from the actual MLH. For example, during the evening transition time (ETT; also called the afternoon-to-evening transition or AET, see (Wingo & Knupp, 2015)) under quiescent conditions, the ML is replaced by the residual layer (RL) (Stull, 1988). In this case, it often happens that the MLH-LC-EKF estimate follows the RL because RL-to-FT aerosol gradient characteristics are similar to those of the ML top (Haeffelin et al., 2012) , particularly in the 1–2 hr period following local sunset. Provision of acceptable initial guesses for the state-vector, $\hat{\boldsymbol{x}}_0^-$, state-vector covariance, $\boldsymbol{Q}$, and a priori state-vector error covariance matrix, $\boldsymbol{P_0^-}$, are key to preventing layer-attribution errors. This is especially true during the morning transition time (MTT, i.e., at and after local sunrise), when the ML starts to develop and there are relatively steep backscatter aerosol gradients between the ML and the RL or FT above. An example of this phenomenon is illustrated in Fig. 3.3a. Previous work on assessing the uncertainty of the MLH estimate due to layer-attribution errors has been carried out by (Haeffelin et al., 2012).

The *a priori* and *a posteriori* error-covariance matrices are defined as

$$\boldsymbol{P}_k^- = \boldsymbol{E}\left[\boldsymbol{e}_k^- \boldsymbol{e}_k^{-T}\right], \; \boldsymbol{P}_k = \boldsymbol{E}\left[\boldsymbol{e}_k \boldsymbol{e}_k^{T}\right], \tag{3.6}$$

respectively, where $\boldsymbol{e_k^-} = \boldsymbol{x_k} - \hat{\boldsymbol{x}}_{\boldsymbol{k}}^-$ is the *a priori* error and $\boldsymbol{e_k} = \boldsymbol{x_k} - \hat{\boldsymbol{x}}_{\boldsymbol{k}}$ is the *a posteriori* error, i.e., before and after assimilating the current measurement ($\boldsymbol{y_k}$). Here, $\boldsymbol{x_k}$ is the true atmospheric state (unknown) and $\hat{\boldsymbol{x}}_{\boldsymbol{k}}^-$ and $\hat{\boldsymbol{x}}_{\boldsymbol{k}}$ are the *a priori* and *a posteriori* state vectors estimated by the filter, respectively.

Covariance matrices $\boldsymbol{P_k^-}$ and $\boldsymbol{P_k}$ are updated with each successive step of the recursive loop of the filter (Fig. 3.2b) as a function of the current information available to the filter at time t_k (actual Kalman or projection gain, $\boldsymbol{K}_k$, linearised Jacobian, state vector, $\boldsymbol{x}_k$, state-vector covariance matrix, $\boldsymbol{P}_k$, and measurement-noise covariance matrix, $\boldsymbol{R}_k$) as well as initial settings at t_0. The initial guess of the a priori state-vector error covariance matrix, $\boldsymbol{P}_0^-$, is a rough estimate of the uncertainty associated with the initial guess of the state vector, $\hat{\boldsymbol{x}}_{\boldsymbol{0}}^-$, in the form of a diagonal matrix $\boldsymbol{P_0^-} = diag\left[\boldsymbol{\sigma_P^2}\right], \boldsymbol{\sigma_P} = (\sigma_{e,z_{MLH}}, \sigma_{e,a}, \sigma_{e,A}, \sigma_{e,c})$, where $\sigma_{e,X}, X = [z_{MLH}, a, A, c]$ represents the assumed uncertainty of the initial guess,

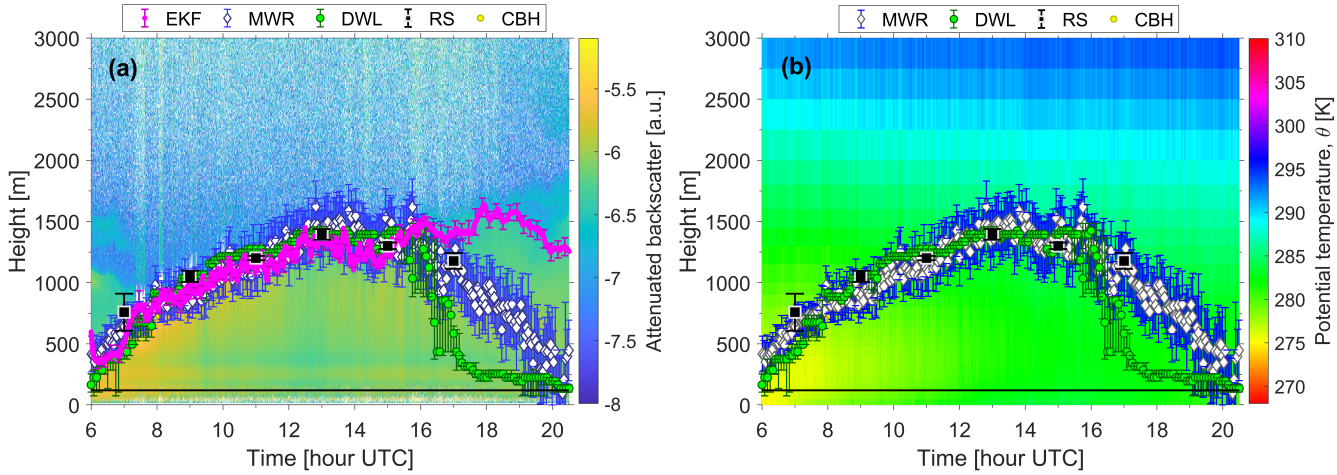

Figure 3.3: (a) Attenuated ceilometer backscatter (in a.u.) measured by the Jenoptik CHM-15 and (b) MWR-retrieved potential temperature (in K) for 20 April 2013 at Jülich, Germany. In panel (a), magenta dots (along with noise-related error bars) represent MLH-LC-EKF. In both panels, white diamonds represent MLH-MWR with associated uncertainty Δz_{MLH}^{MWR} (blue error bars); black squares are MLH-RS; green dots MLH-DWL; and yellow dots are CBH estimates from the Vaisala CT25. In both panels, the solid black line represents a lower bound (120 m) on MLH-DWL.

$\hat{\boldsymbol{x}}_{\boldsymbol{0}}^{-} = [z_{MLH,0}, a_0, A_0, c_0]^T$ at 1σ level. $\boldsymbol{\sigma_P}$ is shorthand notation for $\boldsymbol{\sigma}_{\boldsymbol{P}_0^-}$. We compute the input vector $\boldsymbol{\sigma_P}$ as

$$\boldsymbol{\sigma_P} = \mu_P \hat{\boldsymbol{x}}_{\boldsymbol{0}}^{-}, \tag{3.7}$$

where μ_P denotes the P-intensity factor, to be specified by the user. Factors in the range $\mu_P = 0.1 - 0.3 (10 - 30\%)$ have been used in the examples of Sect. 3.4, with $\mu_P = 0.3$ the default setting. High/low values $(0.3/0.1)$ tend to increase/decrease the search span of the filter during the first iterations. For example, assuming $z_{MLH,0} = 1500$ m, the setting $\mu_P = 0.3$ tells the filter that the user expects the MLH to be roughly at 1500 ± 450 m at filter start up. $P-$ and $Q-$intensity factors are partially coupled parameters because of the recursive nature of the filter and, therefore, the guidelines above are just orientative. Layer-attribution errors are common because, irrespective of the user's initializations for $\hat{\boldsymbol{x}}_{\boldsymbol{0}}^{-}$ and $\boldsymbol{\sigma_P}$, successful filter operation is always conditioned to the existence of aerosol gradients. Therefore, Δz_{attr} can only be known by comparison to a reference instrument (e.g., the radiosonde).

(ii) Impact of observation noise and resulting a posteriori error on the estimated MLH, σ^{P}_{MLH}

Noise-induced errors are due to the presence of noise in $\beta'(z)$ and propagate an error to the MLH-LC-EKF estimate. The recursive loop of the EKF provides by itself convenient error estimates ($\boldsymbol{P}_k^-$, $\boldsymbol{P}_k$ and $\boldsymbol{Q}_k$) of the estimated state vector and, therefore, of the estimated MLH at each discrete time t_k.

Fig. 3.2b shows the estimated *a priori* and *a posteriori* errors for the case shown in Fig. 3.3 computed as the time-dependent standard deviations, $\sigma^{P^-}_{MLH,k}$, $\sigma^{P}_{MLH,k}$, respectively. These are compared to the time-static state noise standard deviation, σ^{Q}_{MLH}. Standard deviations $\sigma^{P^-}_{MLH,k}$, $\sigma^{P}_{MLH,k}$ and $\sigma^{Q}_{MLH,k}$ are computed as the square root of the first diagonal element of these matrices during the recursive loop of the filter. The error of the instantaneous MLH-LC-EKF estimate at time t_k is given by the *a posteriori* error as

$$\sigma^{EKF}_{MLH,k} = \sigma^{P}_{MLH,k} \,, \tag{3.8}$$

which is the key error indicator of interest. In Fig. 3.2b, it can be seen that the a posteriori error magnitude, $\sigma^{P}_{MLH,k}$, is always smaller than the *a priori* error, $\sigma^{P^-}_{MLH,k}$. This variance reduction, $\left(\sigma^{P}_{MLH,k}\right)^2 < \left(\sigma^{P^-}_{MLH,k}\right)^2$, means that the assimilation of the present measurement $\boldsymbol{y_k}$ counteracts the detrimental effects of observation noise. The latter term merges into a single body both measurement noise $v(z)$ (with $\boldsymbol{R_k}$ being estimated run time) and modelling noise (i.e., approximation of the ML-to-FT transition by the erf model used in MLH-LC-EKF). $\sigma^{Q}_{MLH,k}$ is just a reference baseline of the user's assumed MLH variability. Fig. 3.2c depicts time evolution of search boundaries z_1, z_1', z_2' and z_2 (Fig. 3.2a) during the first four hours of data processing (Lange et al., 2014).

The error estimates above are obviously subordinated to filter convergence and tracking of the ML-to-FT interface (i.e., no attribution errors). Otherwise, the total error from sources (i) and (ii) above can be calculated by using the error superposition principle as (see Fig. 3.1)

$$\left|\Delta z^{CEILO}_{MLH}\right| = \sqrt{\left|\Delta z_{attr}\right|^2 + \left|\sigma^{P}_{MLH}\right|^2}. \tag{3.9}$$

3.3.2 MLH estimation from DWL data

To estimate the MLH from DWL measurements, the standard deviation of time-height profiles of vertical velocity are calculated every 5 min within a ± 15 min window. Second, the standard deviation is corrected for instrument noise (Lenschow

et al., 1980). Finally, the MLH is estimated as the first height at which the Vertical Velocity STandard Deviation (VVSTD) falls below a predetermined threshold (Schween et al., 2014; Tucker et al., 2009; Träumner et al., 2011) (hereafter, MLH-DWL).

Useable thresholds for VVSTD range from 0.2 m s^{-1} to 0.4 m s^{-1} (Tucker et al., 2009; Träumner et al., 2011). Based on the work of (Schween et al., 2014), who studied the sensitivity of the mixing layer height derived from different thresholds, here we use a 0.4 m s^{-1} threshold. Because 0.4 m s^{-1} is at the high end of the accepted range, it represents a major source of uncertainty.

DWL-based estimates of ML height (MLH-DWL) are generally limited to daytime hours, when the boundary layer is turbulent due to solar heating and thermally-driven ML overturn. MLH-DWLs at night are less reliable because aerosol content is reduced in stable situations at night. Additionally, mixing layer height values below 120 m AGL are rejected as the DWL is not sufficiently sensitive below this height.

The uncertainty associated with the DWL-derived MLH is estimated by applying a 25% variation to the nominal threshold ($th_{\pm} = 0.4$ m·s^{-1} ± 0.1 m·s^{-1}) (Schween et al., 2014). Upper and lower uncertainty bounds are derived from the MLH estimations using 0.5- and 0.3-m·s^{-1} thresholds, respectively, minus the MLH estimation using the nominal 0.4 m·s^{-1} threshold. Formally,

$$\sigma_{MLH,k}^{DWL,\pm} = \left| z_{MLH,k}^{DWL\ (th=0.4\pm0.1)} - z_{MLH,k}^{DWL\ (th=0.4)} \right|, \tag{3.10}$$

where the plus *(minus)* superscript in $\sigma_{MLH,k}^{DWL,\pm}$ denotes the upper *(lower)* uncertainty bound, which is computed by inserting threshold $th = 0.4 + 0.1$ m·s^{-1} *($th = 0.4 - 0.1$ $m{\cdot}s^{-1}$)* in the first term of the right hand side of Eq. (3.10) above. A similar approach was previously employed by Villalonga et al. (2020).

3.3.3 MLH estimation from MWR data

MLH estimation method

The parcel method is commonly used for MLH estimation using potential temperature data (Holzworth, 1964; Seibert et al., 2000). For a given profile of physical temperature, $T(z)$, retrieved from brightness measurements, the first step is to convert it to potential temperature profile, $\theta(z)$, by using

$$\theta(z) = T(z) \left(\frac{p_0}{p(z)} \right)^{\frac{R}{C_p}}, \tag{3.11}$$

where p_0 is the surface atmospheric pressure, $p(z)$ is the atmospheric pressure profile, $R = 287\,\mathrm{J \cdot K^{-1} \cdot kg^{-1}}$ is the universal gas constant, and $\mathrm{C_p} = 1004\,\mathrm{J \cdot K^{-1} \cdot kg^{-1}}$ is the specific heat capacity for dry air at a constant pressure (Wallace & Hobbs, 2006b). Physically, the potential temperature represents the temperature an air parcel at an altitude z would have if it were lowered, dry adiabatically, to the surface. In the parcel method, the MLH is defined as the lowest point in a given potential temperature profile for which $\theta(z) > \theta(0)$, where $\theta(0)$ is the surface value of the potential temperature. Small scale effects (e.g., surface properties and shielding of the sensor) can bias the estimate of surface temperature $T(0) = \theta(0)$, to which the parcel method is very sensitive (Collaud Coen et al., 2014; Seidel et al., 2010).

Changes in $\theta(z)$ with respect to height, $\frac{d\theta}{dz}$, are indicative of the stability of the atmosphere with respect to displacement of unsaturated air parcels. The atmosphere is stable when $\frac{d\theta}{dz} > 0$, neutral when $\frac{d\theta}{dz} = 0$, and unstable when $\frac{d\theta}{dz} < 0$. Under quiescent conditions in daytime, the mixed layer (ML) is characterized by continuous convective mixing, driven from below by buoyant thermal plumes from the relatively warm surface and, sometimes, from above, by evaporatively driven downdrafts initiated within clouds in the EZ. As a result of this continuous mixing, the interior of the ML exhibits nearly uniform temperature and moisture throughout most of its depth. Thus, $\frac{d\theta}{dz} = 0$ in the ML, and negative in the surface layer (unstable), $\frac{d\theta}{dz} < 0$. At the top of the ML, an increase in temperature and reduction in moisture delineates the EZ, i.e., a transition layer between the ML and the FA. The MLH is typically computed as falling halfway between the top of the ML and the bottom of the FA, near where the magnitudes of the temperature and/or moisture gradients are maximized.

While the parcel method was designed for use with sounding data, Stull (1988) (p. 474) cautions against estimating MLH using only a single radiosounding. This is because a single radiosounding may not be representative of average conditions in a horizontally heterogeneous ML, as would be the case in a convectively active BL characterized by thermal updrafts and downdrafts. MWR offers a partial solution to this issue in that it provides a time series of potential temperature profiles. Temporal averaging can ameliorate to some extent the perturbations caused by individual updrafts and downdrafts, allowing longer-term (e.g., ∼O(30 min–1 hr)) trends in MLH to be discerned.

To estimate the MLH from MWR data, first, MWR potential-temperature profiles are interpolated to a uniform vertical resolution of 10 m. Second, a five-point (50 m) moving average is applied to smooth the profiles (Schween et al., 2014).

Then, the MLH-MWR is derived by using as surface temperature reference, $\theta(0)$, that from the JOYCE meteorological tower at 2 m, thus assuring reliable retrievals (Collaud Coen et al., 2014). The tower-derived temperature, which has a raw temporal resolution of 6 min, is interpolated to the MWR temporal resolution (2.7 min).

In Fig. 3.3, we present an example comparison of MLH-LC-EKF (Fig. 3.3a) with MLH-MWR (Fig. 3.3b). In spite of the relatively coarse spatial resolution (which decreases with height) of the MWR potential temperature profiles, it can be seen that MLH-MWR follows the overall trend of the radiosonde-derived MLH, and particularly during morning (0600-1000 UTC) and evening (1600-1900 UTC) transition times MTT and ETT, respectively. The MLH-MWR captures the collapse of the convective BL during the latter period, after sunset, while the MLH-LC-EKF estimate continues to follow the elevated RL.

Error estimation

The uncertainty associated with MLH-MWR has been approximated by two main error sources (Fig. 3.1): (a) the total uncertainty in the retrieved temperature profile $T(z)$ and consequent error propagated to the MLH calculation, which gives rise to a MLH error, Δz_T, and (b) the uncertainty in the estimated surface temperature, T_0 (or, equivalently, $\theta(0)$), which gives rise to a MLH error, Δz_{T_0}.

(a) Assessment of the MWR-retrieved temperature-profile error in the estimated MLH, Δz_T: A study on the performance of the retrieved temperature profile (Crewell & Löhnert, 2007) using a long-term data set of representative atmospheric profiles and noise levels found uncertainty in the 0.1–0.5 K range. A synthetic brightness temperature data set generated from over 10 000 radiosoundings (of which 5334 were used for training and 4954 were used as a validation data set) was used to test the performance of the statistical retrieval algorithm (analogous to multi-regression algorithm (Löhnert & Crewell, 2003)). Altitude-dependent temperature uncertainties, $\Delta T(z)$, were generated, varying from 0.44 K on the ground to 1.60 K at 4 km. An example of the height-dependent temperature-retrieval kernels is given in Fig. 7 of (Löhnert & Maier, 2012).

In order to assess the uncertainty of MLH-MWR due to temperature-retrieval errors, Δz_T, we adopt the following approach: At each time instant, the retrieved height-dependent temperature errors, $\Delta T(z)$ are converted into potential-temperature errors, $\Delta\theta(z)$. These are added to and subtracted from the retrieved potential temperature profile, resulting in delineation of its "upper" and "lower" error bounds. In this approach, the uncertainty in the temperature profile acts like a

bias, i.e., a consistent under- or over-estimation throughout the profile (see also (Löhnert et al., 2009)).

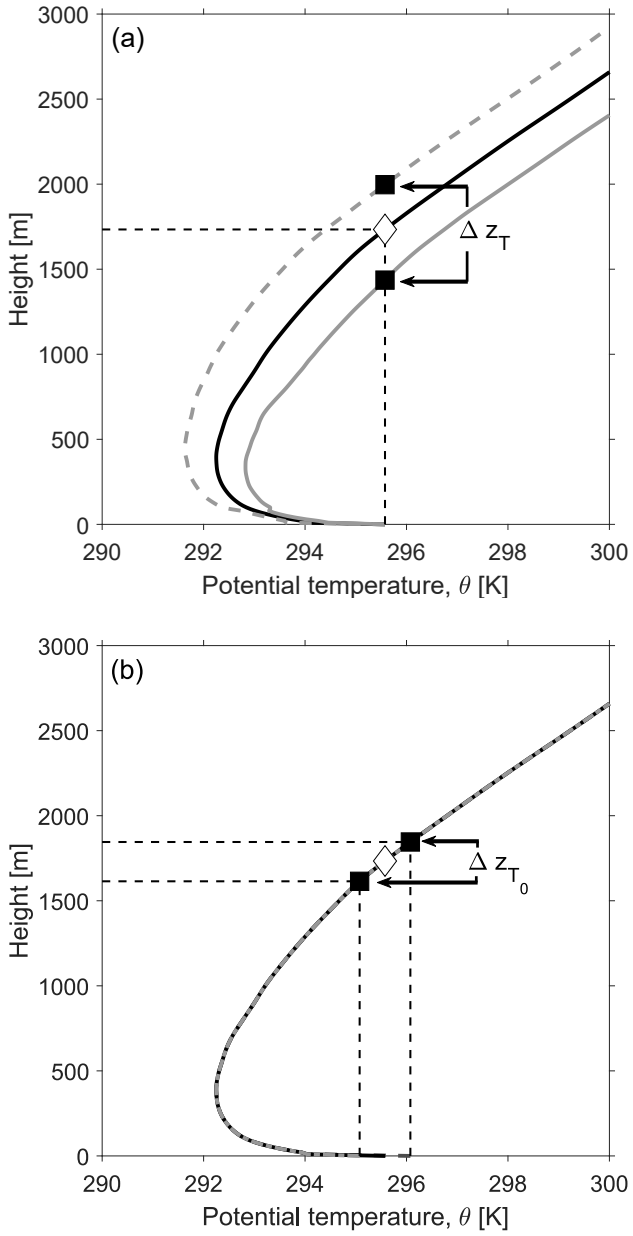

Figure 3.4: Overview of MLH-MWR (parcel method) estimation errors (24 April 2013, 1401 UTC, Jülich, Germany). (a) MLH-MWR error arising from the uncertainty inherent in the MWR retrieval of the temperature profile, Δz_T. Upper (dashed grey)- and lower (solid grey)-bound profiles are obtained by adding and subtracting the height-dependent temperature error-perturbation profile, $\Delta\theta(z)$, to the nominal potential-temperature profile, $\theta(z)$ (solid black line). The white diamond represents MLH-MWR obtained from the nominal profile, and the black squares are corresponding MLH-MWR obtained from the perturbed profiles. (b) MLH-MWR error due to the uncertainty in the measured surface temperature, Δz_{T_0}, obtained by adding and subtracting 0.5 K from the reference temperature.

The parcel method is then applied to all three of these profiles (Fig. 3.4a): (i) $\theta_{MWR}(z) + \Delta\theta(z)$, or the upper error-bound profile for the potential temperature, (ii) $\theta_{MWR}(z)$, or the nominal profile, and (iii) $\theta_{MWR}(z) - \Delta\theta(z)$, or the lower error-bound profile, and consequently, a MLH error bar is obtained. Fig. 3.4a shows an example error bar calculation for the temperature profiles retrieved from HATPRO MWR measurements at Jülich, Germany at 1401 UTC on 24 April 2013. It can be observed that retrieval errors on the order of less than 2 K throughout the vertical profile introduce an uncertainty of about $\Delta z_T \approx 500$ m in the MLH estimates.

(b) Assessment of surface-temperature errors on the estimated MLH, Δz_{T_0}: Following a similar perturbation approach, the uncertainty of the estimated MLH due to surface-temperature errors Δz_{T_0} is calculated by adding and subtracting the approximate uncertainty in the surface temperature (± 0.5 K) (Crewell & Löhnert, 2007) to T_0. Fig. 3.4b shows three resulting MLH estimations. As a result of this perturbation in the surface temperature T_0, the uncertainty in the MLH is about 150–300 m.

Finally, the total error from error sources (a) and (b) above is computed by error superposition (Fig. 3.1) as

$$\left|\Delta z_{MLH}^{MWR}\right| = \sqrt{\left|\Delta z_T\right|^2 + \left|\Delta z_{T_0}\right|^2} \tag{3.12}$$

3.3.4 MLH estimation from radiosonde data

The procedure to estimate the nominal MLH from RS data is the parcel method (refer to Sect. 3.3.3). RS-MLH errorbars are derived in similar fashion to Sect. 3.3.3.b assuming $\pm$ 0.5 K surface temperature uncertainty. Unlike the uncertainty for temperature profiles $T(z)$ retrieved from MWR, however, the uncertainty associated with RS-measured $T(z)$ is not altitude dependent, but constant ($\pm$ 0.5 K) with height. Thus, $\left|\Delta z_{MLH}^{RS}\right| = \pm$ 150–300 m.

3.3.5 30-min averaged MLH retrievals and error assessment

In order to inter-compare MLH retrievals in a meaningful statistical sense we standardize MLH-LC-EKF, MLH-MWR, and MLH-DWL to a common temporal resolution of 30 min via Maximum Likelihood (MaxL) as (Rocadenbosch et al., 2020)

$$MLH_X(t_h) = \frac{\sum_k z_k/\sigma_k^2}{\sum_k 1/\sigma_k^2}, \tag{3.13}$$

where X stands for the instrument or method used ($X = EKF$, MWR, DWL), t_h is the center time of the 30-min time window ($t_h = 0630, 0700, \ldots, 2000$ UTC), z_k (formally, $z_k = z^X_{MLH,k}$) is the instantaneous MLH estimated at time $t_k \in [t_h - 15\,\text{min}, \ldots, t_h + 15\,\text{min}]$, i.e., with the raw temporal resolution of the instrument/method X, and σ_k (formally, $\sigma_k = \sigma^X_{MLH,k}$) is the associated uncertainty of MLH estimate z_k. σ_k is computed via Eqs. (3.8), (3.12) and (3.10) for the MLH-LC-EKF, MLH-MWR, and MLH-DWL, respectively.

The associated 30-min MLH uncertainty is computed as

$$\sigma_X(t_h) = \sqrt{\sigma^2_{X_1}(t_h) + \sigma^2_{X_2}(t_h)}, \tag{3.14}$$

where σ_{X_1} is the standard deviation of the estimated MLH by instrument or method X (a proxy of the instantaneous MLH variability),

$$\sigma_{X_1} = std(z_k) \tag{3.15}$$

and σ_{X_2} is the uncertainty associated with the MLH estimation by instrument or method X,

$$\sigma_{X_2}(t_h) = \sqrt{\frac{1}{\sum_k 1/\sigma^2_k}}. \tag{3.16}$$

In Sect. 3.4, intercomparisons of 30-min MLH will be performed on pairs of instruments. Bias between instruments X and Y is computed as

$$bias^{X,Y}(t_h) = MLH_X(t_h) - MLH_Y(t_h), \tag{3.17}$$

and bias variability as

$$\sigma^{X,Y}_{bias}(t_h) = \sqrt{\sigma_X(t_h)^2 + \sigma_Y(t_h)^2}. \tag{3.18}$$

3.3.6 The ceilometer-MWR synergistic (SYN) method

The MLH-LC-EKF and MLH-MWR methods feature contrasting behaviours as exemplified in Fig. 3.3a. On one hand, MLH-MWR uncertainties span several hundred meters (blue error bars), and expand with height as a consequence of the MWR coarser spatial resolution at higher altitudes. On the other hand, MLH-LC-EKF have much smaller uncertainties (magenta error bars), on the order of tens of meters, which lie within those of MLH-MWR when the ABL is well developed (e.g., 1000–1400 UTC). However, during the ETT (1500–1800 UTC), MLH-LC-EKF detaches from the ABL, following the RL, instead.

Accordingly, we are motivated to introduce a synergistic MLH estimation method (SYN), which yields an optimal MLH estimate (MLH-SYN) that improves upon MLH-MWR and MLH-LC-EKF estimates considered in isolation. The SYN method combines the 30-min MLH retrievals and associated uncertainties of these two methods as follows: the MLH estimate provided by the synergistic method, MLH_{SYN}, is computed as

(i) the maximum likelihood between MLH-LC-EKF and MLH-MWR as

$$MLH_{SYN}(t_h) = \frac{\frac{MLH_{EKF}(t_h)}{\sigma^2_{EKF}(t_h)} + \frac{MLH_{MWR}(t_h)}{\sigma^2_{MWR}(t_h)}}{1/\sigma^2_{EKF}(t_h) + 1/\sigma^2_{MWR}(t_h)} \quad if\ I_{EKF}(t_h) \cap I_{MWR}(t_h) \neq \emptyset \tag{3.19}$$

in two situations:

(a) when their respective MLH uncertainty intervals (Eq. (3.14)), $I_{EKF}(t_h) = [\![MLH_{EKF}(t_h) - \sigma_{EKF}(t_h), MLH_{EKF}(t_h) + \sigma_{EKF}(t_h)]\!]$ and $I_{MWR}(t_h) = [\![MLH_{MWR}(t_h) - \sigma_{MWR}(t_h), MLH_{MWR}(t_h) + \sigma_{MWR}(t_h)]\!]$ overlap at least partially (i.e., Eq. (3.19)), or

(b) when t_h falls in a strongly convective period, I = [1000 – 1400] UTC. I corresponds to mid-afternoon at the JOYCE site, when, assuming quiescent atmospheric conditions, the CBL reaches is maximum depth and maturity. In a more generalized formulation, I would be location-dependent.

The associated uncertainty for the synergistic MaxL estimate of Eq. (3.19) above is given by

$$\sigma_{SYN}(t_h) = \sqrt{\frac{1}{1/\sigma^2_{EKF}(t_h) + 1/\sigma^2_{MWR}(t_h)}}. \tag{3.20}$$

(ii) The MLH-MWR estimate elsewhere (i.e., out of statements (i.a) and (i.b) above). Formally,

$$\begin{cases} MLH_{SYN}(t_h) = MLH_{MWR}(t_h) \\ \sigma_{SYN}(t_h) = \sigma_{MWR}(t_h) \end{cases}. \tag{3.21}$$

In this latter case, the uncertainty of the MLH-SYN is equal to that of MLH-MWR (Eq. (3.14)).

Eq. (3.19) is essentially the MaxL definition given by Eq. (3.13) but applied to each pair of MLH estimates, EKF and MWR, at each 30-min time step, t_h. The SYN method is discussed next in Sect. 3.4.1.

In case (i), this formulation balances MLH-LC-EKF and MLH-MWR estimates by attributing higher weight to the estimates with lower uncertainty. Typically, MLH-LC-EKF is favored during the mid-afternoon peak in convective boundary layer growth. Case (ii) typifies MLH development or decay during MTT and ETT, respectively. During these periods, MLH-LC-EKF and MLH-MWR tend to diverge, and the SYN method retains MLH-MWR as the most reliable estimate. This constraint ensures that the SYN method avoids MLH-LC-EKF tracking the RL (i.e., layer-attribution error).

3.4 Discussion

30-min MLH-SYN estimates are compared to MLH-LC-EKF, MLH-MWR and MLH-DWL (Sect. 3.3) considered in isolation with reference to MLH-RS. The statistical analysis is limited to the 0600-2030 UTC time interval, which delineates the CBL diurnal cycle including MTT and ETT over the JOYCE site. Sect. 3.4.1 discusses the synergistic method in the context of one "textbook" clear-day example, Sect. 3.4.2 gives an overview of the campaign dataset, and Sect 3.4.3 evaluates performance statistics of the different MLH retrieval methods for the whole campaign.

3.4.1 Synergistic method example

Case day 20 April 2013 (Fig. 3.3a) is used to exemplify the synergistic method retrieval in Fig. 3.5a. MLH estimates derived from the different methods are plotted with 30-min resolution (Eq. 3.13). This day was characterized by a cloud-capped mixing layer from 0700 to 1100 UTC and by clear sky otherwise. For visual reference in the plots next, MTT is defined as [0600–1000) UTC, ETT as [1400–2030) UTC, and peak convective boundary layer growth time as [1000–1400) UTC. Solar noon at JOYCE is 1130 UTC.

From 0600 to 0800 UTC, MLH-LC-EKF, MLH-MWR and MLH-DWL track closely with one another but fall below MLH-RS (Fig. 3.5a). The MLH-LC-EKF agreed well with MLH-MWR, despite the presence of aerosols in the 500–1000 m layer. In contrast, MLH-DWL fell slightly below MLH-MWR because of the relatively weak turbulence in the early morning, and the the use of a constant VVSTD threshold

(Sect. 3.3.2). MLH estimates from all methods coincided from 0800 to 1500 UTC. In other words, during most of this interval (case (i.a) in Sect. 3.3.6), the MLH-LC-EKF and MLH-MWR errorbars (computed as the $\pm 3\sigma$ value from Eq. (3.14)) partially or totally overlapped and hence, the MLH-SYN) was the MaxL estimate between the MLH-LC-EKF and MLH-MWR retrievals in isolation (Eq. 3.19) with an associated uncertainty given by Eq. (3.20).

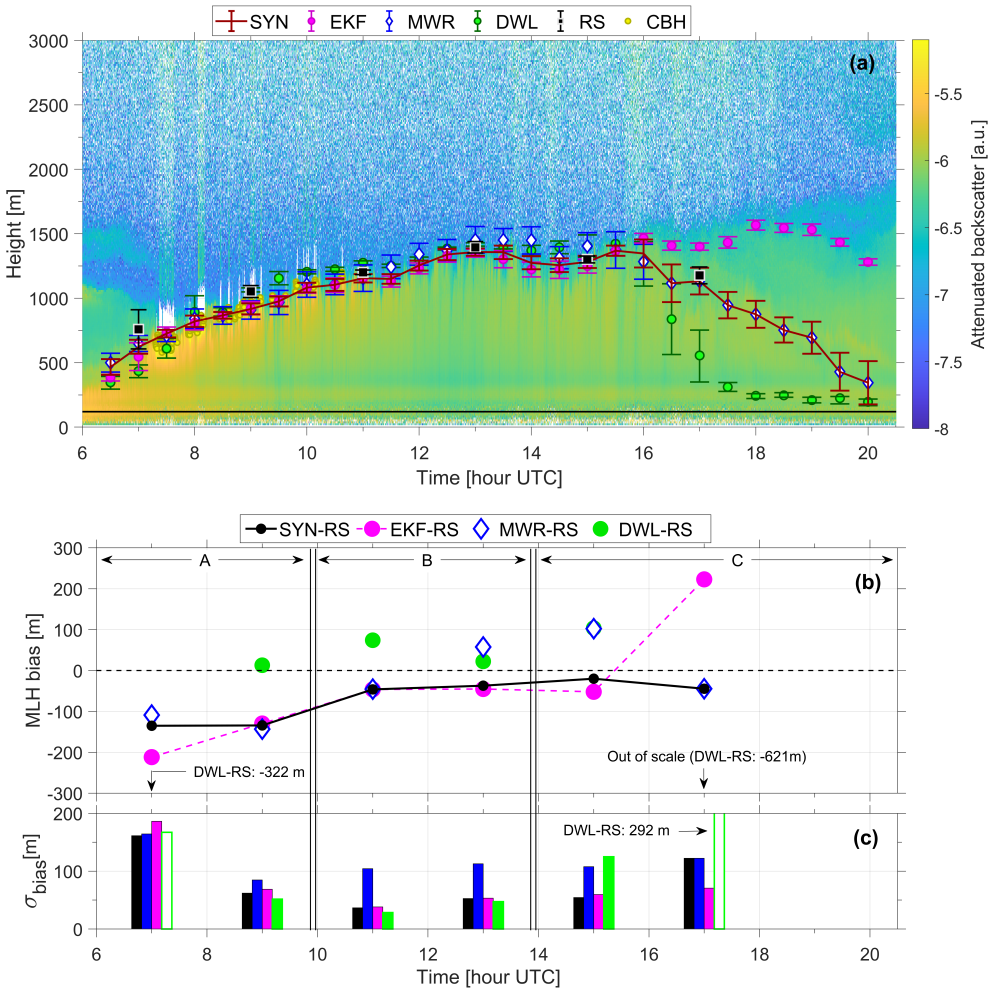

Figure 3.5: Performance of the SYN algorithm and MLH-LC-EKF, MLH-MWR, and MLH-DWL methods in isolation with reference to MLH-RS estimates as function of hour of day (case 20 April 2013, Fig. 3.3). (a) 30-min MLH estimates (Eq. (3.13)). (b) MLH bias (Eq. (3.17)). (c) MLH bias variability (Eq. (3.18)). Labels A, B, and C indicate typical MTT, peak convective, and ETT intervals, respectively (Sect. 3.4.1).

During the strongly convective interval, 1000 to 1400 UTC (case (i.b) in Sect. 3.3.6), the ML-to-FT gradient was sharply defined, and reliability of MLH-LC-EKF increased, with values closer to MLH-RS. In this interval, the ML was free from

layer attribution errors, and the MLH-SYN was constrained to the MaxL value between MLH-LC-EKF and MLH-MWR, irrespective of whether their individual error bars overlapped (e.g., at 1400 UTC). The latter shows the case of thermal updrafts causing MLH-MWR and MLH-DWL to jump slightly above the smoother MLH-LC-EKF time series. As a result of the smaller MLH-LC-EKF error bars during this interval, the MLH-SYN followed MLH-LC-EKF and inherited its smaller uncertainty (Eq. 3.20).

After 1500 UTC (i.e., the start of the ETT), each MLH estimate started to develop a distinct behaviour: MLH-DWL fell quickly as thermal turbulence decayed, whereas MLH-MWR decreased smoothly, thus coinciding with the radiosonde at 1700 UTC. In contrast, MLH-LC-EKF kept on tracking the elevated aerosol layer, which became the RL. In this situation, MLH-SYN followed MLH-MWR (case (ii) in Sect. 3.3.6, with MLH-SYN error bars overlapping MLH-MWR error bars (plotted in dark red and blue, respectively, in Fig. 3.5a), therefore avoiding layer-attribution errors typical of MLH-LC-EKF in the ETT.

Bias performance of the different MLH estimation methods with reference to MLH-RS are shown in Fig 3.5b. MLH-SYN and MLH-MWR (labeled SYN-RS and MWR-RS, respectively) yielded bias (Eq. 3.17) of less than $\pm$150 m during the whole period (0600–1400 UTC). Additionally, MLH-SYN bias variability (Eq. 3.18) was always lower than that of MLH-MWR (Fig 3.5c, SYN-RS and MWR-RS bars), which increases our confidence in the SYN algorithm. In the highly convective time interval B, it is evident that the MLH-LC-EKF bias variability is much lower than that of MLH-MWR (Fig 3.5c, EKF-RS and MWR-RS bars). MLH-DWL bias in the 0900–1500 UTC interval (corresponding to the well-developed ML) was $\pm$ $\sim$100 m, comparable to MLH-SYN bias. However, outside of this interval (e.g., at 0700 and 1700 UTC, empty green circles) MLH-DWL bias dramatically increased to 300 and 600 m, respectively. As mentioned in Sect. 3.3.2, this is a consequence of using a constant VVSTD threshold.

3.4.2 Dataset overview

Having examined a single case day in detail, we now expand our analysis to consider the entire data set from the 31-day HOPE campaign (01 April to 06 June 2013), which included 80 radiosondes.

Twenty-one days were selected from this set with a total of 55 radiosondes available. Selected days were either clear-sky days (cloud cover below 3 km lower than 10%, 8 days) or cloudy days (cloud cover below 3 km not greater than 70%, 13

days): Clear-sky days included days with single (Fig. 3.5a) or multiple aerosol layers (Fig. 3.6a) in the transition times. Cloudy days were characterized by a cloud-capped BL (Fig. 3.6b), sometimes with additional midlevel clouds well above the BL (Fig. 3.6c). Eight of the selected days included light drizzle events (< 0.5 mm/h, < 30 min/event, accumulated rain (0600-2000 UTC) < 0.1 mm), which usually occurred during MTT or ETT. Excluded days (10) were days with cloud cover below 3 km greater than 70% (7 days) and rainy days (rain intensity $>= 0.5$ mm/h, 2 days).

During the period of peak CBL growth (1000–1430 UTC), CBHs are usually at the same height as the MLH (Fig. 3.6b), as is common in the spring and summer time (Schween et al., 2014). MLH-RS using the parcel method overestimated the MLH at 11, 13 and 15 UTC by some 300 m, which motivated us to compare MLH-RS with the MLH retrieved using another thermodynamically-based alternative, the Bulk Richardson Number method (Schween et al., 2014). Like the parcel method, the Bulk Richardson Number method is also based on the temperature profile, but less sensitive to perturbations in the surface temperature, T_0. For consistency when computing statistics for the whole campaign, we retain MLH-RS using the parcel method.

Virga (precipitation streamers attached to the base of the clouds, e.g., in Fig. 3.6c from 1730-2000 UTC) were also problematic for MLH-LC-EKF, which tended to track the sharp gradient at the cloud tops from 1800 UTC onwards. Because cloud cover strongly changes the incoming solar radiation and, consequently, ML growth, cloudy days are particularly challenging for MLH-DWL, which uses VVSTD as a proxy of the turbulent mixing. Qualitatively, the SYN algorithm delineated fairly well the typical ML diurnal cycle (Fig. 3.6a-c).

3.4.3 Performance statistics

In this subsection, statistical measures of central tendency and variability for the 21-day sample considered are used to demonstrate superiority of MLH-SYN over MLH-MWR and MLH-LC-EKF estimates considered in isolation. Definitions for the statistical indicators are given in Appendix A.

During the course of this research, it was found that MLH-DWL performance statistics for the whole campaign are inferior to those of the other MLH estimation methods, mainly because MLH-DWL is hampered by the use of a fixed VVSTD threshold. In particular, during MTT and ETT, intermittent turbulence tends to cause MLH-DWL instability if the threshold is not adjusted. Dynamic adjustment

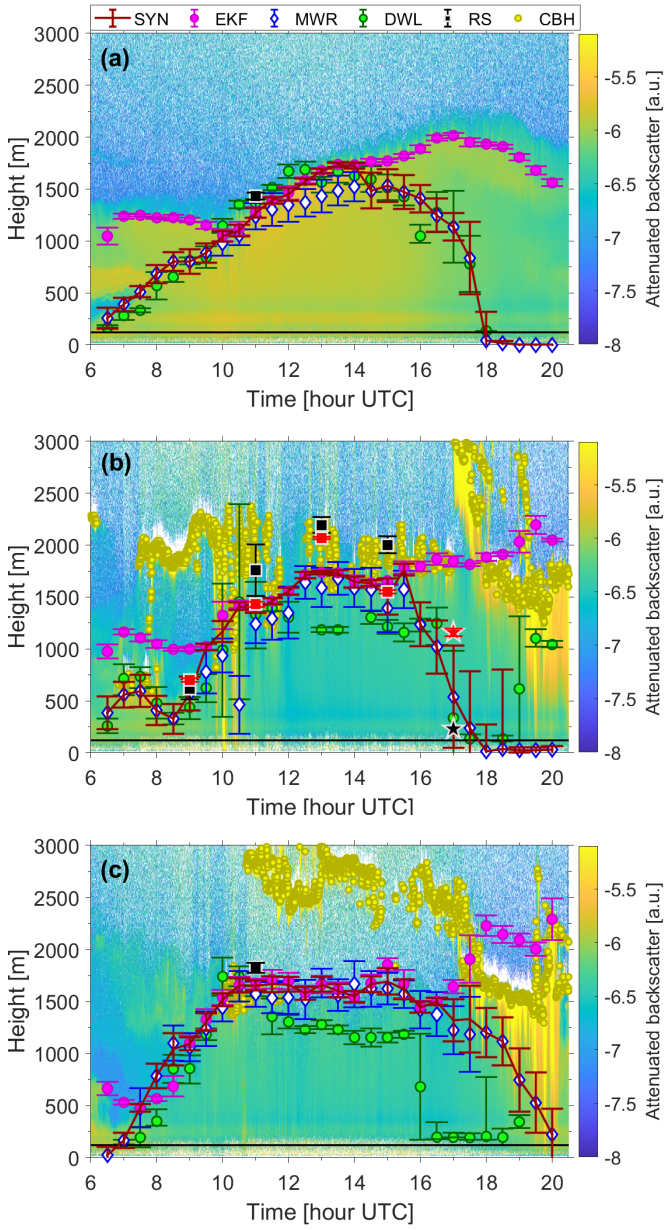

Figure 3.6: As in Fig. 3.5a, but representing the three typical atmospheric modes observed during the HOPE campaign: (a) Clear-sky day (22 April 2013) showing multiple aerosol layers from 0600 to 1000 UTC; (b) partially cloud-capped boundary layer day (13 April 2013); and (c) midlevel cloud day (16 May 2013) with virga from 1730 to 2000 UTC. In panel (b), red squares are MLH estimates made using Bulk Richardson Number (BRN) derived from RS $\theta(z)$ profiles. Black and red stars at 1700 UTC indicate the stable BL height estimates retrieved by the gradient method and BRN, respectively.

of the VVSTD threshold in MLH-DWL falls beyond the scope of the present work. MLH-DWL performance characteristics will nonetheless be reported in this study

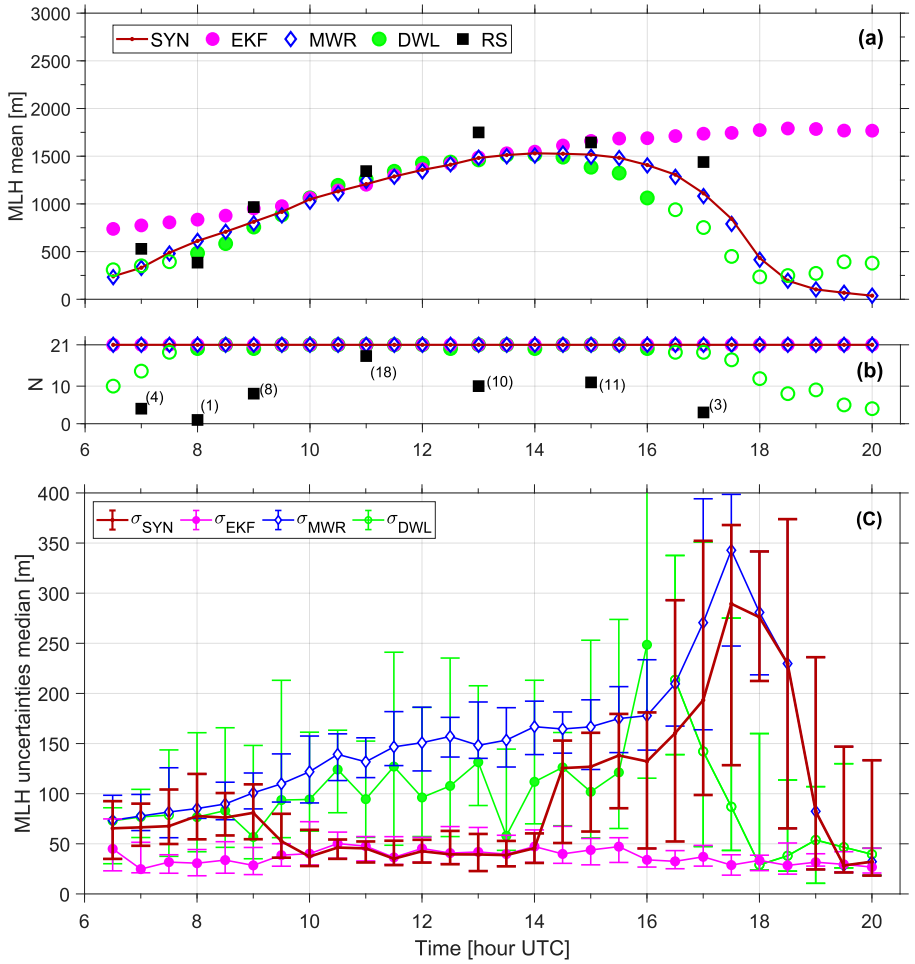

Figure 3.7: Means and uncertainties of 30-min MLH estimates over the selected 21 clear-sky days as a function of hour of day in UTC (LT=UTC+1h). (a) (Top panel) means (Eq. (B.0.1)) of MLH-SYN (red solid trace), MLH-LC-EKF (magenta dots), MLH-MWR (white diamonds), MLH-DWL (green dots) and MLH-RS (black squares). (b) Number of case days (out of 21 total days) used to compute mean values. (c) Median values (markers) and interquartile ranges (bars) of the 30-min MLH uncertainties (Eq. 3.14).

in order to motivate future research in this area.

I. MLH estimates by the different methods: MLH estimates averaged over the selected 21 days as a function of hour of day (local time) are shown in Fig. 3.7a. While both MLH-MWR and MLH-EKF methods were based on 21 samples (one for each hour, each day; Fig. 3.7b), MLH-DWL furnished fewer samples during MTT (0600-0800 UTC) and ETT (1600-2030 UTC) , open green circles). In these time intervals, MLH-DWL was often < 120 m, and such estimates were rejected as outliers by the reasoning discussed in Sect. 3.3.2.

The best agreement among all MLH estimation methods occurred from 1000 to 1400 UTC. As previously mentioned, this is the interval in which, under quiescent conditions, intensive, thermally driven convection deepens the CBL and, consequently, MLH reaches its highest altitudes of the daily cycle (Stull, 1988). The MLH-LC-EKF attribution-layer error clearly evidenced during MTTs and ETTs, during which the SYN algorithm successfully took over. From 0600 to 0900 UTC, the MLH-LC-EKF exceeded MLH from other estimators, revealing that MLH-LC-EKF retrievals were frequently affected by the persistent aerosol layers from the previous night. During early the morning, the MLH-SYN followed MLH-MWR. Both rose in concert with MLH-RS 0700 and at 0900 UTC. MLH-SYN, MLH-MWR and MLH-DWL rose together until 1400 UTC. As exemplified by previously discussed case of 20 April 2013 (Fig. 3.5), the disagreement among all MLH estimation methods grew sharply from 1500 UTC onwards (i.e., the start of the ETT), when the turbulence decayed, the CBL separated from the RL, and the stable boundary layer began to form in response to the reversal of surface radiative flux. MLH-LC-EKF tracked this RL. While MLH-DWL properly tracked the turbulence decay, it exhibited worse agreement than MLH-MWR with MLH-RS at 1700 UTC (Fig. 3.7a).

30-min MLH estimation uncertainty (Eq. (3.14)), as a function of hour of day is shown in Fig. 3.7c by computing medians and interquartile ranges (25-to-75-th percentiles) for the total sample of 21 days. MLH-LC-EKF exhibited much lower medians (by $\approx$ 40 m) and spreads than MLH-MWR in all hours of the strongly convective period (e.g., $\approx$ 140 m, 1000–1400 UTC). This result further favours the SYN algorithm during this interval.

II. Performance of the SYN method and of MWR and EKF methods in isolation with reference to RS retrievals:

MLH bias vs. RS - MLH mean bias (Fig. 3.8a, Eq. (B.0.3)) is computed as the difference between the 21-day means of MLH-SYN, MLH-MWR, MLH-DWL and MLH-RS estimates in a 30-min time window centred at the RS launch time.

MLH-SYN and MLH-MWR yielded mean biases less than $\pm$ 150 m overall (SYN-RS and MWR-RS labels in Fig. 3.8a, respectively), and -150 m during the convective interval (*B*; 1000–1400 UTC). The latter is consistent with the findings of (Banks et al., 2015) (Fig. 4a therein) who estimated bias of $\approx$ 200 m for MLH-LC-EKF. As expected, MLH-LC-EKF (EKF-RS label in Fig. 3.8a) performed poorly outside the 1000–1400 UTC convective interval (*B*), during the MTT and ETT. Its

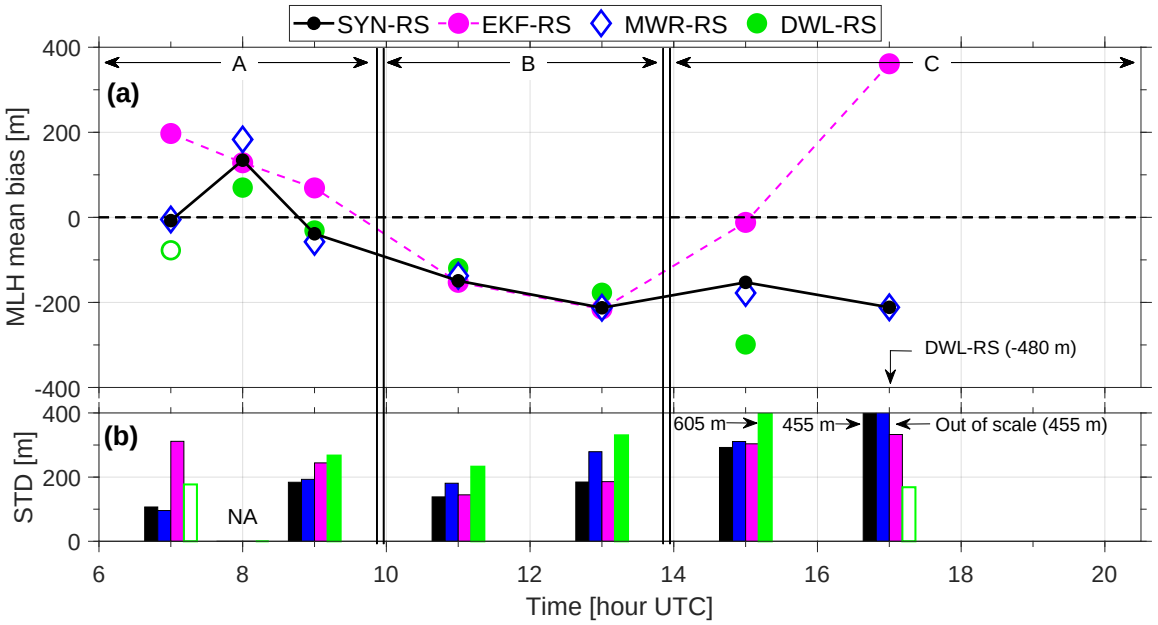

Figure 3.8: Biases relative to MLH-RS of the 30-min MLH estimations over the selected 21 clear-sky days as a function of hour of day in UTC. (a) Mean biases. Label "X-RS" (X=SYN, EKF, MWR, DWL) stands for the mean bias $\mu_{bias}^{X,RS}(t_h)$ (Eq. (B.0.3)) between an instrument/method combination X and MLH-RS. (b) Mean biases standard deviation $\sigma_{bias}^{X,RS}(t_h)$ (Eq. (B.0.4))

V-shaped mean bias curve reaches +200 and +400 m at 0700 and 1700 UTC, respectively.

MLH bias-to-RS variability.- MLH bias-to-RS variability (Fig. 3.8b) is computed as the standard deviation (STD) given by Eq. (B.0.4). Because all the MLH estimates are subject to the same atmospheric, day-to-day variability, comparative differences in bias STD among them are attributable to their individual performance. Therefore, each hourly set of vertical bars ranks the different MLH estimation methods by bias performance with reference to RS. Thus, in the convective interval (1000-1400 UTC) MLH-LC-EKF and MLH-SYN had the lowest bias STD (EKF-RS and SYN-RS labels, respectively). In contrast, during TTs, MLH-MWR and MLH-SYN exhibited the lowest bias STD. In summary, the the SYN algorithm performed best over the whole daily interval because it inherited the superior performance characteristics of its constituent methods. MLH-LC-EKF performance in TTs was – as expected – worst (Fig. 3.8a). MLH-DWL only gave usable estimates between 900-1500 UTC, and even then its performance (green bars) was always worse than that of the MWR (blue bars). Outside of this interval, there were retrieval issues (empty green dots) related either to the selection of a fixed VVTSD

threshold or MLHs below the instrument minimum measurable height of 120 m.

Correlation and regression analysis.- Fig. 3.9 compares the different MLH retrievals to MLH-RS (e.g., $X = MLH_{RS}$ and $Y = MLH_{MWR}$ in panel (a)). Two time intervals were investigated: *(i) One capturing the full daytime diurnal cycle* [0600-2030) UTC, which included 55 radiosondes, and *(ii) the shorter, strongly convective period in the local afternoon* [0930-1430) UTC, which included 28 radiosondes. MLH mean bias (MB) values in each of these two time intervals were comparable for both SYN and MWR methods. Additionally, the MB obtained in time intervals *(i)* and *(ii)* (red and blue text labels, respectively) for each method approximately coincided with the average of the hourly biases plotted in Fig. 3.8a in these intervals. The root-mean-square error (RMSE) was slightly lower for the SYN method ($RMSE^{(i)}_{SYN} = 247$ m, $RMSE^{(i)}_{MWR} = 278$ m, see labels) and relatively high for the DWL $RMSE^{(i)}_{SYN} = 393$ m. The latter value is in accordance with the RMSE of 359 m (0800-1600 UTC) reported by Schween et al. (2014). All RMSE indicators improved in convective time interval (ii) because of the lower variability of the MLH.

The significance of the indicators above warrant some comments. Gross outliers were particularly abundant during TTs. Gross outliers are defined as biased estimates (MLH_X-MLH_{RS}, X=SYN, EKF, MWR, DWL) above $\pm 1\sigma$ of the mean of the associated MLH bias histogram computed hourly. To further improve the significance of results, gross outliers were removed prior to evaluating correlation statistics via a similar procedure as that described in (Banks et al., 2015) and (Rocadenbosch et al., 2020). When Fig. 3.9 was regenerated after gross outliers were removed (not shown), the linear regression lines ("RL" subscript in Fig. 3.9) became virtually coincident with the 1:1 line, indicating virtually no bias. Furthermore, MLH-SYN remained superior to MLH-MWR and MLH-DWL. In the diurnal time interval *(i)* above, the SYN exhibited $\rho^{(i)}_{SYN,1\sigma} = 0.98$, $RMSE^{(i)}_{SYN,1\sigma} = 76\ m$, followed by the MWR, $\rho^{(i)}_{MWR,1\sigma} = 0.96$ and $RMSE^{(i)}_{MWR,1\sigma} = 103\ m$ and the DWL, $\rho^{(i)}_{DWL,1\sigma} = 0.95$ and $RMSE^{(i)}_{DWL,1\sigma} = 157\ m$. Over the convective time interval *(ii)*, the SYN achieved $\rho^{(ii)}_{SYN,1\sigma} = 0.99$ and $RMSE^{(ii)}_{SYN,1\sigma} = 41\ m$ (as compared to $\rho^{(ii)}_{MWR,1\sigma} = 0.94$ and $RMSE^{(ii)}_{MWR,1\sigma} = 86\ m$ prior to gross outlier removal).

3.5 Conclusions

A synergistic MLH retrieval algorithm combining MWR and ceilometer-based estimates was presented along with performance statistics covering 21 days of the

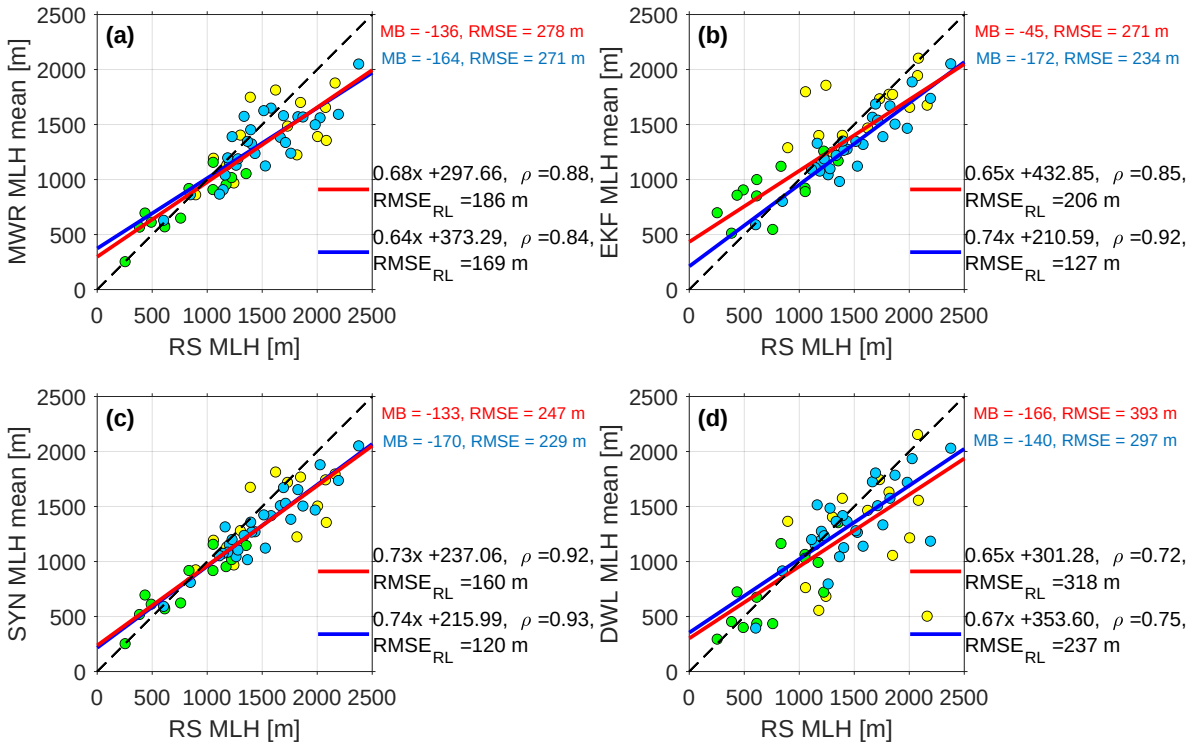

Figure 3.9: Scatterplot comparison of 21 clear-sky day, 30-min (a) MLH-MWR, (b) MLH-LC-EKF, (c) MLH-SYN and (d) MLH-DWL with MLH-RS. Green, blue and yellow dots depict MLH estimates in the [0600-0930), [0930-1430) and [1430-2030) UTC time intervals, respectively. Red and blue lines are regression lines over diurnal [0600-2030) UTC and convective [0930-1430) UTC MLH estimates, respectively. $RMSE_{RL}$ denotes regression-line root-mean-square error. For reference in all panels, the 1:1 line is drawn as a black dashed line. Mean bias (MB) and RMSE are annotated in colors corresponding to their respective time intervals.

HOPE campaign. The SYN method used a maximum-likelihood algorithm (Sect. 3.3.6) that combined MLH-LC-EKF and related error uncertainties in the strongly convective BL time interval (local afternoon, which at JOYCE is 1000–1400 UTC) with MLH-MWR and associated uncertainties outside of this interval. MLH-LC-EKF were derived from the ML-to-FT gradient in the attenuated backscatter profile by using a Kalman filter, yielding time-adaptive MLH estimates with a temporal resolution equal to that of the LC. MLH-MWR were estimated by the parcel method applied to MWR-derived temperature profiles.

The motivation for creating MLH-SYN, which combined MLH estimates by different methods, was the inherent weaknesses each method exhibited in isolation. Specifically, MLH-LC-EKF tends to track aerosol gradients, which led the

filter to follow RLs during MTT and ETT. The latter was the most common layer-attribution error. In experiments, the EKF was able to detect gradients as low as 1.5 to 1 times the mean FT level (Fig. 3.2a). Assuming no attribution errors, the MLH uncertainty was given by the *a posteriori* error of the filter (Sect. 3.3.1). We therefore formulated MLH-SYN to equal MLH-LC-EKF in the strongly convective afternoon interval (1000-1400 UTC). Outside this interval, MLH-MWR proved more reliable, with an uncertainty given by the inherent error in the MWR-retrieved temperature profile and parcel-method surface-temperature error (Sect. 3.3.3). MLH-DWL was excluded from the formulation of MLH-SYN; intermittent turbulence, particularly during the ETT, along with the assumption of a fixed VVSTD threshold, were major issues.

The variability in MLH estimation uncertainty matched that of its component algorithms (MLH-MWR and MLH-LC-EKF) as a function of time of day (Fig. 3.7b). Specifically, during the strongly convective interval (1000–1400 UTC), the MLH-SYN exhibited $\approx$ 40 m (median) as compared to $\approx$ 140 m by MLH-MWR, which indicates that SYN inherited the steady tracking performance of the MLH-LC-EKF. Outside this interval, the variability of MLH-SYN approached that of MLH-MWR.

Comparative performance of the different MLH estimation methods with reference to MLH-RS was also addressed. Statistical analysis over the 21-day sample showed that MLH mean bias was inflated by gross outliers associated with TTs and day-to-day atmospheric variability. Additionally, the parcel method (used in both MLH-MWR and MLH-RS) was particularly sensitive to the accuracy of surface temperature T_0. Non-representativeness of T_0 on specific days involving complex micrometeorological effects was a challenging difficulty. Nonetheless, with reference to radiosoundings (with and without outlier removal from the data collection), the SYN algorithm outperformed all other MLH estimation methods in isolation. In the *diurnal*$^{(i)}$⟦*convective*$^{(ii)}$⟧ time interval, MLH-SYN achieved a correlation coefficient $\rho^{(i)(ii)}_{SYN,1\sigma} \geq 0.98$ and RMSE, $RMSE^{(i)}_{SYN,1\sigma} = 76m$ ($RMSE^{(ii)}_{SYN,1\sigma} = 41\ m$). These results compare favorably to MLH-MWR alone: $\rho^{(i)(ii)}_{MWR,1\sigma} \geq 0.94$ and $RMSE^{(i)}_{MWR,1\sigma} = 103\ m$ ($RMSE^{(ii)}_{MWR,1\sigma} = 86\ m$).

To sum up, although SYN used the simplistic assumption of a fixed strongly convective time interval (1000–1400 UTC), the time-adaptive combination of two largely independent methods for MLH tracking, one based on aerosol gradient-based observations (MLH-LC-EKF) and the other temperature-based (MLH-MWR) has shown superior MLH tracking skill. Further research is planned to extend this methodology over the whole diurnal cycle, as well as to explore further synergy

with DWL sensors. Besides, a comparison of all the sources of uncertainty in terms of how they balance and propagate would be an interesting study for the remote sensing community.

Chapter 4

Assessing Obukhov length and friction velocity from floating lidar observations

This Chapter presents a parametric-solver algorithm - the so-called 2D method - for estimating atmospheric stability and friction velocity from floating Doppler wind lidar (FDWL) observations. The focus of the study is two-fold: (i) to examine the sensitivity of the computational algorithm to the retrieved variables and derived stability classes (the latter through confusion-matrix theory), and (ii) to present data screening procedures for FDWLs and fixed reference instrumentation at the IJmuiden test site.

4.1 Introduction

Over the past decades, wind energy (WE) has achieved an important position in the global energy market due to its technical improvements and relevant advantages in terms of environmental impact (Council, 2019; Gutiérrez-Antuñano, 2019). In particular, interest has been rising in offshore WE due to the strong homogeneous winds over the ocean (GWEC, 2016). Nowadays, offshore WE is one of the core technologies of the European roadmap to becoming carbon neutral (Carbon Trust, 2018). However, offshore wind farms still have very high production and deployment costs compared to onshore facilities (Hevia-Koch & Jacobsen, 2019a).

In order to reach the European goal of 150 GW of installed offshore WE capacity by 2030, efforts toward commercial competitiveness are being dedicated by the WE industry and research institutions (IRENA, 2019). Traditionally, the wind resource of potential wind farm areas has been characterized using meteorological masts planted on the seabed (Sathe & Mann, 2013). In some cases, the instrumentation on the masts can be used to assess the state of the atmosphere together with the wind resources. However, they also have very high production and deployment costs and cannot be re-placed once installed (WindPower, 2018).

In the past few years, Doppler wind lidars (DWLs) have been introduced as an alternative for masts due to their flexibility and cost-effectiveness (Gottschall et al., 2014). When deployed offshore atop buoys, floating DWLs (FDWLs) have a series of advantages over metmasts: an offshore metmast can easily cost millions of Euros and requires a long planning and construction period. FDWLs costs are in the hundreds of thousand Euro range and are not as demanding regarding the soil, environmental constraints, and construction time frames (Nicholls-Lee, 2013; Peña et al., 2013). In addition, a FDWL can easily be redeployed to other locations and thus cover larger areas (Pichugina et al., 2012). In the past few years, commercially available FDWLs have widely been deployed around the world and the reliability of their data has been proven, either as standalone instruments or collocated with masts to measure atmospheric- and sea-related parameters (Salcedo-Bosch et al., 2021b).

On the other hand, FDWLs suffer the influence of wave motion, which increases the variances of the reconstructed wind by the lidar (Salcedo-Bosch et al., 2021a; Tiana-Alsina et al., 2017; Kelberlau et al., 2020). However, within averaging periods typical of atmospheric measurements, i.e., 10 or 30 min, the error due to wave motion on the mean reconstructed wind vector are negligible (as they cancel out within such periods), as shown by multiple validation campaigns (Gutiérrez et al., 2015; Gutierrez-Antunano et al., 2017; Schuon et al., 2012; Mathisen, 2013; Gutiérrez-Antuñano et al., 2018).

FDWLs cannot generally assess the same number of atmospheric parameters as masts. Masts can host multiple sensors to assess several different atmospheric parameters, such as, temperature, pressure, humidity and turbulent fluxes, whereas FDWLs are generally limited to observe wind speed and wind direction (Campbell Scientific, 2016). Several authors have reported the influence of atmospheric stability on different aspects of the wind power generation, e.g., turbine power performance, wind shear, and wakes (Subramanian et al., 2018; Machefaux et al., 2016;

Kim et al., 2021). Ghaisas et al. (2017) compared different power laws to retrieve the wind-shear coefficient in order to extrapolate the wind speed to the turbine hub height. They concluded that when atmospheric stability information was included when extrapolating the wind speed, the results substantially improved, yielding to a predicted hub-height wind speed at worst biased by 5%.

Alblas et al. (2014) studied two offshore wind farms, Egmond aan Zee (OWEZ) and North Hoyle, and found that unstable conditions led to smaller wake losses, thereby yielding higher power output than near-neutral conditions. Fatigue loads over the wind turbine structure are often estimated by considering turbulence intensity and wind shear. However, many studies have reported a dependency of fatigue loads on atmospheric stability, which can be used in order to improve the load calculation accuracy (Kretschmer et al., 2018; Holtslag et al., 2016; Sathe et al., 2013).

The Obukhov length, L, a key parameter within the Monin–Obukhov similarity theory (MOST, (Monin & Obukhov, 1954)) is nowadays employed in wind energy to predict the vertical behavior of wind and to classify periods in different atmospheric stabilities (Subramanian et al., 2018; Barthelmie, 1999; Holtslag et al., 2015; Sathe et al., 2011). Computation of the Obukhov length requires the measurement of momentum and heat fluxes, which can be directly calculated from sonic anemometers.

There are different suggestions to estimate the Obukhov length in situations in which the experimental setup is limited. Beljaars et al. (1989) proposed a method to retrieve the Obukhov length based on MOST relationships by using the roughness length, the wind speed at one reference height, and the difference between air and sea-level temperatures. Their method was used, for instance, by Motta et al. (2005), who studied the influence of atmospheric stability on the power output of a potential wind farm. A similar approach, which relies on temperature and wind measurements at different levels, was extensively described by Holtslag et al. (2014). Basu (2018) proposed an optimization method to estimate the Obukhov length (without temperature measurements) from wind profile measurements at three heights. The method consists of Obukhov length optimization towards MOST. The optimization is achieved by a root finding algorithm accounting for the monotonic behavior of the vertical wind speed ratio with respect to the Obukhov length.

In the present work, we constructed a parametric solver algorithm along with a basic data screening procedure that, relying on FDWL measurements only and

MOST, enables the estimation of the Obukhov length and friction velocity. Additionally, a sensitivity study was conducted for the retrieved variables and estimated atmospheric stability classes. In contrast to the approaches by Holtslag et al. (2014) and Beljaars et al. (1989), the parametric algorithm assesses the atmospheric stability without needing temperature inputs. Complementary to the method proposed by Basu (2018), the proposed algorithm can be extended to an unlimited number of measurement heights.

The work is structured as follows: Section 4.2 describes the 3-month measurement campaign carried out at IJmuiden as well as the instrumental setup. Section 4.3.1 introduces the notation used in this work, Section 4.3.2 revisits MOST and atmospheric stability classifications. Section 4.3.3 describes the parametric solver algorithm. Sections 4.3.4 and 4.3.5 outline the derivation of the Obukhov length and friction velocity. Section 4.3.6 describes the data screening methods used to enhance measurement precision and data quality for both FDWL and the mast. Section 4.4 provides a discussion of the results and, finally, Section 4.5 provides our concluding remarks.

4.2 Materials

This Chapter uses data from the IJmuiden observational campaign. Refer to Sect. 2.2.3 for a detailed review of the related instruments.

4.3 Methods

4.3.1 Wind notation conventions

Wind measurements from the instruments above provided the three instantaneous wind vector components (u, v, and w) corresponding to the components in the horizontal x and y, and vertical z directions, respectively. Fluctuations u', v', and w' are defined as the difference between the actual instantaneous velocity components and their respective mean velocities, e.g., $u' = u - U$, where U is the mean value of u. Although we often use a Cartesian coordinate system so that the x, y, and z axes point north, east, and south, here, we align x along the wind direction. We skip usage of $\overline{U}$ to denote the mean wind component in order to avoid confusion with the vector notation $\overrightarrow{U}$, which is used to denote a specific set of HWS measurements in subsequent sections. We retain, however, usage of the over-bar, $\overline{(.)}$, to denote mean over time (10 min) for all other variables.

4.3.2 Surface-layer theory

The vertical wind gradient for a neutral, homogeneous, and stationary flow can expressed as (Panofsky, 1973)

$$\frac{\partial U}{\partial z} = \frac{u_*}{l}, \tag{4.1}$$

where u_* is the friction velocity and l is the mixing length (Peña et al., 2008). In the surface layer, which corresponds to the lowest 5–10% of the boundary layer, the magnitudes of stress and turbulent fluxes generally vary by less than 10% with height (Stull, 1988). Thus, within the surface layer, two assumptions are commonly made: (i) the friction velocity variation with height is negligible, and (ii) the mixing length increases with height as $l(z) = \kappa z$ (Peña & Gryning, 2008), where $\kappa \approx 0.4$ is the von Kármán constant. The logarithmic wind profile for neutral atmospheric conditions is the integral of Equation (4.1):

$$U(z) = \frac{u_*}{k} \ln\left(\frac{z}{z_0}\right), \tag{4.2}$$

where z_0 is the roughness length, which is the height at which the mean wind speed becomes zero. Over sea, the roughness length is commonly expressed using the Charnock's relation,

$$z_0 = \alpha_c \frac{u_*^2}{g}, \tag{4.3}$$

where $g = 9.81$ m/s^2 is the gravitational acceleration and α_c is the Charnock's parameter, $\alpha_c \approx 0.012$ (Charnock, 1955).

According to MOST, the influence of atmospheric stability over the wind speed gradient within the surface layer is expressed by the dimensionless wind shear, ϕ_m, as

$$\frac{\partial U}{\partial z} = \phi_m \frac{u_*}{\kappa z}. \tag{4.4}$$

The dimensionless wind shear takes different functional forms depending on the atmospheric stability conditions. It is usually described by the experiment-based Businger–Dyer functions (Businger et al., 1971; Dyer, 1974):

$$\phi_m = \begin{cases} 1 + \beta \frac{z}{L}, & \text{for} \frac{z}{L} > 0 \text{ (stable)} \\ 1, & \text{for} \frac{z}{L} = 0 \text{ (neutral)} \\ \left(1 - \gamma \frac{z}{L}\right)^{-\frac{1}{4}}, & \text{for} \frac{z}{L} < 0 \text{ (unstable)} \end{cases}, \tag{4.5}$$

where L is the Obukhov length, $\frac{z}{L}$ is the dimensionless stability parameter, and $\beta = 6.0$ and $\gamma = 19.3$ are empirical constants (Högström, 1988), later validated by Holtslag et al. (2015) for the IJmuiden site.

Thus, under non-neutral conditions the diabatic wind profile can be expressed as

$$U(z) = \frac{u_*}{\kappa}\left[\ln\left(\frac{z}{z_0}\right) - \Psi_m\left(\frac{z}{L}\right)\right], \tag{4.6}$$

where $\Psi_m\left(\frac{z}{L}\right)$ is the stability correction function (Stull, 1988; Barthelmie, 1999)

$$\Psi_m\left(\frac{z}{L}\right) = \begin{cases} -\beta\frac{z}{L} & \frac{z}{L} > 0 \text{ (stable)} \\ 0 & \frac{z}{L} = 0 \text{ (neutral)} \\ 2\ln(\frac{1+x}{2}) + \ln(\frac{1+x^2}{2}) - 2\arctan(x) + \frac{\pi}{2} & \frac{z}{L} < 0 \text{ (unstable)} \end{cases}, \tag{4.7}$$

where $x = \left[1 - \frac{\gamma z}{L}\right]^{1/4}$. Although the Businger–Dyer functions were empirically derived from data collected over land, their applicability has been successfully tested and validated for the estimation of the offshore wind profile (Holtslag et al., 2015; Lange et al., 2004).

The Obukhov length can be used to classify atmospheric stability conditions, classified into stable ($L > 0$), neutral ($L \to \pm\infty$), or unstable ($L < 0$). With a view to Section 4.4 two atmospheric stability classifications are listed in Tables 4.1 and 4.2 according to the definition classes for L of Van Wijk et al. (1990) and Gryning et al. (2007).

The behavior of the stability correction $\Psi_m\left(\frac{z}{L}\right)$ as a function of the Obukhov length L is depicted in Figure 4.1.

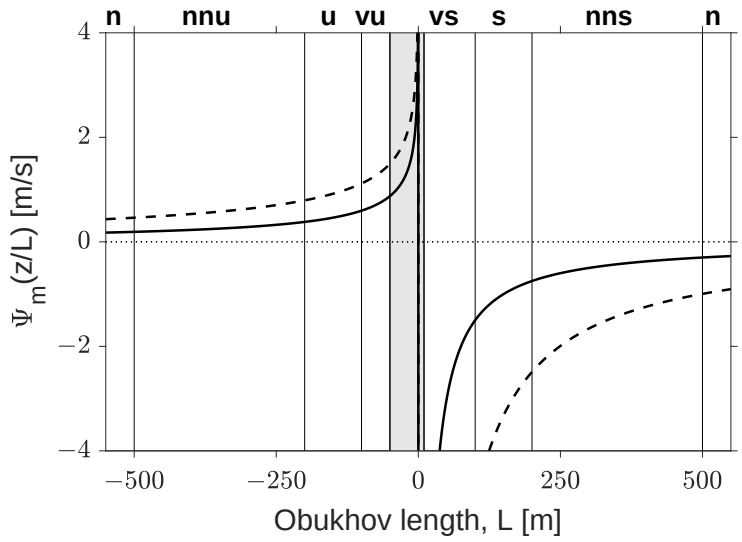

Figure 4.1: Stability correction function $\Psi_m(\frac{z}{L})$ as a function of Obukhov's length for $z = 25$ m (thick solid line) and $z = 83$ m (dashed line). The vertical grey shaded area delimits the interval from $L = -50$ to $L = 10$ m. Vertical lines delimit Gryning et al. (2007) stability classification thresholds per Table 4.2. Labels: vu, very unstable; u, unstable; nnu, near-neutral unstable; n, neutral; nns, near-neutral stable; s, stable; and vs, very stable.

Table 4.1: Van Wijk et al.'s stability classes based on the Obukhov length, L. Adapted from (Van Wijk et al., 1990).

Atmospheric Stability	**Obukhov Length Range (m)**
Very Stable—vs	$0 < L \leq 200$
Stable—s	$200 < L < 1000$
Neutral—n	$\|L\| \geq 1000$
Unstable—u	$-1000 < L < -200$
Very Unstable—vu	$-200 \leq L < 0$

Table 4.2: Gryning et al.'s stability classes based on the Obukhov length, L. Adapted from (Gryning et al., 2007).

Atmospheric Stability	**Obukhov Length Range (m)**
Very Stable—vs	$10 \leq L < 50$
Stable—s	$50 \leq L < 200$
Near-Neutral Stable—nns	$200 \leq L < 500$
Neutral—n	$\|L\| \geq 500$
Near-Neutral Unstable—nnu	$-500 < L \leq -200$
Unstable—u	$-200 < L \leq -100$
Very Unstable—vu	$-100 < L \leq -50$

Finally, we introduce the wind-speed ratio between HWSs at two heights, z_1

and z_2, $z_2 > z_1$, is therefore,

$$WSR(z_1, z_2, L) = \frac{U(z_2)}{U(z_1)} = \frac{\ln\left(\frac{z_2}{z_0}\right) - \Psi_m\left(\frac{z_2}{L}\right)}{\ln\left(\frac{z_1}{z_0}\right) - \Psi_m\left(\frac{z_1}{L}\right)}. \tag{4.8}$$

The wind-speed ratio is a proxy of wind shear that will be used to analyze the dependence of wind shear on the dimensionless stability, $\frac{z}{L}$, further.

4.3.3 Parametric wind model estimation

We estimate atmospheric stability based on FDWL HWS profiles measured at a discrete number of heights. We propose solving Equations (4.6) and (4.7) for model variables L, u^*, and z_0. The algorithm's sensitivity to these three variables and consequent dimensionality reduction of the problem (two-variable problem, L and u^*) is provided in Section 4.4.2.

The optimization problem can be formulated as

$$(L\,, u_*\,, z_0) = \underset{L,u_*,z_0}{argmin} ||\vec{U}_{FDWL} - \vec{U}(z, L\,, u_*\,, z_0)||^2, \tag{4.9}$$

where the function $\vec{U}(z, L\,, u_*\,, z_0)$ is the parametric wind profile model formulated by Equation (4.6) and piece-wise by Equation (4.7). Below, functions are assimilated into vectors and treated indistinctly. A constrained nonlinear least squares (NLSQ) method is used to solve the model parameters, L, u^*, and z_0, minimizing the error norm between the model vector, $\vec{U}(z)$, and the FDWL-measurement vector, $\vec{U}_{FDWL}$.

The diabatic correction function $\Psi_m(\frac{z}{L})$ (Equation (4.7), Figure 4.1) becomes ill-posed for Obukhov lengths close to zero ($L = 0$) and exhibits a nearly flat behavior for large values of the Obukhov length ($|L| \to \infty$). Additionally, $\Psi_m(\frac{z}{L})$ is a piece-wise function. To facilitate NLSQ convergence, we define upper and lower search bounds for each of the parameters to be optimized as

- $L \in [-2000, -1] \cup [1, 2000]$ m,
- $u_* \in [0, 1.4]$ m/s, and
- $z_0 \in [10^{-5}, 10^{-2}]$ m.

The limiting bounds for the roughness length z_0 in offshore environments follow (Golbazi & Archer, 2019; Stull, 1988). The friction velocity bounds are in agreement with those found in different experimental campaigns in the literature (Emeis

& Türk, 2009; Vickers et al., 2015) and represent roughly a factor 1.5 over the range of practical friction velocities retrieved by the sonic anemometers (Section 4.3.5, Equation (4.14)). The search bounds for the Obukhov length, L, are, e.g., a factor two and four over the practical neutral stability thresholds given by Van Wijk et al. (1990) (Table 4.1) and Gryning et al. (2007) (Table 4.2), respectively. Larger values do not tend to substantially improve the algorithm search performance (see Section 4.4.2).

Optimization starting vector. Two start points, one positive, $L^+ \in [1, 2000]$, and one negative, $L^- \in [-2000, -1]$, are set to $L^+ = 500$ m and $L^- = -500$ m, respectively, as initial guesses for the Obukhov length. This allows us to avoid the asymptotic discontinuity of $\Psi_m(\frac{z}{L})$ at $L = 0$ (Figure 4.1). The initial guesses for the friction velocity, u_*, and roughness length, z_0, are set to 0.7 m/s and 5×10^{-3} m, respectively, which are the mean values of these variables in the above search ranges. From these two starting vectors, (L^+, u_*, z_0) and (L^-, u_*, z_0), a positive and a negative search is started by the NLSQ algorithm and two candidate solution vectors are obtained. The vector with the smallest error norm is chosen as the solution.

4.3.4 Reference measurements: atmospheric stability

Reference metmast-derived Obukhov length and friction velocity are needed in order to assess the performance of the proposed algorithm in Section 4.3.3 above. In the present and following subsection (Section 4.3.5), different methods to estimate such reference parameters are presented.

Conventionally, the Obukhov length is directly computed from turbulence fluxes measured (from wind and temperature observations at similar heights), e.g., with a sonic anemometer (Stull, 1988). However, the sonic anemometer at 85 m available only recorded velocity observations. Alternatively, the method by Grachev & Fairall (1997) to estimate the Obukhov length, L, provides a way out when air and sea temperature observations are available, as is the case. They found empirical dependency between the bulk-Richardson number, Ri, and the dimensionless stability parameter. Their method has been used in recent studies (Holtslag et al., 2015; Borvarán et al., 2021).

The bulk Richardson number is an approximation of the gradient Richardson number in which actual local gradients in an atmospheric layer are approximately computed by measurements at a couple (or a series of) discrete heights. The bulk

Richardson number is defined as (Stull, 1988)

$$Ri = \frac{g\Delta\overline{\theta}_v \Delta z}{\overline{\theta}_v U^2}, z \in [z_{bottom}, z_{top}], \tag{4.10}$$

where $\Delta\overline{\theta}_v = \overline{\theta}_v(z_{top}) - \overline{\theta}_v(z_{bottom})$ is the difference between the mean virtual potential temperature at the top layer height, z_{top}, and bottom layer height, z_{bottom} and $\Delta z = z_{top} - z_{bottom}$. Here, $z_{top} = 21$ m above LAT and $z_{bottom} = 0$ m above LAT. $\overline{\theta}_v$ is the mean potential temperature in the layer and U is the mean wind observed at z_{top} (at this point we note that U is formally defined as $\Delta U = U(z_{top}) - U(z_{bottom}) = U(z_{top})$ on account of the fact that $U(z_{bottom}) = 0$). In practice, U is the 10 min averaged wind observed at 27 m.

The potential temperature is estimated from the expression (Stull, 1988; Wallace & Hobbs, 2006a)

$$\theta_v(z) = T(z)\left[\frac{P_0}{P(z)}\right]^{R/C_p}[1 + 0.61r(z)], \tag{4.11}$$

where T (K) is the temperature, $P_0 = 1000$ hPa is the reference pressure, P is the air pressure, $R \approx 287$ J/(K·kg) is the gas constant of air, $C_p \approx 1004$ J/(K·kg) is the specific heat capacity at a constant pressure for air, and r is the mixing ratio (unsaturated air).

In this study, we computed the mean potential temperature $\overline{\theta}_v$ at 21 m from the mast temperature, pressure, and humidity data at 21 m. $\overline{\theta}_v$ at sea-level was computed from the wave-buoy-measured 60 min mean water temperature (MacIsaac & Naeth, 2013), which was interpolated down to 10 min resolution, according to wind-energy standards (Peña et al., 2013). The pressure and relative humidity at sea level were calculated by extrapolating the mast pressure and humidity vertical profiles from the sensors at 21 m and 90 m (Figure 2.11) down to 0 m. Pressure and relative humidity at 0 m as well as water-temperature at 10 min resolution were computed via shape-preserving piecewise cubic interpolation (Fritsch & Carlson, 1980; Kahaner et al., 1989).

Subsequent to the calculation of Ri, the dimensionless stability parameter $\zeta = z/L$ is computed as

$$\zeta = \begin{cases} 10Ri & Ri \geq 0 \\ \frac{10Ri}{1-5Ri} & 0 < Ri < 0.2 \end{cases}. \tag{4.12}$$

The constants 10 and 5 above are empirical values (Grachev & Fairall, 1997). The latter implies a critical stable Ri of 0.2 so the theory has a limitation when the

conditions are very stable. Besides, when using the bulk Richarson number approximation, the thicker the layer, the more likely to smooth out large gradients in the layer and, therefore, to misestimate the occurrence of turbulence (Stull, 1988).

When we derive L from Equation (4.12) we refer to it as L_{Ri},

$$L_{Ri}(z') = \frac{z'}{\zeta}, \tag{4.13}$$

where z' is a reference height ensuring the validity of the bulk Richardson model (Equation (4.10)) above in the layer $[z_{bottom}, z_{top}]$. In the standard methodology (Grachev & Fairall, 1997), z' is taken as the sonic-anemometer observational height (11 m). However, in the case of IJmuiden, temperature and particularly the wind-speed observational heights are relatively high, 21 and 27 m, respectively. Although a rough estimation of the reference height can simply be taken as the mean height between the air observational height and sea level (Holtslag et al., 2015), in this case, $z' \approx (z_{top} + z_{bottom})/2 = 10.5$ m, accurate estimation of the reference height is more involved.

In order to estimate the most accurate meaningful reference height, z', the following procedure was carried out: different estimations of $L_{Ri}(z')$ were retrieved from
Equation (4.13) by varying z' from the layer top observational height ($z_{top} = 21$ m) to the rough reference height (10.5 m) in steps of 0.5 m, i.e., $z' = 21, 20.5, \ldots, 10.5$ m. As a result, we obtained 22 different sets of $L_{Ri}(z')$ values, each one corresponding to a z'. Next, the MOST model wind-speed ratio of Equation (4.8) was computed for all sets of the $L_{Ri}(z')$ as well as the coefficient of determination, ρ^2, between the measured and modeled wind-speed ratios. The z' (equivalently, $L_{Ri}(z')$) with the highest ρ^2 yielded the sought-after reference height. Thereby, $z' = 15.5$ m was found to be the reference height ensuring the highest ρ^2 after the outlier screenings applied over $L_{Ri}(z')$ and the measured wind-speed ratio (see the outlier screening and the results in Section 4.4.3).

4.3.5 Reference measurements: friction velocity

The friction velocity is a form by which a shear stress may be rewritten in units of velocity such as the velocity that relates wind shear between layers of flow, e.g., for neutral condition $u_* = \kappa\ (U(z_2) - U(z_1))/ln(z_2/z_1)$ (Equation (4.2)). Two reference methods are considered for comparison:

The first solves Equation (4.6) for u_* given the Obukhov length L_{Ri} estimated from the bulk Richardson number using Equation (4.13) and mast HWS measurements at 27 m. The roughness length z_0 is computed from Equation (4.3). This method can be viewed as "mast" 1D ($u_{*_{1-D}}$).

The second uses directly the measured turbulent fluxes (Stull, 1988),

$$u_{*_{sonic}} = \left(\overline{u'w'}^2 + \overline{v'w'}^2\right)^{0.25}. \tag{4.14}$$

For these computations, we used the sonic measurements at 85 m.

4.3.6 Data screening

To begin with, FDWL, mast-sensors and mast-DWL data were averaged to a common uniform time resolution of 10 min, which is according to WE standards (Peña et al., 2013). Accordingly, the wave-buoy-derived water temperature was resampled from 60 to 10 min as already mentioned in Section 4.3.4.

Regarding anemometers' data, the screening procedure relied on selection of the true wind direction (TWD) (Werkhoven & Verhoef, 2012). To do this, WD and HWS measurements from all the three anemometers at each of the three metmast measurement heights (27, 58.5 and 85 m) were checked. Figure 4.2 sketches a top-view of mast depicting the positions of the wind vanes and anemometers at each height. First, the middle WD (MWD) was computed as the median of the WD measurements by the three anemometers. Then, the TWD was derived following these criteria (see Figure 4.2a):

- If the MWD lay on the red crown, the TWD was computed as the mean WD between vanes HxxB240 and HxxB120,
- If (...) on the blue crown, (...) between vanes HxxB0 and HxxB120, and
- If (...) on the green crown, (...) between vanes HxxB240 and HxxB0.

Finally, the true wind speed was chosen as the one retrieved from the anemometer over which the TWD was within a confidence angle range (the wake-free range) of $90° \pm 30°$ (Figure 4.2b) in relation its boom orientation.

Concerning the lidar instruments, HWS measurements lower than 2 m/s or higher than 100 m/s were rejected on account of the ZephIR-300 manufacturer's specifications (Campbell Scientific, 2016). Regarding the FDWL, it is well-known that motion-induced effects on the retrieved wind vector become prominent at

a 1-s temporal resolution but are negligible at the 10 min level. For the latter case, motion effects increase fluctuations on the wind speed (Gutiérrez-Antuñano et al., 2018; Salcedo-Bosch et al., 2020, 2021c). At the 10 min level, it was shown (Gutiérrez-Antuñano et al., 2017; Arranz, 2011) that the spatial variation (SV) parameter (see below) can be used as a threshold to filter data as it represents a trade-off between key performance indicator (KPI) improvements and data availability.

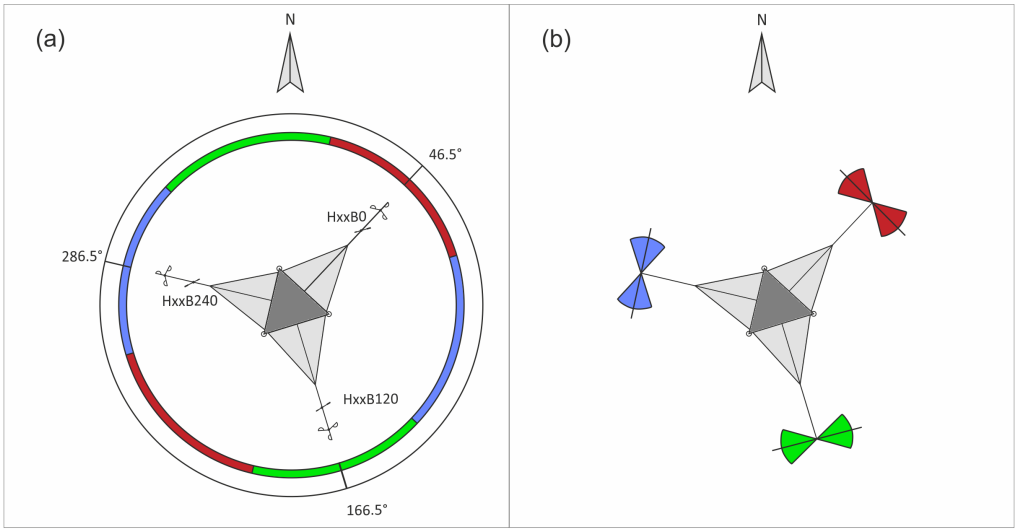

Figure 4.2: Top view of the mast at IJmuiden. (**a**) Wind vanes and anemometers on each boom (B0, B120, and B240) at the three measurement heights, Hxx (xx = 27, 58.5 and 85 m). Angles indicate boom orientation. (Red, green, and blue) Color-coded circular crown sectors represent the wake-free angle ranges for each anemometer ($90° \pm 30°$, panel (**b**)) in relation to boom orientation. Adapted from (Werkhoven & Verhoef, 2012).

FDWL measurement outliers were identified by plotting the HWS differences between the metmast and FDWL measurements as a function of different FDWL internal parameters, namely, the backscatter, bearing (compass), points in fit out of the 50 radial velocities within a full scan (see below), SV, precipitation, and visibility. For each internal parameter, we considered as outliers the samples which yielded differences higher than 2 m/s in relation to metmast reference. The same analysis was conducted with the mast-DWL, which served as the reference lidar.

Backscatter refers to the intensity of the Doppler lidar echo. Bearing refers to the lidar pointing direction with respect to the Earth's magnetic North. Points in fit and SV are parameters related to the Velocity Azimuth Display (VAD) algorithm used by the lidar to retrieve the wind vector under the assumption of uniform

wind. The SV is an indicator of the goodness of the VAD fitting of the radial velocities within the lidar scanning circle used to retrieve the wind vector at a given height. Therefore, the SV can be understood as a turbulence parameter describing the variation degree of the radial wind speeds within the scan (Wagner et al., 2009). High SV values are associated to measurements for which the hypothesis of uniform wind during the lidar scan is no longer valid (Salcedo-Bosch et al., 2021c). This leads to outlier measurements, which must be removed.

Numerical analysis showed that the largest differences in HWS between the mast anemometer and FDWL measurements were attributable to bearing and SV of the FDWL. Therefore, we applied the following outlier rejection criteria:

- (i) HWS < 2 m/s or HWS > 70 m/s,
- (ii) bearing = $0°$ (FDWL compass issue, see Section 4.4.1), and
- (iii) 95th percentile spatial-variation threshold.

4.4 Results and discussion

4.4.1 Data screening and quality assurance

Now, we discuss our results for outlier criteria (ii) and (iii) which were introduced in Section 4.3.6 above. Figure 4.3a shows the HWS difference between the cup anemometer and the FDWL measurements at 83 m as a function of the FWDL bearing. Similar results were found for the two other FDWL heights, 25 and 56 m (not shown). Figure 4.3b shows a similar plot but for the mast-DWL. As expected, the FWDL bearing covers the full range of motion, whereas the mast-DWL bearing remains mostly fixed at $\approx 3°$. The largest HWS differences occur for bearings equal to zero, which lacks physical consistency and might show an issue in the data acquisition system.

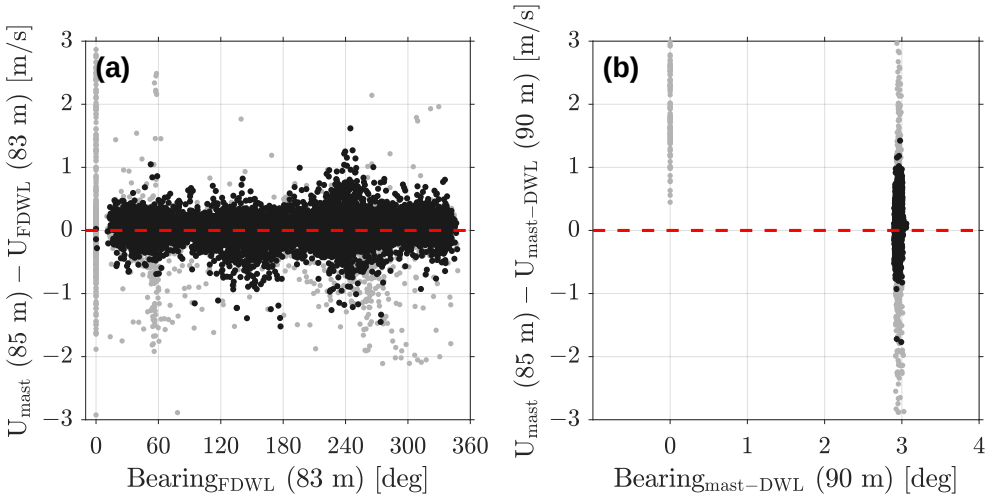

Figure 4.3: Lidar data screening: bearing. (**a**) HWS differences between the cup anemometer and the FDWL measurements as a function of FDWL bearing at a 83 m height. (**b**) Same as in panel (**a**) but compared to the fixed DWL on the mast. Black and grey dots indicate valid and outlier samples, respectively (Section 4.3.6). Dashed red line indicates the zero-bias baseline.

Figure 4.4 shows the histogram of SV from the FDWL at 25 m and the HWS differences as a function of the SV between the 27-m cup anemometers and the FDWL, respectively. In Figure 4.4a, the border line between the white and grey shades delimits the 95th percentile of the one-tailed spatial-variation distribution. This percentile corresponds to a SV threshold, SV$= 0.055$ and SV$\approx 0.055 - 0.065$ for the other measurement heights of the lidar (data not show). For the mast-DWL, the 95th percentile corresponds to the threshold SV≈ 0.07 (data not shown). The SV thresholds used here for 10 min data were found to be more conservative than those used in previous studies (SV≈ 0.1) (Gutiérrez-Antuñano et al., 2017; Arranz, 2011), in which the FDWL measurements were compared against metmast values for quality assurance (QA).

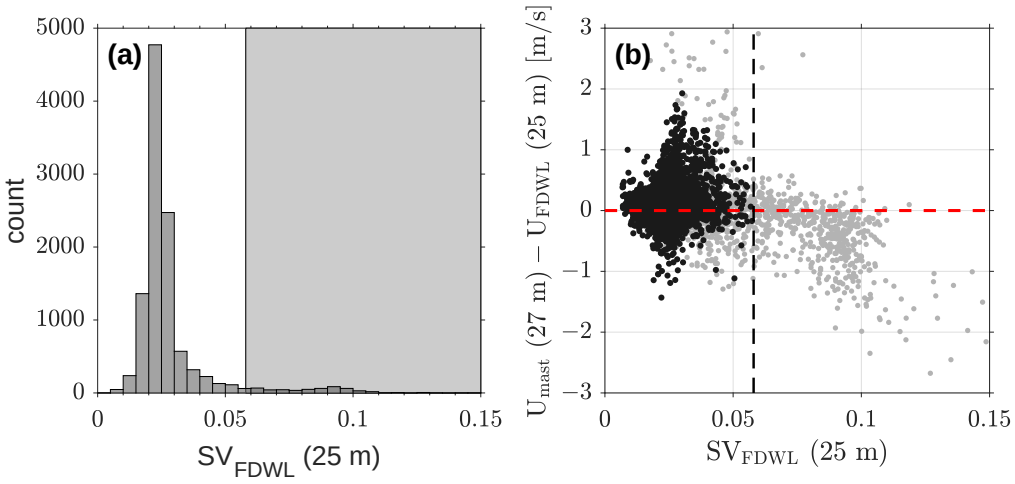

Figure 4.4: Lidar data screening: spatial variation. (**a**) SV histogram for the FDWL at a 25 m height (refer to Figure 2.11). Grey shading indicates the upper tail of the 5% area corresponding to the rejected outliers in the SV distribution (95th to-100th percentiles). (**b**) Same format as in Figure 4.3 but using SV as the dependent variable. The dashed vertical line indicates the 95th percentile of the SV threshold.

The appropriateness of the SV filtering criterion is re-encountered in Figure 4.4b, which shows that HWS differences between the FDWL and the metmast measurements started to deviate from the ideal 0-m/s bias (dashed red line) for SVs above approximately 0.05, which justifies our choice for criterion (iii) in Section 4.3.6.

Regarding the anemometers, Figure 4.5 shows the HWS differences between the cup anemometers and the lidars as a function of direction. The reduction on the scattering of data after application of the TWD screening criterion is well noticed (black versus grey dots). Quantitatively, after outlier rejection, peak HWS differences were below ± 1 m/s at all heights, which shows that the mast effects were effectively removed.

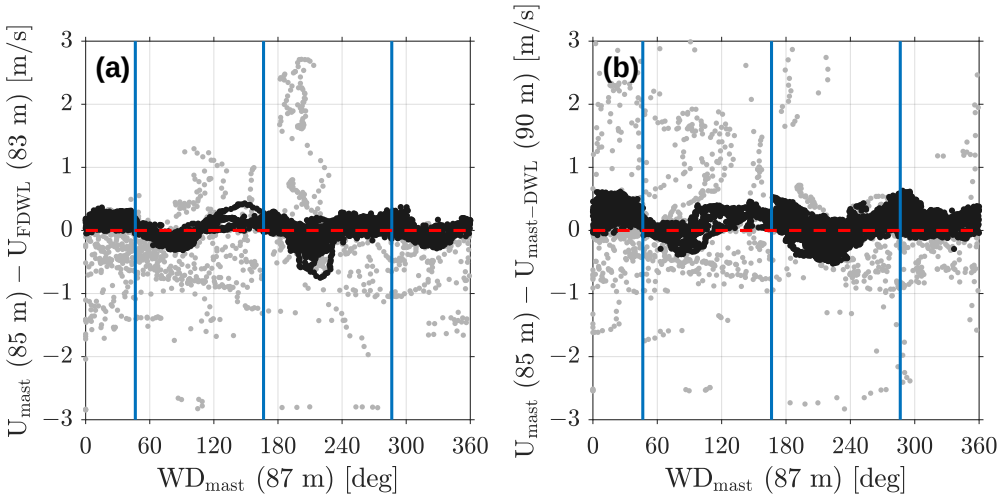

Figure 4.5: Anemometer data screening: WD. (**a**) HWS differences between the cup anemometer and the FDWL measurements as a function of wind direction at a 87 m height. (**b**) Same as in panel (**a**) but compared to the DWL on the mast. Vertical blue lines indicate the directions of the mast booms (46.5°, 166.5°, and 286.5°, Figure 4.2).

The 82-day IJmuiden campaign produced a dataset with 10,833 10 min samples. After the filtering procedure described in Section 4.3.6, we obtained 8263 10 min samples. Figure 4.6 shows that both the cup anemometers and the fixed and floating lidars measured very closed HWSs with determination coefficients higher than $\rho^2 = 0.996$ and slopes of the regression lines between 0.985 and 1.010 at all measurement heights, as expected from previous studies (Gutiérrez et al., 2015; Gutierrez-Antunano et al., 2017; Schuon et al., 2012; Mathisen, 2013; Gutiérrez-Antuñano et al., 2018). These values are within the KPIs defined by the Carbon Trust's Offshore Wind Accelerator (OWA) (Carbon Trust, 2018).

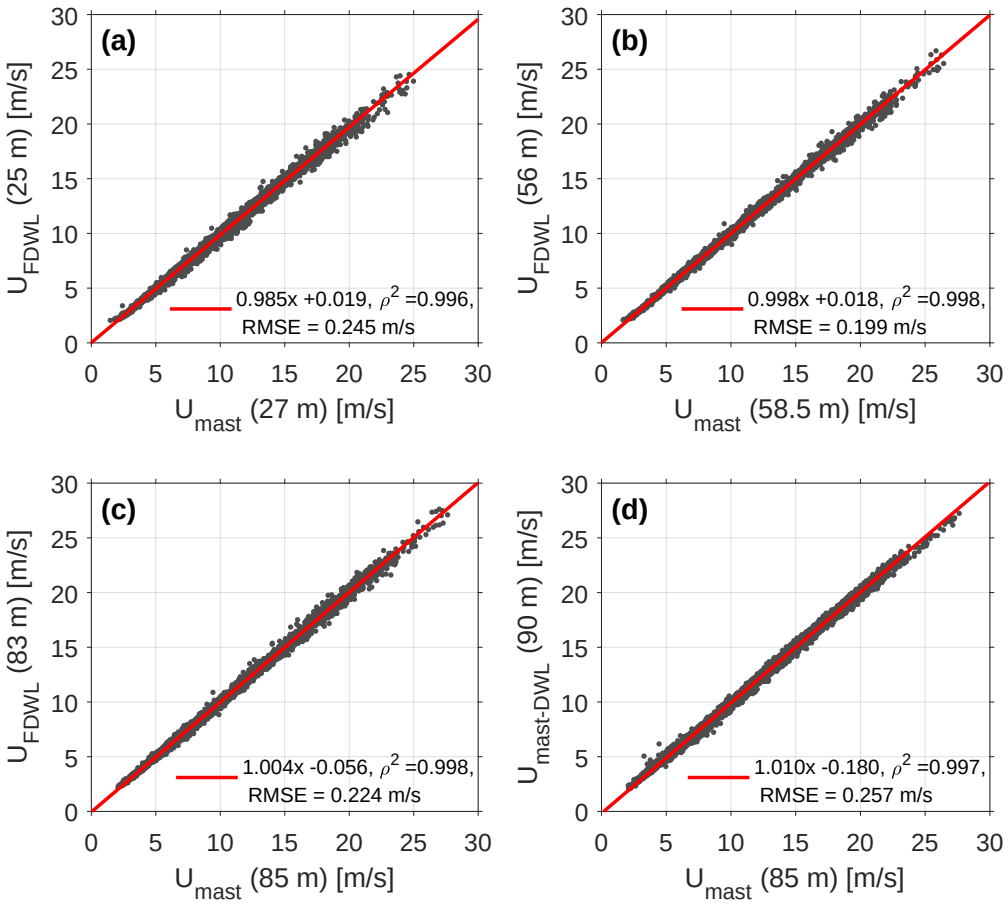

Figure 4.6: Quality assurance. (**a**–**c**) Comparison between FDWL HWS (denoted U_{FDWL}) and cup anemometer HWS (U_{mast}) at the at different heights (see labels). (**d**) Same as (**a**) but for the DWL on the mast at 90 m. The red line indicates the regression line. ρ^2 is the coefficient of determination.

4.4.2 Sensitivity to the wind model parameters

In order to analyze the sensitivity of the parametric wind model presented in Section 4.3.2 with respect to Equation (4.9) model parameters, a sensitivity simulator was implemented (Figure 4.7). The simulator inputs are the model parameters Obukhov length L, friction velocity u_*, and roughness length z_0, denoted as L^0, u_*^0, and z_0^0, respectively. These inputs were perturbed by an intensity factor $\pm P\%(\pm 10\%)$. Then, the perturbed inputs were used to compute the non-neutral wind correction $\Psi_m\left(\frac{z}{L}\right)$ using Equation (4.7). Finally, the perturbed wind profile, $U(z) + \Delta U(z)$, was simulated as a function of the perturbation intensity on the input variables through Equation (4.6). Five different atmospheric stability scenarios were considered: very unstable, unstable, neutral, stable, and very stable, based on

Obukhov length values denoted by L^0_{vu}, L^0_u, L^0_n, L^0_s, and L^0_{vs}, respectively.

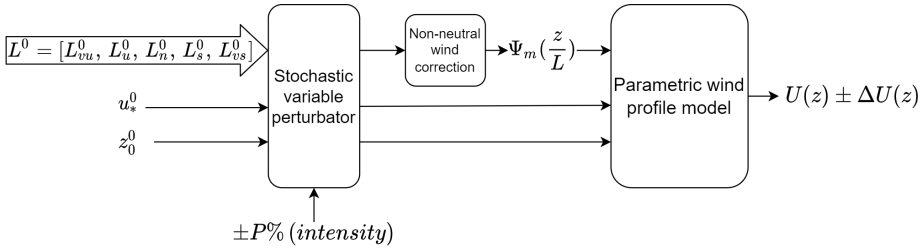

Figure 4.7: Sensitivity simulator block diagram. L^0, u^0_*, and z^0_0 denote the nominal values for L, u_* ,and z_0, respectively. Subscripts vu, u, n, s, and vs stand for very unstable, unstable, neutral, stable, and very stable atmospheric stability conditions, respectively. The non-neutral wind correction block implements Equation (4.7) and the parametric wind profile model block refers to Equation (4.6).

The error propagated on the model wind profile was found to be insensitive to perturbations in the roughness length z_0. Therefore, practical implementation of the algorithm embeds Equation (4.3) into Equation (4.6) as

$$U(z) = \frac{u_*}{\kappa}\left[\ln\left(\frac{z}{\alpha_c \frac{u_*^2}{g}}\right) - \Psi_m\left(\frac{z}{L}\right)\right]. \tag{4.15}$$

Thus, the model dimension reduces from three (L, u_*, and z_0) to two (L and u_*), hereafter called the 2D algorithm. Likewise, slight deviations in the Charnock's constant (Equation 4.3) have low impact on the retrieved wind model parameters (L and u_*). Furthermore, as expected from correction function $\Psi_m(\frac{z}{L})$ (Figure 4.1), the sensitivity of the model wind profile with respect to the Obukhov length was found to be proportional to $1/|L|$. Further discussion is given in Section 4.4.4, in line with the statistical results encountered.

4.4.3 Wind shear dependence on dimensionless stability

The dependence of the wind speed ratio (Equation (4.8)) on the dimensionless stability computed from both the 2D Obukhov length ($\frac{z'}{\hat{L}}$) and from the Ri reference ($\frac{z'}{L_{Ri}}$) enabled us to quantify the performance of the 2D algorithm. The wind speed ratio was computed between the top and bottom measurement heights of both the FDWL (83 and 25 m) and the mast (85 and 27 m). As described in Section 4.3.4, $z' = 15.5$ m was taken as the reference height. We used 8,263 10 min clean data records (Section 4.3.6). Additionally, two successive levels of outlier filtering were

considered: (i) retrieved Obukhov lengths in the interval $(-50 < L_{Ri} < 10)$ m were rejected because these values were outside the stability limits in Table 4.2, and (ii) wind speed ratios were histogram-filtered. To achieve the latter, the dimensionless stability range was divided into 0.01-width bins and, in each bin, the wind-speed ratios outside of the $\mu \pm 1\sigma$ (with μ being the mean and σ being the standard deviation of the wind-speed ratio distribution in the bin) were rejected as outliers.

Figure 4.8a,b plots FDWL and metmast wind-speed ratios as a function of dimensionless stability parameter $\frac{z'}{\hat{L}}$, respectively. Figure 4.8c plots metmast wind-speed ratio as function of $\frac{z'}{L_{Ri}}$.

The FDWL wind-speed ratio as a function of $\frac{z'}{\hat{L}}$ (Figure 4.8a) yielded the best statistical indicators either if all or nonoutlier samples were considered ($\rho^2_{all} = 0.965$, $RMSE_{all} = 0.029$; $\rho^2_{1\sigma} = 0.988$, $RMSE_{1\sigma} = 0.016$, respectively). This was expected because the FDWL-derived HWSs were used to retrieve the estimated Obukhov length $\hat{L}$ using the 2D method, which, in turn, relies on the Businger–Dyer functions. Figure 4.8b provides tiebreaker proof confirming the successful performance of the 2D algorithm. Thus, in Figure 4.8b, the mast-derived wind speed ratios are compared to the estimated $\hat{L}$ values, and the statistical indicators found ($\rho^2_{1\sigma} = 0.974$ and $RMSE_{1\sigma} = 0.023$) are virtually coincident with those in Figure 4.8a. Additionally, when comparing the distribution of the points along the horizontal axes in Figure 4.8b,c ($\frac{z'}{\hat{L}}$ and $\frac{z'}{L_{Ri}}$, respectively), figures that share identical mast data, the spread along the $\frac{z'}{\hat{L}}$ axis (2D algorithm) is narrower than along the $\frac{z'}{L_{Ri}}$ (Richardson reference). Again, this confirms the superior performance of the 2D algorithm. Regarding Figure 4.8c, and despite the clear dependence obtained between the wind-speed ratio and dimensionless stability $\frac{z'}{L_{Ri}}$, the huge number of outliers suggests that not all measured wind profiles were acceptably modeled by the MOST model (Equation (4.6)).

In non-MOST situations, e.g., low-level jet and storm events, the estimates of the 2D-algorithm may be highly biased. The residual norm between the measured and fitted wind profiles has been used to quantitatively assess the 2D-algorithm accuracy. The residual norm is indicative of the quality of the fitting and is defined as the norm of the error between the parametric and the measured wind profiles. Most of the records showed residual norm values between 0 m/s and 2.21 m/s. Occurrences with a residual norm higher than the residual norm 95th percentile, corresponding to a value of 0.42 m/s, were filtered out (413 records). In the vast majority of cases, the 2D-algorithm is able to converge because most of experimental wind profiles measured by the FDWL are well predicted by MOST.

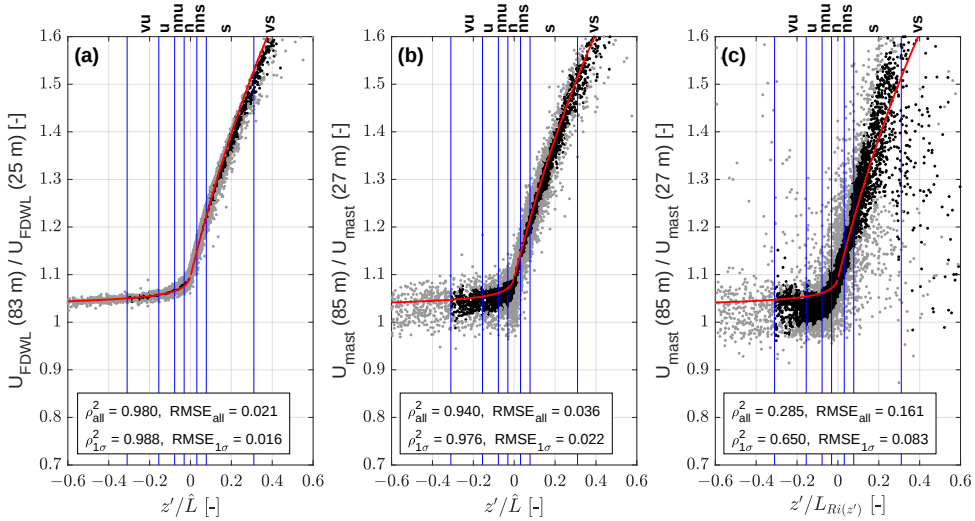

Figure 4.8: (**a**,**b**) The FDWL and mast wind-speed ratios as a function of $\frac{z'}{\hat{L}}$, respectively. (**c**) The mast wind-speed ratio plotted as a function of $\frac{z'}{L_{Ri}}$. Black and grey dots represent valid and outlier samples, respectively. $z' = 15.5$ m. ρ is the coefficient of determination. Subscripts "all" and "1σ" represent all samples and samples at $\mu \pm 1\sigma$ (see body text), respectively. Red line, wind-speed ratio reference model (Equations (4.8) and (4.7)). Blue lines, stability classification thresholds from Gryning et al. (2007) (see Table 4.2). vu, very unstable; u, unstable; nnu, near-neutral unstable; n, neutral, nns near-neutral stable; s, stable; and vs, very stable.

4.4.4 Performance statistics: friction velocity and stability

The performance of the 2D algorithm with regard to friction velocity u_* was assessed by comparing the velocity estimated using the 2D algorithm, $\hat{u}_*$ with the two reference velocities described in Section 4.3.5, namely, the reference $u_{*_{sonic}}$ computed by the sonic anemometer and the mast-derived $u_{*_{1-D}}$ computed by the 1D method (Figure 4.9).

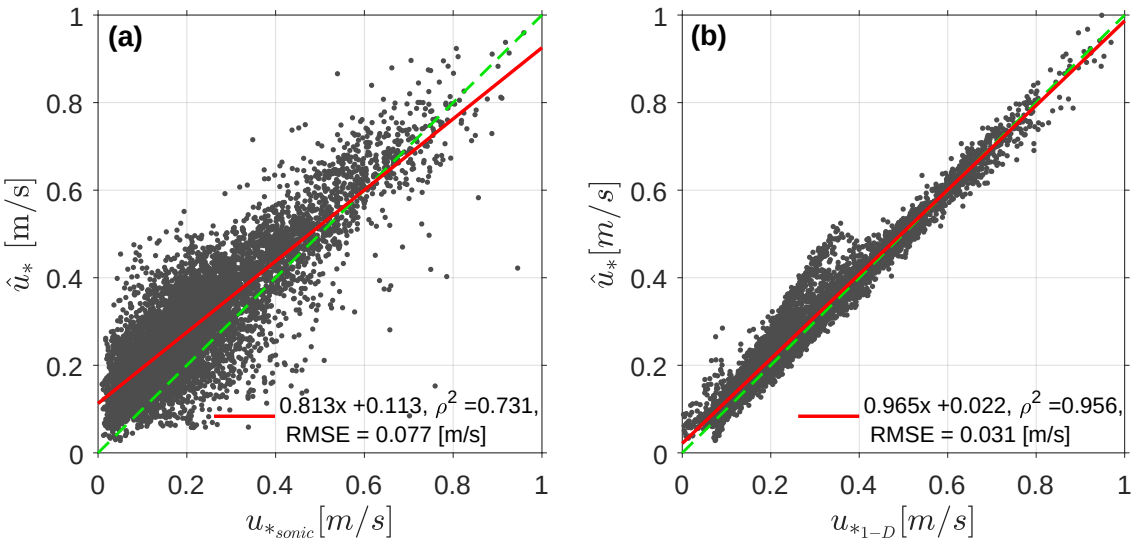

Figure 4.9: Scatter plot of the 2D-estimated friction velocity $\hat{u}_*$ against the two references provided in Section 4.3.5: (**a**) sonic anemometer reference velocity $u_{*_{sonic}}$, at 85 m; and (**b**) 1D method reference velocity u_{*1-D}. Green line is the reference 1:1 line.

Figure 4.9a shows that the points $(u_{*_{sonic}}, \hat{u}_*)$ were scattered widely. This was further corroborated by numerical analysis, which yielded a linear regression (LR) $\hat{u}_* = 0.813 \cdot u_{*_{sonic}} + 0.113$, coefficient of determination $\rho^2 = 0.731$, and $RMSE = 0.077$ m/s. These comparatively modest indicators are due to the fact that the sonic anemometer was located at a height of 85 m, which may well be beyond the surface layer. Above the surface layer, the proposed model is not valid, which leads to biased estimations (Stull, 1988). Worse results were attained when considering alternative values for Charnock's parameter, α_c, which is a site-dependent parameter here assumed as $\alpha_c = 0.012$ based on previous studies (Cheynet et al., 2017; Kelly, 2021; Peña & Gryning, 2008; Holtslag et al., 2015)

When comparing $\hat{u}_*$ against mast-derived $u_{*_{1-D}}$ (Figure 4.9b), a much better agreement is found. This is supported by a LR as good as $\hat{u}_* = 0.965 \cdot u_{*_{1-D}} + 0.022$, which is virtually the ideal 1:1 line; $\rho^2 = 0.956$; and $RMSE = 0.031$ m/s.

The performance of the 2D algorithm for the estimated Obukhov length, $\hat{L}$, was tested against the Richardson reference, L_{Ri}, for the whole campaign. For this task, two well-accepted stability classification criteria in the literature were considered: (i) Van Wijk's (Table 4.1), and (ii) Gryning's criteria (Table 4.2).

Van Wijk's classification. Figure 4.10 compares classification results among the Obukhov lengths estimated by the 2D algorithm, $\hat{L}$, and by the Ri estimate, L_{Ri}. The type criteria are provided in Table 4.1. Figure 4.10a,b shows similar but not

identical results. For example, the hourly evolution of the stable and neutral classes is nearly identical for both estimators. However, this is not the case for very unstable class, which was overestimated by the 2D algorithm to the detriment of the unstable class when compared to the Richardson reference. Similar results can be derived from Figure 4.10c,d. Thus, the 2D method yielded 33% of very unstable cases, whereas the Richardson reference yielded 25%.

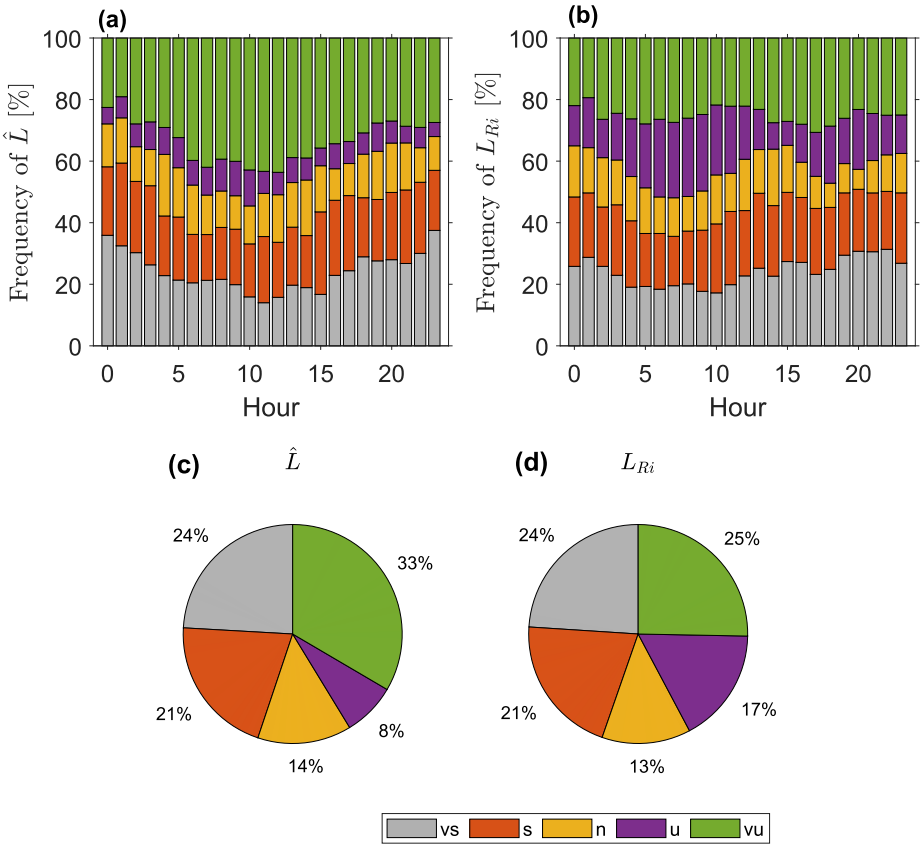

Figure 4.10: Overall campaign stability classification results (Van Wijk et al. (1990) criterion). (**a**,**b**) Stability histograms showing the relation between frequency of occurrence of each stability class clustered by hour of the day. (**c**,**d**) Corresponding stability pie charts showing the estimated Obukhov length, $\hat{L}$ (**c**), and the Richardson reference, L_{Ri} (**d**).

Gryning's classification. A similar analysis was conducted for the Gryning classification (Table 4.2). This criterion essentially breaks down the Van Wijk stability classes into subclasses in order to create room for the near-neutral stable and near-neutral unstable subclasses.

Figure 4.11 compares the classification results yielded by the 2D algorithm, $\hat{L}$,

and Ri estimate, L_{Ri}. Figure 4.11a,b shows similar temporal behavior for the very stable and stable classes over the course of the day. The latter class became prominent during the last hours of the day. In contrast, as occurred with the Van Wijk classification, the neutral class and all the unstable classes estimated by the 2D algorithm exhibited larger variations compared to the Richardson reference. When comparing $\hat{L}$ to L_{Ri} in the pie charts, 5% ($\hat{L}$ chart) vs. 3% (L_{Ri} chart) of the cases were classified as very unstable, 11% vs. 15% were classified as unstable or near-neutral unstable. In contrast, the following classes remained essentially the same: 31% ($\hat{L}$ panel) vs. 31% (L_{Ri} panel) for the neutral case, 19% vs. 19 % for the near-neutral stable case, 28% vs. 27% for the stable case, and 4% vs 4% for the very stable class.

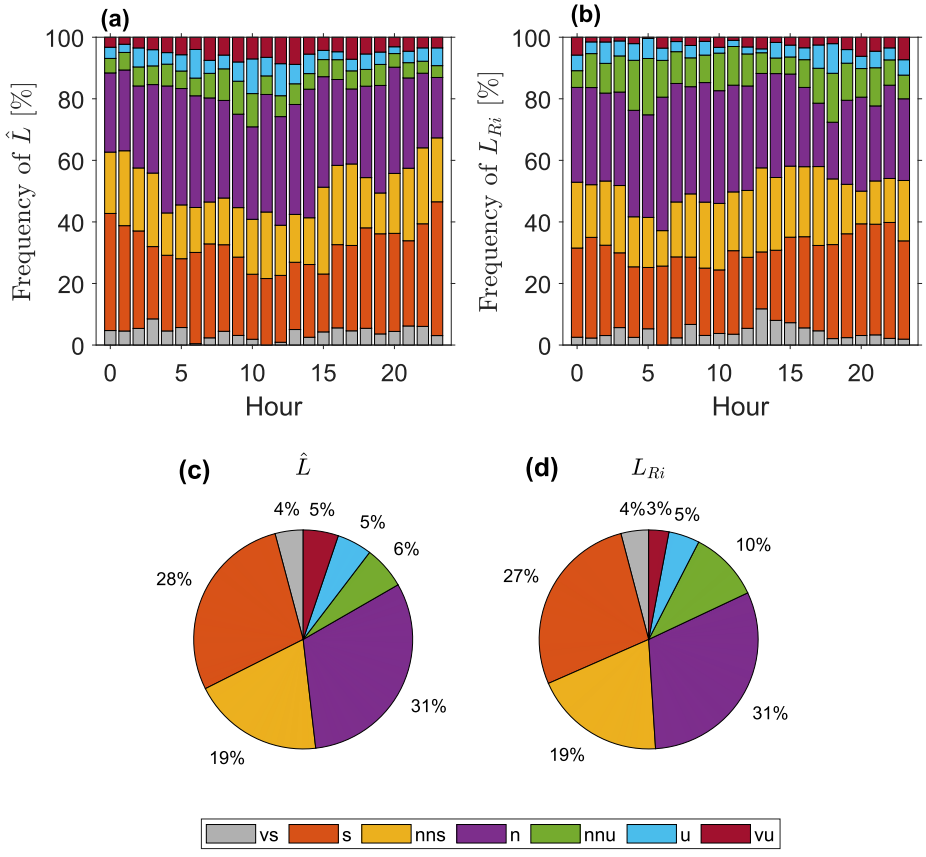

Figure 4.11: Overall campaign stability classification results (Gryning et al. (2007) criterion) using the same format as in Figure 4.10.

Next, we quantified classification performance by rating the one-to-one stability class correspondence between $\hat{L}$ and L_{Ri}. This one-to-one correspondence

is expressed via a confusion matrix, in which each matrix row represents the instances in an actual reference stability class (L_{Ri}), and each column represents the instances in an estimated stability class ($\hat{L}$). 4.12 depict the matrix obtained when considering the Gryning classification criterion. An ideal predictive method would have all instances along the main diagonal of the confusion matrix. Thus, bluish cells represent instances in which the estimated stability class matches the Richardson reference class, whereas reddish cells represent misclassifications. In order to quantitatively assess performance of the 2D algorithm, we define the hit rate (HR) as

$$HR[\%] = \frac{\text{no. of correct estimations}}{\text{no. of estimations}} \times 100. \tag{4.16}$$

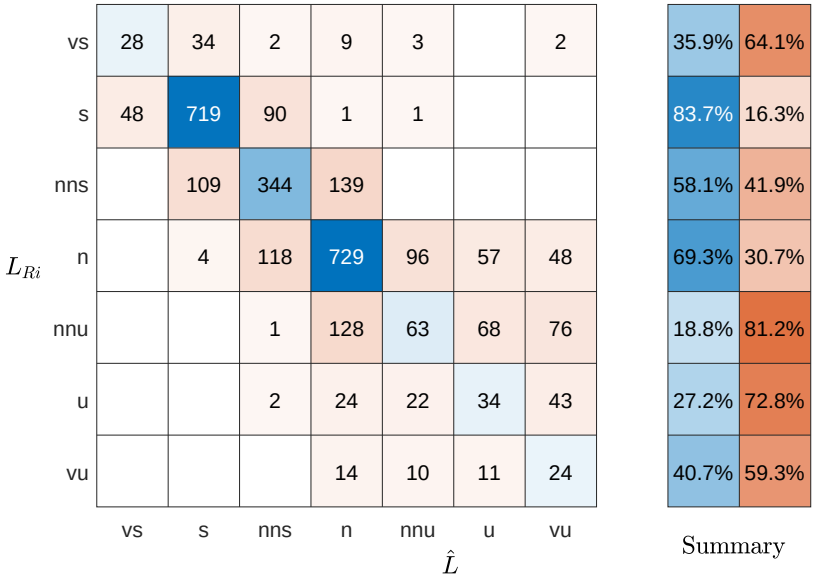

Figure 4.12: Confusion matrix between $\hat{L}$ and L_{Ri} for Gryning's stability classes (Table 4.1). The summary matrix on the right totals the HR (bluish) and miss rate (1-HR, reddish) for each stability class. vs, very stable; s, stable; nns, near-neutral stable; n, neutral; nnu, near-neutral unstable; u, unstable; vu, very unstable.

The miss rate is simply the complementary function $1-HR$. Figure 4.12 depicts the confusion matrix considering Gryning's stability classes (Table 4.2). We found that the estimated classes lay along a band formed by the main diagonal, the first diagonal below this, and the first diagonal above the main diagonal. Thus, an overall HR of 62.59% was obtained and the remaining 29.21% corresponded to the classes estimated by the 2D algorithm that were adjacent to the correct ones given by the Richardson reference. The summary matrix shows a very high miss

rate in unstable atmospheres with the HRs ranging from 18.8% to 40.7%. The low HRs attained for the nnu, u, and vu classes occurred due to the low sensitivity of the wind shear model in Equation (4.6) with respect to the Obukhov length for unstable atmospheres. This is re-encountered in Figure 4.13a, in which the median wind profiles and related 25th to 75th percentiles are plotted parameterized by stability condition. For the nnu, u, and vu classes, the percentile bars overlap (dark green, red, and magenta traces, respectively), which makes it impossible for the 2D algorithm to discern them.

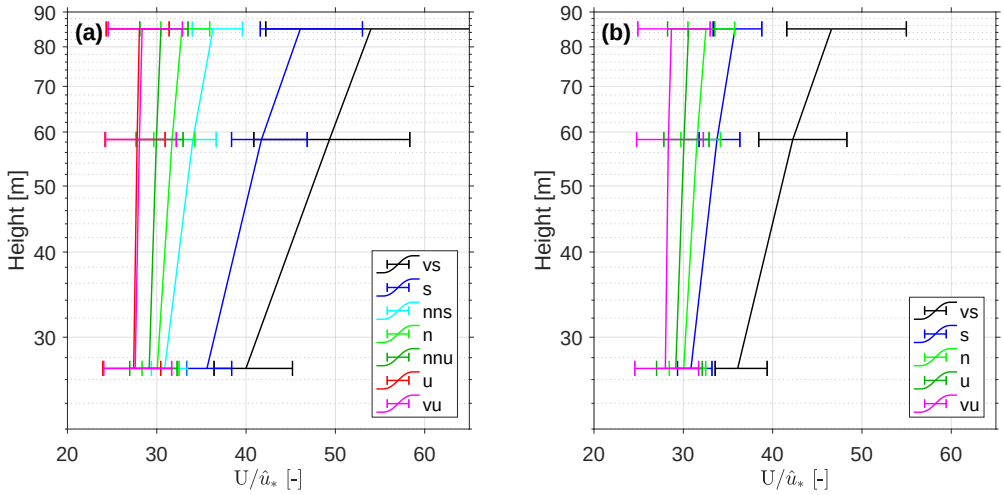

Figure 4.13: Median and percentiles of the u_*-normalized wind profiles measured by the metmast during IJmuiden campaign clustered by atmospheric stability classes. (**a**) Clusters by Gryning's classes. (**b**) Clusters by Van Wijk's classes. Error bars depict the 25th to 75th percentiles at each height.

In contrast, "s", "nns", and "n" classes scored HRs of 83.7%, 58.1%, and 69.3%, respectively, on account of their higher sensitivity, which, in turn, led to higher discernability among these classes. It is also worth noting the low HR (35.9%) achieved by the "vs" class. One reason accounting for that is the comparatively short span of Obukhov lengths included in the "vs" class ($10 \leq L < 50$) in Table 4.2. This was a too short span for the NSLQ solver to estimate the Obukhov length at such fine level of accuracy, which eventually led to miss-classification between the "vs" and "s" classes. This is also evidenced in Figure 4.13a by overlapping percentile bars for these classes.

Analogously to Figure 4.12, Figure 4.14 represents the confusion matrix considering the Van Wijk stability classes (Table 4.1). An overall HR of 66.07% and a misclassification rate of 33.93% were observed. The estimation performance varied

widely, ranging from HRs of 26.2% for the u class to 88.3% for the vs class. Again, the low HRs were due to the low sensitivity of the wind shear model with respect to the Obukhov length in unstable conditions, as evidenced in Figure 4.13b.

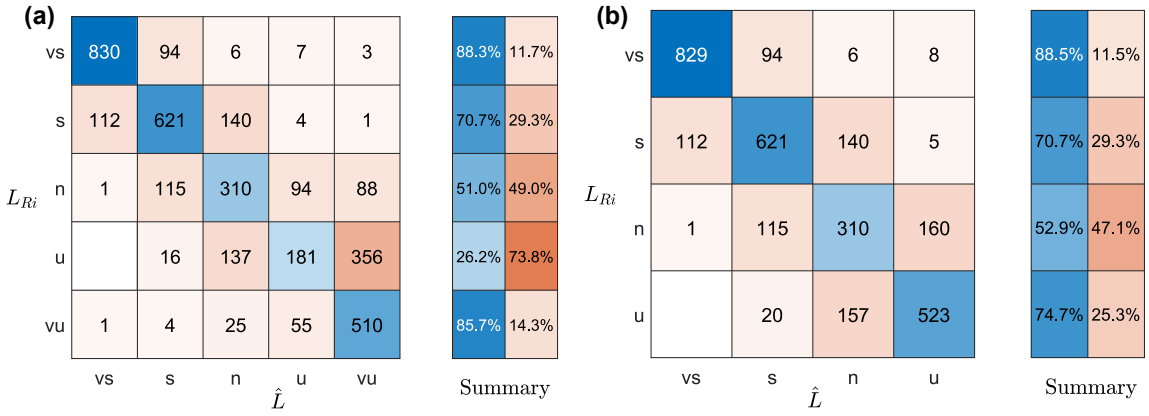

Figure 4.14: Confusion matrix between $\hat{L}$ and L_{Ri} for Van Wijk's stability classes (Table 4.1) in the same format as in Figure 4.12.

By comparing Figures 4.14 and 4.12 (equivalently, Figures 4.10 and 4.11) Van Wijk's classification criterion shows better performance than Gryning's. Although both have similar HRs (66.07% for Van Wijk and 62.59% for Gryning), the Van Wijk confusion matrix (Figure 4.14a) scores higher HRs than Gryning's in all but the u class, as indicated by the reddish cell in the summary matrix.

This, however, warrants some comments. For example, the good match between the estimated and reference stability classes in the pie chart in Figure 4.11 for the Gryning classification hides a population inversion between the right- and left-adjacent classes to the main diagonal (Figure 4.12). This also applies to Figure 4.14a.

Experiments also showed that wind profiles often became indistinctly misclassified into adjacent classes, as shown by the overlapping error bars in Figure 4.13. A method to mitigate this issue involves collapsing all unstable subclasses into an aggregated class named "unstable". Specifically, this aggregation leads to vs, s, n, and u classes in the Van Wijk classification (Figure 4.14b), and to vs, s, nns, n, and u classes in Gryning's classification (figure not shown). As a result, a much better agreement between the estimated and reference stability classes was achieved, as indicated by the higher HRs attained in all classes. Quantitatively, the overall HR increased to 73.6% for the Van Wijk classification. Similar results were achieved for the Gryning classification (figure not shown), which scored an HR of 72.6%.

It is important to mention that although we use L_{Ri} as the reference, it cannot be considered as the ground-truth reference for one-to-one comparison with $\hat{L}$, because it was not derived exactly as proposed by Grachev & Fairall (1997) due to the absence of turbulent fluxes measurements in the surface layer and the different instrumental measurement heights available. However, it is a good indicative of the method goodness in terms of atmospheric classification. In order to validate the method against a third party, the stability estimated by the 2D-algorithm was compared against the stability estimated by means of virtual potential temperature gradient ($d\theta_v/dz$) between 90 and 21 m. Virtual potential temperature was retrieved using temperature, pressure and relative humidity data from the IJmuiden mast via Equation (11). The potential temperature gradient indicator is only able to discern between two stability classes: unstable ($d\theta_v/dz < 0$) and stable ($d\theta_v/dz > 0$). Considering these categories, HRs higher than 82% were found for the comparison between $\hat{L}$ and $d\theta_v/dz$, further proving the goodness of the 2D algorithm.

4.5 Summary and conclusions

In this study, we suggested an 2D algorithm that accurately estimated both the Obukhov length and the friction velocity, hence, correctly determined atmospheric stability from FDWL measurements at four different heights. We used the spatial variation within the lidar scans as an important filtering parameter of the FDWL (Figure 4.4). The parameter is a proxy of turbulence; high spatial variation is associated to nonuniform wind during the scan. The latter can originate either from apparent turbulence (i.e., induced by sea motion) or from true wind turbulence (Gutiérrez-Antuñano et al., 2017). When comparing FDWL to mast-based wind speeds, we found that the mean winds were biased less than 1.5% (LR, $U_{FDWL} = 0.985 \cdot U_{mast} + 0.018$) with a determination coefficient, $\rho^2 = 0.996$, and a RMSE as low as 0.25 m/s. Similar values were found for the fixed DWL on the mast.

The algorithm assumes that the measured FDWL wind profiles follow MOST and the Charnock's relation is used to parameterize the roughness length. Over the sea, with such low roughness, the sensitivity of the roughness on the estimated parameters can be neglected. A parametric sensitivity study showed that unstable wind profiles exhibited lower sensitivity than stable wind profiles to variations of the Obukhov length (Figure 4.13).

The 2D-estimated Obukhov length and friction velocity were compared with reference to the mast-derived Obukhov length using the Richardson number, to the sonic-anemometer-derived friction velocity, and the 1D-model-derived friction velocity. Thus, the 2D-estimated friction velocity was largely in agreement with the sonic-anemometer-derived and the 1D-model-derived friction velocities, with coefficients of determination of 0.72 and 0.94, respectively (Figure 4.9).

We also examined the performance of the algorithm by classifying atmospheric stability in a number of classes. When comparing the relative frequencies of occurrence of each class of the Van Wijk classification, differences occurred between 0% and 10% (Figure 4.10) and between 0% and 4% for Gryning's classification (Figure 4.11). Notwithstanding these results, analysis through confusion matrices showed HRs of 65.24% for the Van Wijk and 62.63% for the Gryning classification. Higher HRs were attained for stable regimes than for unstable ones due to the lower sensitivity of the 2D algorithm to the Obukhov length in unstable regimes. This issue was addressed by collapsing the unstable sub-classes into a unique aggregated class named "unstable". For the Van Wijk's, this reclassification improved the HR up to 72.9% and up to 72.4% for the Gryning's. The confusion matrix study also showed that although simple pie chart statistics (Figure 4.11) indicate a very good one-to-one correspondence between the estimated stability class (through $\hat{L}$) and the Richardson reference class (through L_{Ri}), this correspondence is only apparent because cross-correspondences occur frequently between classes adjacent to the main diagonal (Figures 4.12 and 4.14). This effect became more prominent for classes falling in an Obukhov length interval in which Businger–Dyer's correction function had a flatter derivative (i.e., less gradient). Other misclassifications were attributable to anomalous profiles such as those associated with low-level jets. Moreover, the bulk Richardson number methodology used to compute the gradient Richardson number is just a two-point approximation of the derivative of the local wind and temperature gradients in the surface layer. Finally, the performance of the algorithm in terms of stability classification was compared against the virtual potential temperature gradient method acting as a proxy of stability. HRs higher than 82% were encountered, further validating the algorithm performance.

Overall, we aimed to show the potential of FDWLs for offshore wind resource assessment as a standalone instrument and the ability of an algorithm to estimate atmospheric stability from the FDWL wind speeds only. As further steps, we would like to evaluate the algorithm's performance against direct measurements

of both momentum and heat fluxes taken over the same range of heights. Additionally, a comparison between the 2D-algorithm and other methods based on MOST relationships is still required.

Chapter 5

On the retrieval of surface-layer parameters from lidar wind-profile measurements

This Chapter revisits two recent methodologies based on Monin-Obukhov Similarity Theory (MOST), the 2D method by Araújo da Silva et al. (2022a) and Hybrid-Wind (HW) by Basu (2019), which are aimed at estimation of the Obukhov length, friction velocity and kinematic heat flux within the surface layer. Both methods use wind-speed profile measurements only and their comparative performance requires assessment.

5.1 Introduction

Wind energy is one of the most cost-efficient renewable power-generation technologies nowadays. Accordingly, the amount of onshore and offshore wind farms being installed worldwide has greatly increased over the last years (GWEC, 2022). Nevertheless, the onshore sector has become comparatively less attractive in terms of wind conditions and capacity factor as well as it has faced resistance by populations from potential deployment areas that may be affected by the farm installation and operation, hence the industry development has been moving towards offshore (Hevia-Koch & Jacobsen, 2019b; WindEurope, 2020). However, despite of the abundant wind resource that can be found over the seas, offshore wind farms harvesting remains more expensive than its onshore counterpart. Additionally, the

site's feasibility still relies on offshore meteorological masts (metmasts), which are very expensive to install and maintain (Peña et al., 2022).

During the last decade, floating Doppler wind lidars (FDWLs) have emerged as the wind-energy-industry preferred solution to replace the metmast because of its accuracy and attractive cost-benefit of installation and maintenance. Many studies have shown that 10-min averaged wind-speed measurements from FDWLs are numerically equivalent to reference observations from anemometers or fixed Doppler wind lidar (DWL) (Peña et al., 2022; Araújo da Silva et al., 2022a; Gutiérrez-Antuñano et al., 2017). However, FDWLs cannot measure a number of the atmospheric parameters that instruments mounted on meteorological masts can, which restrains commercial acceptance of FDWLs as stand-alone sensing instrument.

The *surface layer* is the lowest part of the atmospheric boundary layer (ABL) where turbulent fluxes vary by less than 10% of their magnitude (Stull, 2015). Thus, under stable stability conditions, ABL heights are of a few hundreds of meters or less. Under convective (i.e., unstable) stability conditions, ABL heights can be up to of a few kilometers. A measure of atmospheric stability is the *Obukhov length*, which has been used to extend the logarithmic wind profile to account for atmospheric stability conditions (Holtslag et al., 2015). The Obukhov length is directly related and very sensitive to the *friction velocity*. The latter is a fundamental velocity scale of atmospheric flow and can also be used to estimate the wind-speed standard deviation, which determines, together with the mean wind speed, turbulence intensity (Türk & Emeis, 2010). The role of the Obukhov length and friction velocity has been investigated in different wind-energy studies related to wind-turbine wake modelling (Göçmen et al., 2016), power production (Lopez-Villalobos et al., 2022), and structural loading (e.g., wind-turbine aeroelastic design) (Gao et al., 2021). It is worth noting that the eddy-covariance method, from which one can derive the friction velocity and heat flux is up-to-date the most accurate way to derive the Obukhov length (Stull, 1988, 2015). Estimations, however, can be alternatively performed using, e.g., the Richardson number (Grachev & Fairall, 1997).

Multiple sensors, such as sonic anemometers installed on metmasts, provide high-frequency measurements, which can be used to derive turbulent fluxes. Other sensors can provide air-pressure and air-humidity observations. However, alternative methods are needed in scenarios with limited instrumentation (Berkowicz & Prahm, 1982; Klug, 1967; Swinbank, 1964; Lo, 1979; Beljaars et al., 1989; Basu,

2019; Araújo da Silva et al., 2022a). A good number of these methods use Monin-Obukhov similarity theory (MOST), which implies a wind-speed profile that is monotonically increasing with height. The assumptions in MOST are valid within the surface layer only; therefore, MOST-based methods can normally be used to predict wind speeds up to approximately 100 m (Gryning et al., 2007; Holtslag et al., 2015).

The methods for estimation of surface fluxes of momentum and heat (i.e., surface-layer parameters) by Beljaars et al. (1989) and Berkowicz & Prahm (1982) require both temperature and wind-speed measurements, and that by Klug (1967) the aerodynamic roughness length in addition. When looking for studies utilising *only* wind-speed measurements as a feasible alternative to be applied using FDWL observations the number of surface-layer-retrieval methods are limited to four (Swinbank, 1964; Lo, 1979; Basu, 2019; Araújo da Silva et al., 2022a). Nevertheless, the reliability of the optimisation method proposed by Lo (1979) can be considered questionable because of different mathematical issues reported by Zhang (1981). Of the remaining three methods, the recent one by Basu (2019) –the so-called Hybrid-Wind (HW) method–is an enhanced version of the Swinbank (1964), in which the surface-layer wind profile follows an exponential profile instead of MOST (Businger et al., 1971; Dyer, 1974; Peña et al., 2009; Holtslag et al., 2015; Araújo da Silva et al., 2022a). HW estimates the Obukhov length from three levels of wind speed measurements. Once the Obukhov length is obtained, the friction velocity and surface heat flux can be derived. In contrast to HW, the 2D method by Araújo da Silva et al. (2022a) enables a simultaneously retrieval of the Obukhov length and friction velocity by using a two-dimensional (2D) parametric-solver algorithm. Besides, the 2D algorithm can be extended to any number of measurement heights describing the wind profile.

In the present work, we aim at assessing the performance for retrieval of surface-layer parameters of both the 2D and HW methods. Performance evaluation is twofold: First, we use reference synthetic noise-corrupted wind-profile realizations with characteristic parameters inherited from FDWL observational datasets. And, second, we use sonic-anemometer estimates from the IJmuiden metmast. Focus is also given to the stand-alone capability of these methods for atmospheric stability estimates.

This paper is structured as follows. Section 5.2 presents the observational campaign at the IJmuiden site. Section 5.3 reviews MOST and revisits the 2D and HW retrieval algorithms. Section 5.4 studies the comparative performance of both the

2D and HW methods as a function of the noise-corrupting intensity and stability condition with reference to synthetic and observational data. And, Section 5.5 provides concluding remarks.

5.2 Materials

This Chapter uses uses data from the IJmuiden observational campaign. Refer to Sect. 2.2.3 for a detailed review of the related instruments.

The numerical simulations (Sect. 5.3.4) were performed using the High Performance Computing environment CALCULA. CALCULA uses as a basis the resource management system Slurm Workload Manager, a scheduler of open source tasks widely used in supercomputing environments, and the system of GlusterFS distributed files for data management.

5.3 Methods

5.3.1 MOST wind profile

According to MOST, the diabatic wind profile (i.e., under non-neutral conditions) within the surface layer is expressed as

$$U_{MOST}(z) = \frac{u_*}{\kappa}\left[\ln\left(\frac{z}{z_0}\right) - \Psi_m\left(\frac{z}{L}\right)\right], \tag{5.1}$$

where z is the height [m], u_* is the friction velocity [m/s], $\kappa \approx 0.4$ is the Von Kármán constant, z_0 is the roughness length, L is the Obukhov Length, and $\Psi_m\left(\frac{z}{L}\right)$ is an stability-correction function (Stull, 1988; Barthelmie, 1999):

$$\Psi_m\left(\frac{z}{L}\right) = \begin{cases} -\beta\frac{z}{L} & \frac{z}{L} > 0 \text{ (stable)} \\ 0 & \frac{z}{L} = 0 \text{ (neutral)} \\ 2\ln(\frac{1+x}{2}) + \ln(\frac{1+x^2}{2}) - 2\arctan(x) + \frac{\pi}{2} & \frac{z}{L} < 0 \text{ (unstable)} \end{cases}, \tag{5.2}$$

where $x = \left[1 - \frac{\gamma z}{L}\right]^{1/4}$, and $\beta = 6.0$ and $\gamma = 19.3$ are empirical constants suggested by Högström (1988), which where already validated by Araújo da Silva et al. (2022a) and Holtslag et al. (2015) for the IJmuiden site.

The Obukhov length is a scaling parameter that is proportional to the height above the surface layer at which buoyant factors first dominate over mechanical production of turbulence (Stull, 1988). The Obukhov length can be computed from:

$$L = \frac{-\overline{\theta}_v u_*^3}{\kappa g (\overline{w'\theta'_v})_s}, \tag{5.3}$$

where $\overline{\theta}_v$ is the virtual potential temperature, w is the vertical wind component, $(\overline{w'\theta'_v})_s$ is the surface-layer virtual kinematic heat flux, and $g = 9.8\, m/s^2$ is the gravitational acceleration. The overbar indicates average over time (normally 10 min). The "prime" in w' and θ'_v denotes the fluctuating part of these components, i.e., the deviations from their respective mean values.

Offshore, the roughness length can be modelled through the Charnock's relationship as (Charnock, 1955)

$$z_0 = \alpha_c \frac{u_*^2}{g}, \tag{5.4}$$

where $\alpha = 0.012$ is the Charnock's constant and $g = 9.81$ [m/s^2] is the gravitational acceleration (Peña & Gryning, 2008; Holtslag et al., 2015). By inserting Eq. 5.4 into Eq. 5.1, the latter equation can be written as a function of only variables Obukhov length and friction velocity as

$$U(z, L, u_*) = \frac{u_*}{\kappa} \left[\ln \left(\frac{z}{\alpha_c \frac{u_*^2}{g}} \right) - \Psi_m \left(\frac{z}{L} \right) \right]. \tag{5.5}$$

Despite the simplicity of Charnock's model (Eq. 5.4), this model has the advantage of only depending on one of the variables that are being searched for (u_*). Physically, because of the overall low roughness over water, the sensitivity of any retrieval method to the roughness length *per se* is very small (and hence to the Charnock's constant).

Figure 5.1 revisits MOST, i.e., Eq. 5.1, for different stability conditions and sensitivity analysis in these two variables. Figure 5.1a shows that the wind profile in neutral stability conditions appears as a straight line with logarithmic height. In stable conditions the wind profile is concave downwards, while in unstable conditions is concave upwards. Note that MOST models wind profiles in which the wind speed monotonically increases with height, i.e., the wind profile has positive gradients at all heights (Basu, 2019, 2018). Figure 5.1b and c) show that the wind profile is much more sensitive to friction velocity u_* than to the Obukhov length L. The wind profile is virtually insensitive to perturbations in the sea roughness length.

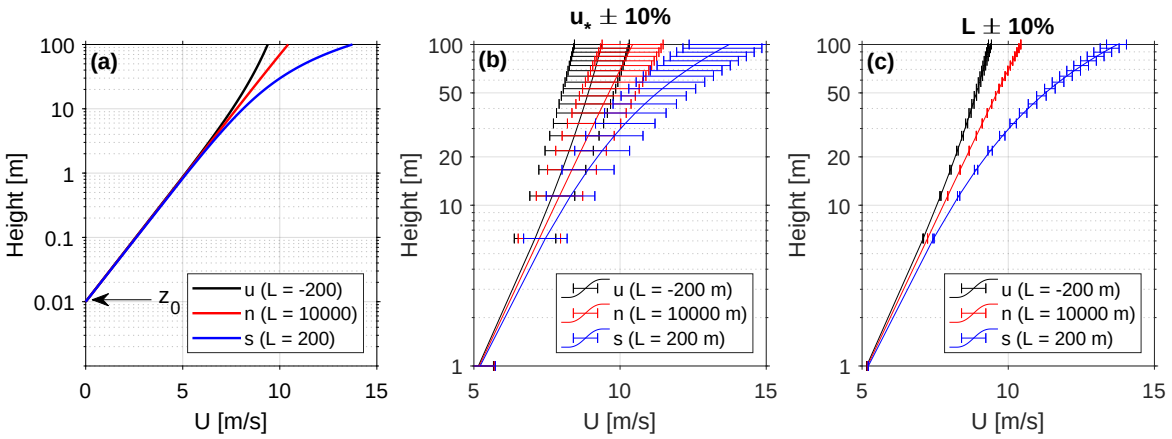

Figure 5.1: MOST wind profiles (Eq. 5.1) and numerical sensitivity. (a) MOST model for different stability conditions. *(u)* is unstable, *(n)* is neutral and *(s)* is stable. (b) Sensitivity to the friction velocity, u_*. (c) Sensitivity to the Obukhov length, L. (All panels) Simulation parameters: $z_0 = 0.01$ m, $u_* = 0.45$ m/s and $L = -200, 10000$, and 200 m (see legends). Error bars computed by applying a 10% perturbation to the nominal value of the variable under study.

5.3.2 Surface-layer parameter retrieval methods based solely on wind speed profiles

The 2D method

The 2D parametric solver algorithm *simultaneously* estimates the friction velocity, u_*, and Obukhov length, L, relying on MOST and wind-profile measurements only (Araújo da Silva et al., 2022a). The algorithm estimates model parameters (L,u_*) by minimising the norm of residuals between the model vector $\vec{U}_{MOST}(L, u_*)$, Eq. 5.5, and the observed wind-profile vector $\vec{U}_{obs}$, via constrained least-squares optimisation. Thereby, the optimisation problem is formulated as

$$(\hat{L}, \hat{u}_*) = \arg\min_{L,u_*} ||\vec{U}_{obs} - \vec{U}_{MOST}(L, u_*)||^2. \tag{5.6}$$

Two optimisation branches, one for $\Psi_m\left(\frac{z}{L}\right) > 0$ and another for $\Psi_m\left(\frac{z}{L}\right) < 0$, are considered for enhancing the sensitivity of the algorithm and avoiding the asymptotic discontinuity, $|\Psi_m\left(\frac{z}{L}\right)| \to 0$. The branch that yields the smallest residual norm is chosen as the solution. Once L and u_* are obtained, the heat flux is estimated from the definition of L (Eq. 5.3) as

$$\overline{w\theta} = -\frac{\theta_0 u_*^3}{\kappa g L}, \tag{5.7}$$

where $\theta_0 = 300K$ is assumed as the reference potential temperature (Basu, 2018). Equation 5.7 is just a plausible approximation of the surface-layer heat flux $(\overline{w'\theta'_v})_s$

in Eq. 5.3, whose calculation would require sonic-anemometer and humidity-sensor measurements.

The Hybrid-Wind method

The HW method is a MOST-based algorithm that primarily retrieves the Obukhov length from three height levels of a horizontal wind speed (HWS) profile (Basu, 2018). Given the Obukhov length and MOST profile Eq. 5.1, the friction velocity and heat flux are also obtained. Because the HW method is also reliant on MOST, the assumption of monotonic wind behaviour is inherent to the method (Sect. 5.3.1).

The HW reduces the number of MOST wind-profile parameters from three, namely, Obukhov length (L), friction velocity (u_*) and roughness length (z_0), to one primary parameter, the Obukhov length (L), by resorting to the ratio of the vertical wind-speed differences, which are formulated as (Basu, 2018)

$$\Delta U_{21} = U(z_2) - U(z_1) = \frac{u_*}{\kappa}\left[\ln\left(\frac{z_2}{z_1}\right) - \Psi_m\left(\frac{z_2}{L}\right) + \Psi_m\left(\frac{z_1}{L}\right)\right], \tag{5.8a}$$

$$\Delta U_{31} = U(z_3) - U(z_1) = \frac{u_*}{\kappa}\left[\ln\left(\frac{z_3}{z_1}\right) - \Psi_m\left(\frac{z_3}{L}\right) + \Psi_m\left(\frac{z_1}{L}\right)\right], \tag{5.8b}$$

where $U(z_i)$ is the HWS at the height z_i. Then, the ratio of wind speed differences is defined as

$$R(L) = \frac{\Delta U_{31}}{\Delta U_{21}} = \frac{\ln\left(\frac{z_3}{z_1}\right) - \Psi_m\left(\frac{z_3}{L}\right) + \Psi_m\left(\frac{z_1}{L}\right)}{\ln\left(\frac{z_2}{z_1}\right) - \Psi_m\left(\frac{z_2}{L}\right) + \Psi_m\left(\frac{z_1}{L}\right)}. \tag{5.9}$$

The ratio $R(L)$ is only function of Obukhov length L, which is retrieved via a non-linear least squares that fits the observed to the modelled vertical wind-speed ratio. Then, this retrieved Obukhov length L is used to solve friction velocity u_* from the formulation of HWS differences $\Delta U_{31}(u_*, L)$ and $\Delta U_{21}(u_*, L)$ expressed in Eq. 5.8 above via ordinary linear least squares. After estimating L and u_* the heat flux can also be estimated via Eq. 5.7. This procedure is identical for the 2D method once L and u_* are known.

5.3.3 Observational reference retrievals

10-min averages of the observations from the Ijmuiden metmast are used to determine the reference data as:

(i) *Reference Richardson-number-estimated Obukhov length, L_{Ri}.*- Because high-frequency temperature data from the sonic anemometers were not stored, the Obukhov length was estimated via bulk Richardson number using the methodology proposed by Grachev & Fairall (1997). L_{Ri} was computed as described in Araújo da Silva et al. (2022a) (see Sect. 4.3.4).

(ii) *Reference friction velocity.*- The sonic anemometers were installed at 85 m in height, which may well lie above the surface layer. Therefore, *two approximate reference friction-velocity values* were computed:

(ii.a) The *local friction velocity at 85 m* via the sonic-anemometer measurements as (Stull, 2015):

$$u_{*_{sonic}} = \left(\overline{u'w'}^2 + \overline{v'w'}^2\right)^{1/4}, \tag{5.10}$$

where u, v, and w denote the longitudinal, lateral and vertical wind components, respectively.

(ii.b) The so-called *1D friction velocity*, denoted $u_{*_{1D}}$. The 1D friction velocity was numerically derived by solving Eq. 5.5 for u_* given the Richardson-number-estimated Obukhov length (L_{Ri}, refer to Sect. 4.3.4) and the measured wind-speed at 27 m, which is the lowest height available from the metmast. Accordingly, u_* becomes the only unknown in Eq. 5.5 (hence the one-dimensional (1D) suffix used), which is solved via least-squares optimisation.

5.3.4 Synthetic data generation

2D and HW retrieval accuracies were examined by using random sets of synthetic wind profiles, $U^{syn}(z)$, generated for different atmospheric conditions. Monte-Carlo simulation was used to generate synthetic pairs (u_*^{syn}, L^{syn}) compliant with MOST (Eq. 5.1). This is explained next:

Generation of Obukhov length and friction velocity random pairs

The variables Obukhov length and friction velocity are physically related via Eq. 5.3. Consequently, random sets for these variables cannot be created using the customary assumption of independent Gaussian random variables. To circumvent this problem, in Eq. 5.3 we recognise that L is proportional to the cube of the

friction velocity and the ratio $\overline{\theta}_v/(\overline{w'\theta'_v})_s$, which is denoted factor c in what follows. Hence, Eq. 5.3 can be rewritten as

$$L = -\frac{c}{kg}{u_*}^3. \tag{5.11}$$

From Eq. 5.11 above, it arises that Obukhov length L is unambiguously defined by friction velocity u_* and factor c or, equivalently, that random values for u_* and c must be generated from the Probability Density Functions (PDFs) of independent random variables U_* and C, respectively. Here *upper-case* letters denote random variables and *lower-case* letters denote the values for these variables. Because the PDFs for random variable friction velocity U_* and random variable C-factor are "a priori" unknown, they have to be estimated. This was done from the whole set of IJmuiden metmast measurements recorded during the campaign (8,278 records, hereafter "the statistical sample") as follows: the PDF for U_* was approximated by that of local friction velocity $U_{*_{sonic}}$ computed via Eq. 5.10 over the statistical sample. The PDF for C was derived from the estimates of this variable computed as $C \approx -\frac{kgL_{Ri}}{{U_{*_{sonic}}}^3}$ over the statistical sample, where L_{Ri} is the Richardson-number-estimated Obukhov length (see Sect. 4.3.4).

Different PDFs models were experimentally fitted to the estimated friction velocity U_* and factor-C distributions in order to obtain the PDFs that best described the observations. As a result, it could be observed that both U_* and C followed a log-normal distribution or the combination of a log-normal with a folded version of it. The log-normal PDF for a random variable X is formulated as

$$f_X(x) = \frac{1}{\sigma_X\sqrt{2\pi}} e^{-\frac{[\ln(x)-\mu_X]^2}{2\sigma_X^2}}, \quad x > 0, \tag{5.12}$$

where μ_X and σ_X are the PDF constitutive parameters.

Because the log-normal PDF is positive defined, it becomes an appropriate distribution to describe the friction velocity PDF, denoted $f_{U_*}(u_*)$. In contrast, because variable C can have positive and negative values, its PDF is defined log-normal piecewise as

$$f_C(c) = \begin{cases} f_{C_p}(c_p), c_p = c, & if \quad c > 0, \\ f_{C_n}(c_n), c_n = -c, & if \quad c < 0, \end{cases} \tag{5.13}$$

where $f_{C_p}(c_p)$ and $f_{C_n}(c_n)$ are the log-normal ($X = C_p$, Eq. 5.12) and folded log-normal ($X = C_n$) PDFs associated to positive and negative values of C, denoted c_p and c_n, respectively. As mentioned, upper-case letters denote random variables

and lower-case letters denote values for these variables. In what follows, this notation formality is skipped unless otherwise necessary for understanding.

By fitting: *(i)* Eq. 5.12 PDF with $X = U_*$ to the statistical sample of *local friction-velocity* values measured at 85m ($U_{*_{sonic}}$, Sect. 5.3.3), and *(ii)* Eq. 5.13 PDF to the C-factor sample computed as $C \approx -\frac{kgL_{Ri}}{{U_{*_{sonic}}}^3}$, then PDF characteristic parameters, $\mu_X = \mu_{u_*}$ and $\sigma_X = \sigma_{u_*}$ for $f_{U_*}(u_*)$, and $\mu_X = \mu_{C,p}, \mu_{C,n}$ and $\sigma_X = \sigma_{C,p}, \sigma_{C,n}$ for $f_C(c)$ can be estimated. Once PDFs $f_{U_*}(u_*)$ and $f_C(c)$ are characterised, random values u_*^{syn} and c^{syn} can be generated computationally. Most data-processing software packages provide built-in algorithms able to generate log-normal-distributed random values. Alternatively, log-normal distributions can be obtained by transforming uniformly distributed random values through the inverse log-normal cumulative distribution function. Thus, log-normal distributed values y can be obtained using the transformation (Devroye, 2013)

$$y = e^{\mu + \sqrt{2\sigma^2} erf^{-1}(2x-1)}, \tag{5.14}$$

where x are random values from a uniformly distributed random variable, and erf^{-1} is the inverse Gauss error function. Once random values u_*^{syn} and c^{syn} have been generated, L^{syn} values can readily be computed from Eq. 5.11.

Generation of synthetic wind profiles

Model wind profiles, $U^{MOST}(z)$, can be generated from the pairs (u_*^{syn}, L^{syn}) via MOST (Eq. 5.1). However, model profiles are noiseless and, in practice, there are always deviations from the MOST profile. In order to emulate these deviations, height-independent zero-mean Gaussian-noise realizations are added to the noiseless model profiles. This can be expressed as

$$U_{syn}(z_i) = U_{MOST}(z_i) + \sigma_n \nu(z_i), \quad i = 1 \dots N, \tag{5.15}$$

where U_{syn} is the noise-corrupted wind profile (hereafter, the *synthetic* wind profile), U_{MOST} is the MOST profile (Eq. 5.1), ν is zero-mean, unit-standard-deviation Gaussian noise, z_i is the *i-th* metmast anemometer-measurement height ($z_i = 27, 58.5, 85$ m, Sect. 5.2), and N is the number of measurements heights.

We quantify the intensity of these perturbations by means of the normalised root-mean-squared error (N_{RMSE}, hereafter, the *normalised noise level*), which is de-

fined in percentage units as

$$N_{RMSE} = 100 \times \sqrt{\frac{1}{N}\sum_{i=1}^{N}\frac{[U_{MOST}(z_i) - U_{mast}(z_i)]^2}{\overline{U_{mast}}}}, \tag{5.16}$$

where U_{mast} is the measured wind profile from the metmast anemometers at height z_i.

The noise-corrupting amplitude is defined as the standard deviation,

$$\sigma_n = \frac{N_{RMSE}\overline{U_{mast}}}{100}, \tag{5.17}$$

where the overbar indicates average over the measurement heights 27, 58.5 and 85 m. From Eq. 5.17, it follows that the normalised noise level (Eq. 5.16) quantifying the noise-corrupting perturbational amplitude in synthetic wind profiles can also be rewritten as $N_{RMSE} = \frac{\sigma_n}{\overline{U_{mast}}}100[\%]$.

Figure 5.2 block diagram summarizes the procedure for synthetic wind-profile generation. First, random pairs (u_*^{syn}, c^{syn}) are generated from PDFs $f_{U_*}(u_*)$ and $f_C(c)$ as described in Sect. 5.3.4. Then, L^{syn} values are computed from u_*^{syn} and c^{syn} values via Eq. 5.11. Next, each "seed" pair (u_*^{syn}, L^{syn}) is used to produce a noiseless MOST profile, $U_{MOST}(z)$, via Eq. 5.1. Finally, zero-mean, σ_n-standard-deviation Gaussian noise $\nu(z)$ (Eq. 5.17) is added to the model wind profile $U_{MOST}(z)$ in order to yield noise-corrupted wind profile $U_{syn}(z)$.

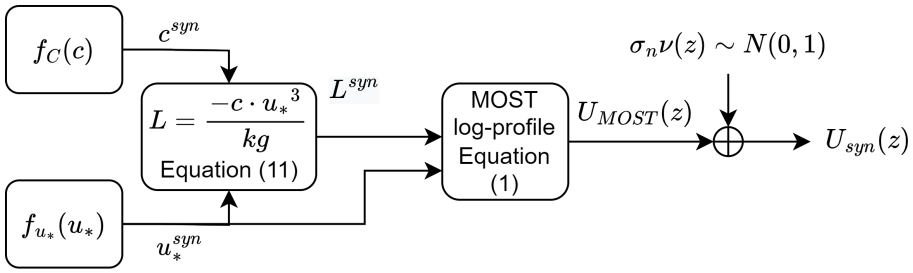

Figure 5.2: Block diagram summarising the procedure to generate synthetic pairs (u_*^{syn}, L^{syn}) and corresponding noise-corrupted wind profiles, $U_{syn}(z)$.

The absolute relative error between the estimated and the synthetic friction velocity, the latter taken as reference, is computed as:

$$\epsilon_{u_*} = \frac{|\hat{u}_* - u_*^{syn}|}{u_*^{syn}} \tag{5.18}$$

where $\hat{u}_*$ is the estimated friction velocity and u_*^{syn} is the synthetic one.

5.4 Results and Discussion

We study the comparative performance of 2D and HW methods as a function of the noise level and atmospheric stability conditions. First, Sect. 5.4.1 shows the synthetic generation of the friction-velocity-to-Obukhov-length distribution proxy for the Ijmuiden dataset, which becomes our *synthetic "truth" reference* for comparison. Sections 5.4.2 and 5.4.3 evaluate the performance of the 2D and HW methods with reference to *synthetic* and *observational* data, respectively.

5.4.1 On the generation of synthetic wind profiles

To begin with, a *dataset* consisted of 5,000 randomly-generated samples, where each *sample* stands for one *pair* friction velocity and Obukhov length, (u_*^{syn}, L^{syn}), and its respective *noisy wind profile.* Each of these pairs is represented by a red dot in Fig. 5.3, which, in turn, is associated to a MOST profile (i.e., noiseless). MOST profiles were generated using the same measurement heights as for the FDWL (i.e., 25, 38, 56 and 85 m, see Sect. 5.2). To obtain a sample noisy wind profile, a noise realization with noise level N_{RMSE} was added to the MOST profile (Eq. 5.15). Based on the measured distribution of the normalised noise level (N_{RMSE}) shown in Fig. 5.4d (explained next), in our simulations, we considered 20 *noise levels* (Eqs. 5.16–5.17) spanning from $N_{RMSE} = 0$ to 60%. For each of these 20 noise levels, a noise realization was added to each of the 50 5,000-sample datasets in order to ensure statistical significance. Therefore, the total number of generated samples was: $20\, noise\, levels\, 50 \frac{dataset}{noise\, level}\, 5,000 \frac{samples}{dataset} = 5,000,000\, samples$.

Practical generation of the synthetic wind profiles in relation to Ijmuiden campaign is described in Sects. 5.4.1–5.4.1 next: Section 5.4.1 details estimation of the characteristic parameters of PDFs $f_{U_*}(u_*)$ and $f_C(c)$ (so-called "seed" PDFs), and generation and quality assurance of the synthetic random pairs (u_*^{syn}, L^{syn}); Sect. 5.4.1 addresses estimation of the distribution the of noise level, N_{RMSE}, from Ijmuiden campaign; and Sect. 5.4.1 tackles the issue of outlier rejection for synthetic samples versus MOST.

Inference of "seed" PDF characteristic parameters and quality assurance

The IJmuiden campaign consisted of 8,278 measurement records after outlier rejection (refer to (Araújo da Silva et al., 2022a), pp. 10–11 for details; in short, rejected measurements were: (i) FDWL-measured HWS values lower than 2 m/s

and higher than 80 m/s, and (ii) FDWL-measured spatial variation values higher than 0.055).

First, the PDFs for the friction velocity, $f_{U_*}(u_*)$, and C-factor, $f_C(c)$, were inferred from the measured distributions of the sonics-derived friction velocity ($U_{*_{sonic}}$) and Richardson-number-estimated Obukhov length (L_{Ri}) as described in Sect. 5.3.4. When fitting model PDF Eq. 5.12 to the measured friction-velocity, characteristic parameters $\mu_{u_*} = -1.36$ and $\sigma_{u_*} = 0.52$ were obtained, which described $f_{U_*}(u_*)$. Analogously, when model PDF Eq. 5.13 was fitted to the measured C-factor distribution, $\mu_{C,p} = 10.29$ and $\sigma_{C,p} = 0.52$, and $\mu_{C,n} = 10.96$ and $\sigma_{C,n} = 1.11$ resulted, hence completely describing $f_C(c)$. Next, once model PDFs $f_{U_*}(u_*)$ and $f_C(c)$ were found, random pairs (u_*^{syn}, L^{syn}) were generated.

Concerning quality assurance, in order to ensure trustworthy *synthetic* datasets in comparison to the observational ones gathered at Ijmuiden, we generated 8,278 (u_*^{syn}, L^{syn}) pairs and compared the u_*^{syn}-to-$1/L^{syn}$ (i.e., the friction-velocity-to-reciprocal-Obukhov-length) distribution to the $u_{*_{sonic}}$-to-$1/L_{Ri}$ distribution measured at IJmuiden. The outcome of this exercise is depicted in Fig. 5.3. As it can be observed in Fig. 5.3a, the distribution of the synthetic pairs (red dots) virtually overlaps that of the measured pairs (black dots), which validates the synthetic generation method described in Sect. 5.3.4. In addition, Fig. 5.3b shows the histogram of the reciprocal of the Obukhov length distribution for both the synthetic and measured datasets, which are virtually identical.

Estimation of the noise level distribution from observational data

In Sect. 5.3.4 we found that the normalised noise level (N_{RMSE}, Eq. 5.16) could be understood as an indicator of the average noise level in the wind profile. In order to estimate typical values for this normalised wind-perturbance intensity indicator, we computed the normalised RMSE between the MOST-predicted and metmast-measured wind profiles.

The MOST-predicted wind profile was computed through the 1D friction velocity, $u_{*_{1D}}$, and Richardson-number-derived Obukhov length, L_{Ri}, in Eq. 5.1 (refer to Sect. 5.3.3 and Sect. 4.3.4). Figure 5.4 compares the MOST-predicted to the metmast-measured wind speed at the three measurement heights (Fig. 5.4a-c) and derives the resulting normalised RMSE distribution (Fig. 5.4d). The virtually ideal 1:1 regression line obtained at 27-m height (Fig. 5.4a) is because $u_{*_{1D}}$ was numerically retrieved using the metmast-measured wind-speed at this same height. Since

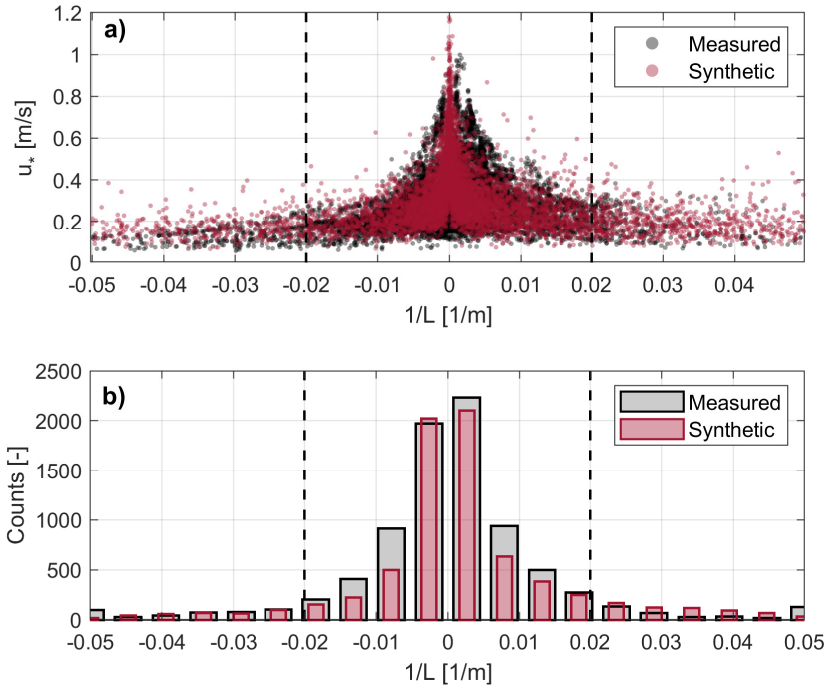

Figure 5.3: Synthetic data quality assurance. (a) Comparison between *synthetic* (red dots) and *measured* (black dots) distributions of friction-velocity and Obukhov-length as (u_*^{syn}, $1/L^{syn}$) pairs. (b) Obukhov-length histograms for the measured and synthetic pairs. X-axis plots reciprocal Obukhov length in 0.005 m^{-1}-width bins.

the uncertainty of the MOST model increases with height, linear regression indicators tend to decrease with it. Thus, at 58.5 m, Fig. 5.4b, slope = 0.90, intercept = 0.15, $\rho^2 = 0.97$; at 85 m, Fig. 5.4c, slope = 0.83, intercept = 0.46, $\rho^2 = 0.93$. By merging all the measurement samples from Figs. 5.4a-c into Eq. 5.16, the histogram bar chart for the normalised RMSE could be derived (Fig. 5.4d). The mean and median normalised RMSE were, $N_{RMSE} = 12\%$ and 8%, respectively, which is descriptive of the statistical noise levels found in real practice in Ijmuiden.

MOST monotonicity and outlier rejection criteria

Synthetic *samples* (refer to *italicised* words at the beginning of Sect. 5.4.1 for terminology) were filtered out according to the following outlier rejection criteria:

- (i) Because MOST inherently assumes that wind speed monotonically increases with height, synthetic noisy wind profiles that did not fulfil this assumption were excluded from the *dataset*.

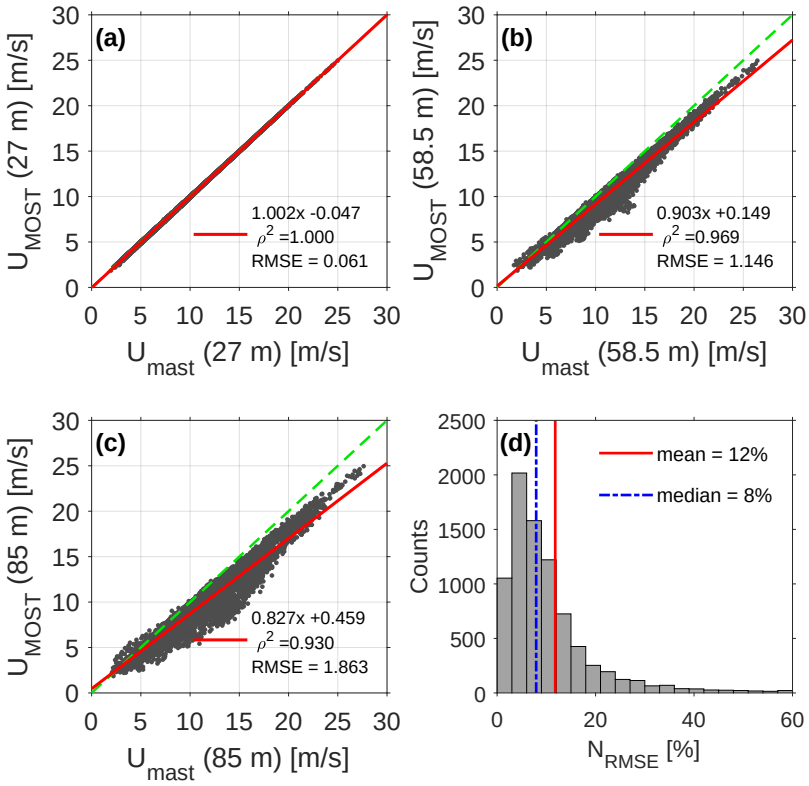

Figure 5.4: Estimation of normalised noise level N_{RMSE} from metmast observations. (a), (b) and (c) Comparison between the MOST-predicted (Eq. 5.1) and mast-measured wind speed at the three measurement heights. Dashed green line is the ideal 1:1 line. Red line is the linear regression line. (d) Distribution of normalised noise level N_{RMSE} (Eq. 5.16), computed between predicted and reference wind-speed profiles for the whole observational campaign.

- (ii) Obukhov-length values in the $-50\ m < L < 50\ m$ interval were rejected as outliers in order to avoid Eq. (5.2) singularity when $L \to 0$ m (Kretschmer et al., 2018; Araújo da Silva et al., 2022a; Gryning et al., 2007).

Although some authors (Araújo da Silva et al., 2022a; Gryning et al., 2007) propose the $-50\ m < L < 10\ m$ interval, our choice (Kretschmer et al., 2018) enables symmetrical rejection of samples from the stable and unstable regimes. In addition, when the $-50\ m < L < 50\ m$ rejection interval is expressed in inverse form ($|1/L| > 0.02\ [1/m]$), this interval approximately corresponds to the 5th and 95th percentiles of the inverse Obukhov-length distribution, in which statistically less representative values occur (see Fig. 5.3b).

As a result from the outlier rejection criteria, the number of valid statistical

samples became smaller than the nominal simulation value of 5,000. Thus, Fig. 5.5 depicts the number of valid samples as a function of noise level N_{RMSE}. Valid samples were counted from all the 50 datasets generated for a given perturbational noise level (Sect. 5.4.1). For both the 2D and HW methods, the number of valid samples decreased with increasing noise level because the higher this level was, the higher the likelihood of occurrence of a non-monotonic wind profile was. Besides, the reduction in the number of valid samples was larger for the unstable condition ($L < 0$ m) on account of the fact that unstable wind profiles have lower wind shear (i.e., lower vertical wind-speed gradients) as compared to stable ones ($L > 0$ m). As a result, unstable profiles are more sensitive to noise perturbations and prone to turn non-monotonic. In addition, the HW had fewer valid samples than the 2D because a larger number of HW Obukhov-length estimates fell in the outlier interval $-50\ m < L < 50\ m$.

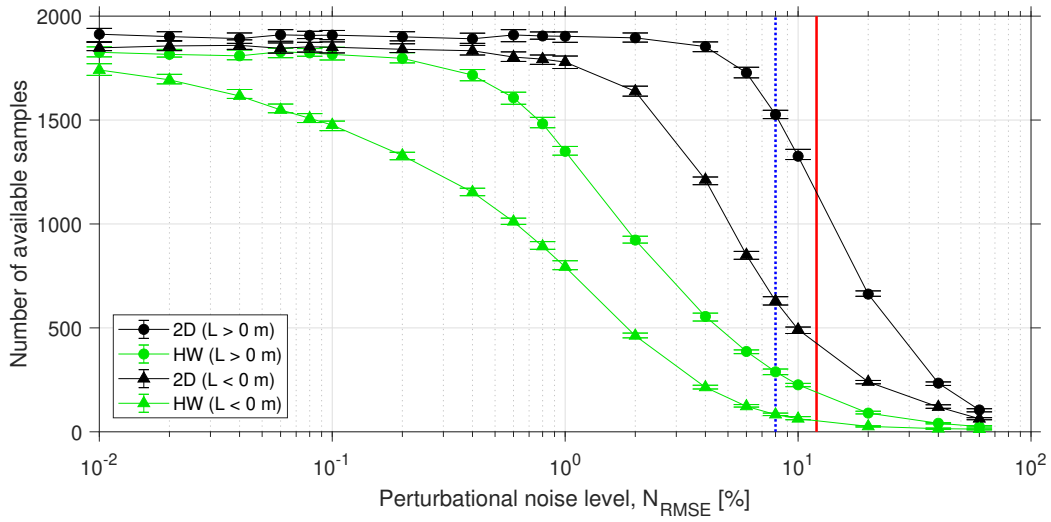

Figure 5.5: Distribution of the number of valid samples (i.e., after rejecting outliers) from all 50 datasets for a given noise level as a function of perturbational noise level N_{RMSE} (Eq. 5.16). *Symbols* indicate median levels. Lower and upper *error bars* depict 25th and 75th percentiles, respectively. (Blue and red lines) respectively correspond to the median (8%) and mean (12%) noise levels shown in Fig. 5.4d.

5.4.2 2D and HW performances with reference to synthetic data

Sensitivity to friction velocity

Figure 5.6 shows the retrieval error (Eq. 5.18) associated to the 2D- and HW-retrieved friction-velocity estimates ($\hat{u}_*^{2D}$ and $\hat{u}_*^{HW}$, respectively) as a function of reference synthetic friction velocity u_*^{syn} for two noise levels, $N_{RMSE} = 10\%$ (high

intensity) and $N_{RMSE} = 2\%$ (low). Because of the inherently stochastic nature of the perturbational noise, large dispersion in the error estimates (Eq. 5.18) is evidenced. To alleviate this issue, median error (50th percentile) lines are also plotted.

Prominently, it emerges that 2D retrievals consistently exhibited lower errors than HW ones for all friction velocities and noise levels. Thus, 2D estimates (Fig. 5.6a) showed median (peak) errors of $\simeq 5\%(30\%)$ for $u_*^{syn} = 0.1$ m/s, whereas HW estimates (Fig. 5.6b) yielded median (peak) errors as high as $\simeq 200\%(1,000\%)$. When regarding the absolute relative error versus noise level, the higher the noise level was, the higher the error was, as expected. Comparatively, the 2D median error at $N_{RMSE} = 2\%$ lay between 0.5% and 1%, and at $N_{RMSE} = 10\%$ between 2% up to 5%, whereas the HW median error at $N_{RMSE} = 2\%$ and $N_{RMSE} = 10\%$ lay between 30% and 150%, and 40% and 200%, respectively. The worse performance of the HW is due to the fact that this algorithm does a two-step estimation: first, L is estimated from the ratio of wind speed differences (Eq. 5.9) and, second, u_* is retrieved from the previously estimated Obukhov length (Eq. 5.8). As a result, the error incurred in the estimation of the Obukhov length propagates down to the friction velocity estimate. In contrast, the 2D algorithm retrieves both variables at once using a single multi-variate optimization process (Eq. 5.6), which does not propagate error between them.

Furthermore, for both algorithms, the error reduced with increasing friction velocity. This is in accordance with the study by Basu (2019) (p. 37, Fig. 4), who previously studied the sensitivity of the HW method to friction velocity under four different noise cases. In that study, case-4 scenario consisted of a multivariate Gaussian noise distribution with standard deviation $\sigma = 0.05$ m/s and the assumption of noise-correlated heights with correlation coefficient $\rho = 0.5$. That standard deviation ($\sigma = 0.05$ m/s) is equivalent to our noise level $N_{RMSE} = 2\%$ representing HWS deviations from MOST up to $\pm$ 0.2 m/s. Quantitative results are as follows: On one hand, Fig. 4 in Basu (2019) reported median errors between ≈50% and 8% for friction velocities between 0.1 and 1 m/s. On the other hand, we found (Fig. 5.6b) that the HW method attained median errors between 150% and 30% for $N_{RMSE} = 2\%$ within the same range of friction velocities. Therefore, both Basu (2019) and our study yield similar quantitative results, albeit a factor three higher error in our simulations due to the conservative assumption of uncorrelated noise.

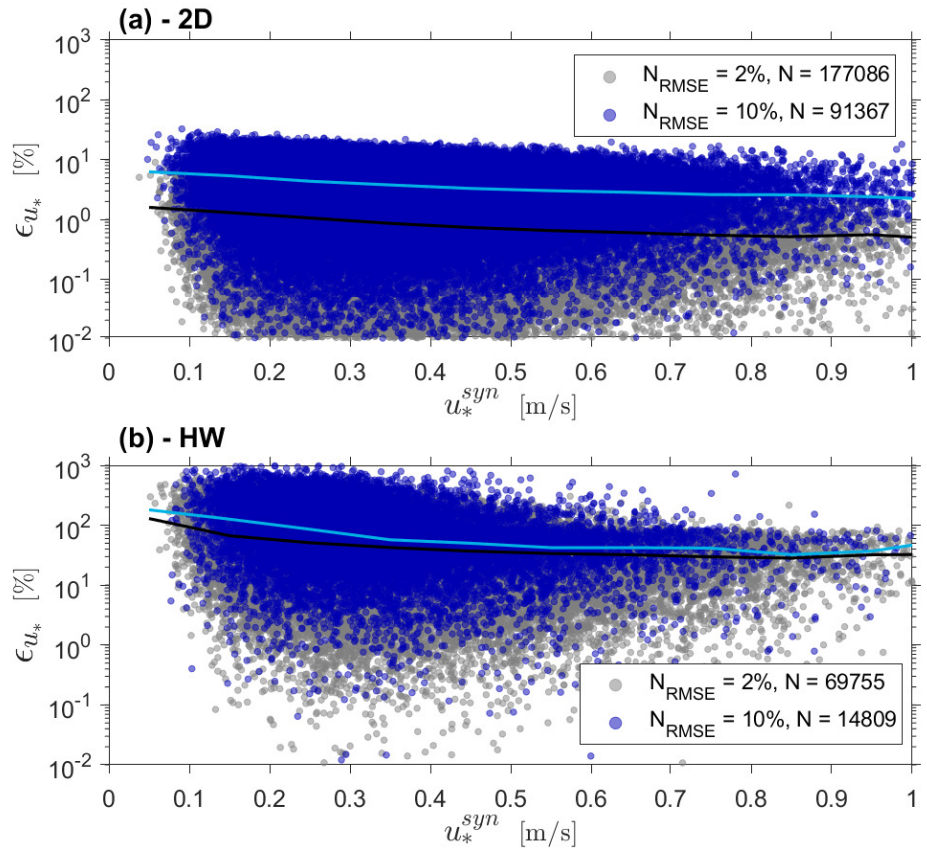

Figure 5.6: Absolute relative error between the estimated and reference synthetic friction velocity (Eq. 5.18) for two different noise levels (see legends). (a) 2D method. (b) HW method. (Blue trace) Median error at noise level $N_{RMSE} = 2\%$. (Black trace) Median error at $N_{RMSE} = 10\%$. N stands for number of samples.

Sensitivity to the perturbational noise level

Numerical analysis was used to assess 2D and HW algorithm performances for *friction velocity, Obukhov length,* and *heat flux* estimation. Towards this purpose, both algorithms computed these three parameters from each of the 50 datasets generated for each noise level (Sect. 5.4.1). The coefficient of determination (ρ^2) enabled to calculate the degree of correlation between each of the estimated parameters and their corresponding synthetic reference in each dataset. As a result, for each parameter and noise level a set of 50 coefficients of determination was obtained.

Figure 5.7 shows ρ^2 as function of noise level for the three parameters above. It can be observed that both the 2D and HW algorithms exhibited ideal performance ($\rho^2 = 1$) in the absence of noise ($N_{RMSE} \to 0$) for all three parameters As expected,

the coefficients of determination decreased with increasing noise, being the 2D method more robust to noise perturbations as shown by ρ^2 values higher than those from the HW algorithm.

Friction velocity (Fig. 5.7b) became the least sensitive parameter to noise as evidenced by much higher coefficients of determination than those obtained for the Obukhov length and heat flux. This is because friction velocity is proportional to the mean wind speed. As found in Sect. 5.4.2, 2D friction-velocity estimates were more accurate than HW ones. Thus, the 2D method yielded coefficients of determination $\rho^2 > 0.75$ for all simulated noise levels, whereas the HW dropped below 0.5 for noise levels higher than $N_{RMSE} = 5\%$. 2D friction-velocity estimates were unaffected by atmospheric stability, as evidenced by the stable-condition trace ($L > 0$ m, black solid) overlapping the unstable one ($L < 0$ m, grey dashed). On the other hand, HW friction-velocity exhibited higher performances in unstable conditions.

With regards to the *Obukhov length* (actually to its inverse $1/L$, Fig. 5.7a), the 2D algorithm was able to acceptably estimate of the Obukhov length in stable regimes ($L > 0$ m), yielding $\rho^2 \simeq 0.8$ at $N_{RMSE} = 8\%$ (which is the mean noise level, N_{RMSE}, found during the IJmuiden campaign, Fig. 5.4d). At this same noise level, the HW method showed $\rho^2 \approx 0$. The higher accuracy of the 2D algorithm in stable conditions was already reported by Araújo da Silva et al. (2022a). On the other hand, none of the methods was able to successfully estimate the Obukhov length in unstable conditions ($L < 0$ m). Quantitatively, ρ^2 values were virtually zero for $N_{RMSE} > 4\%$.

As far as the heat flux is concerned (Fig. 5.7c), the coefficients of determination obtained were similar to those for the Obukhov length in Fig. 5.7a, because the heat flux is a secondary parameter derived from u_* and L through Eq. 5.7. ρ^2 values were slightly higher for the Obukhov length than for the heat-flux retrievals when using the 2D algorithm, particularly, for high noise levels ($N_{RMSE} > 5\%$). A suitable explanation for that is propagation of the Obukhov-length estimation error to heat-flux estimates via Eq. 5.7.

5.4.3 2D- and HW-algorithm performances with reference to observational data

Performance of the two surface-layer retrieval algorithms was also evaluated with reference to metmast observational data gathered during the IJmuiden campaign (Sect. 5.2). 8,263 10-min FDWL-measured wind profiles were used as the sole input for the 2D and HW methods after prior removal of high spatial-variation data,

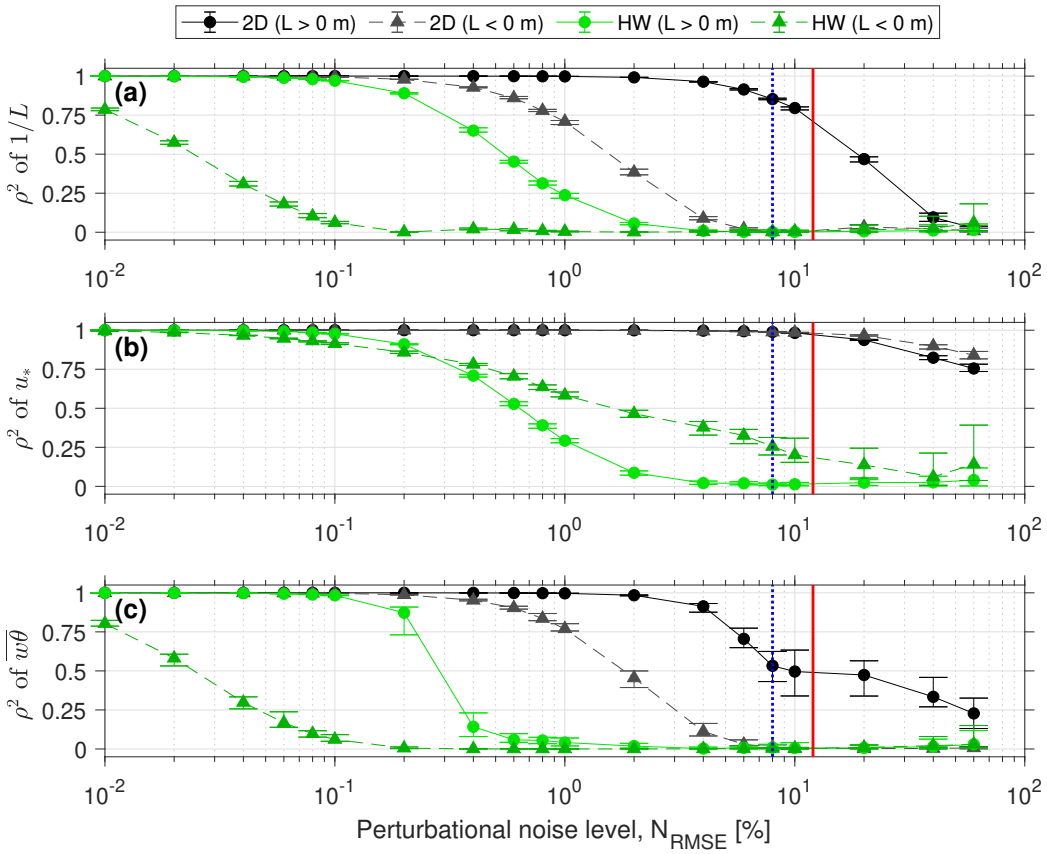

Figure 5.7: Performance statistics as a function of perturbational noise level N_{RMSE}. (a) Inverse of Obukhov length, $1/L$. (b) Friction velocity, u_*. (c) Kinematic heat flux, $\overline{w\theta}$. *Symbols* and *error bars*: Same format as in Fig 5.5. ρ^2 is the coefficient of determination.

and HWS values outside the range 2–80 m/s (refer to (Araújo da Silva et al., 2022a) for detailed FDWL outlier-filtering procedure). We verified that the coefficients of determination were higher than $\rho^2 = 0.996$ between the FDWL and anemometer measurements for the three metmast reference heights closest to the lidar (27, 58.5 and 85 m Sect. 5.2). After this verification step, the observational data collection was submitted to the same outlier rejection criteria as the ones applied over synthetic data (Sect. 5.4.1).

The *first part* of our analysis consisted of testing the capabilities of the 2D and HW algorithms for *typing* the observational wind profiles into three main atmospheric stability classes (Table 5.1) (Araújo da Silva et al., 2022a; Kretschmer et al., 2018): unstable (u), neutral (n), and stable (s). The L values used for the classification were the corresponding 2D- and HW-retrieved Obukhov lengths, denoted L_{2D} and L_{HW}, respectively.

Category	L **range [m]**
Stable (s)	$50 < L < 500$
Neutral (n)	$\|L\| > 500$
Unstable (u)	$-500 < L < -50$

Table 5.1: Relationship between atmospheric stability classes and the Obukhov length (refer to Sect. 5.4.1 (ii)).

Figure 5.8 plots the measured median normalized wind-speed profiles (normalized the wind speed at the lowest height, $U(z_1)$) for cluster categories u, n, and s derived from the 2D- and HW-retrieved Obukhov lengths (L_{2D} and L_{HW}, respectively) over the whole campaign. As observed, both 2D and HW algorithms were able to discern among the different stability types. The 2D algorithm enabled clearer discrimination among the three stability types and showed narrower non-overlapping error bars as compared to the HW. Further, the median wind-speed profiles in Fig. 5.8 follow MOST. For the 2D algorithm the behavior of the wind shear is clearly different for the number of stability classes.

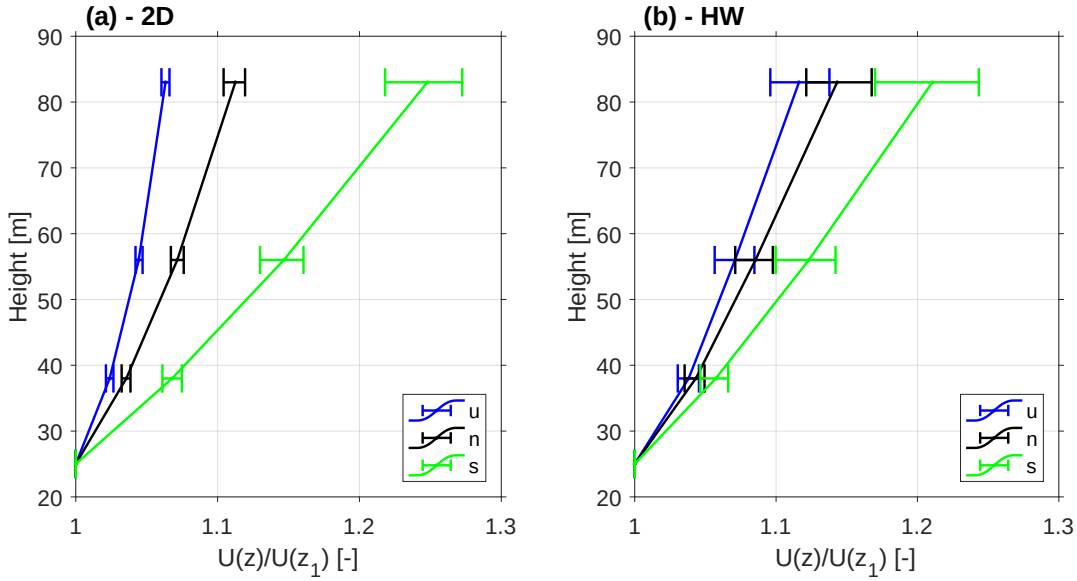

Figure 5.8: (Observational data, Sect. 5.4.3, part I) 2D and HW atmospheric stability typing performance (82-day time resolution): median wind-speed profiles measured by the FDWL during IJmuiden campaign clustered by stability classes (Table 5.1). Panels (a) and (b) show classifications based on the 2D- and HW-retrieved Obukhov lengths, L_{2D} and L_{HW}, respectively. *(u)* stands for *unstable*, *(n)* for *neutral* and *(s)* for *stable.* Error bars depict 40th-to-60th percentiles at each height (note that median is the 50th percentile in the very middle of the error bar).

The *second part* of our analysis tackled numerical evaluation of the 2D and HW

retrieval performances through direct comparison with *reference metmast retrievals*. The Richardson-number-based Obukhov-length, L_{Ri} (see Sect. 4.3.4), numerically-solved friction velocity, u_{*1D} (see Sect. 5.3.3), and heat flux, $\overline{w\theta}$, computed through Eq. 5.7 using L_{Ri} and u_{*1D}, were the references used in this study (Sect. 5.3.3).

Scatter plots comparing 2D- and HW-retrievals to the mast-derived reference estimates are shown in Fig. 5.9. Aimed at limiting linear regression (LR) analysis to the most meaningful samples, an additional de-noising filtering procedure named *histogrammed filtering* was applied as follows: the range for X-axis data (reference reciprocal-Obukhov-length range, $-0.05\ [1/m] < 1/L_{Ri} < 0.05\ [1/m]$) in Fig. 5.9a and Fig. 5.9d was divided into 0.002 [1/m]-width bins and, in each bin, the corresponding Y-values (estimated reciprocal-Obukhov-length values $1/L_{2D}$ in Fig. 5.9a, or $1/L_{HW}$ in Fig. 5.9d) outside the 15th-to-85th-percentile interval were rejected as outliers, therefore, excluded from the LR. At this point we note that the 15th-to-85th percentile is approximately one standard deviation of the mean in a *normal* distribution. For consistency, rejected samples in the Obukhov-length estimates (grey dots in Fig. 5.9a and d) were also rejected in the friction-velocity and heat-flux estimates (Fig. 5.9b-c and Fig. 5.9e-f, respectively).

After histogrammed filtering, the 2D method remained with $N = 2,426$ and $N = 1,230$ samples for the stable ($1/L_{2D} > 0\ [1/m]$) and unstable ($1/L_{2D} < 0\ [1/m]$) classes, respectively (see legends in Fig. 5.9) whereas the HW remained with 1,118 ($1/L_{HW} > 0\ [1/m]$) and 441 ($1/L_{HW} < 0\ [1/m]$) samples, respectively. Overall, the results of Fig. 5.9 agree with the previously found in Fig. 5.7 using synthetic data and show that the 2D excels the HW algorithm. Thus, the 2D-derived friction velocity, $u_{*_{2D}}$, outperformed all other retrievals regardless of the atmospheric stability condition (Fig. 5.9b using observational data and Fig 5.7b using synthetic data). And the HW-estimated friction velocity, $u_{*_{HW}}$, yielded coefficients of determination $\rho^2 = 0.47$ and 0.15 ($\rho^2 = 0.39$ and 0.12 without histogrammed filtering) for unstable and stable cases (Fig. 5.9e) in rough agreement with the 1D friction velocity results of Fig 5.7b, in which coefficients $\rho^2 = 0.25$–0 were respectively found at $N_{RMSE} = 8\%$ (the observational median noise level, Fig. 5.4d).

Finally, in the *third part* of our study we compared the 2D and HW friction-velocity estimates ($u_{*_{2D}}$ and $u_{*_{HW}}$) against the corresponding sonic-anemometer measurements ($u_{*_{sonic}}$), Fig. 5.10. For consistency, histogrammed outliers identified in Fig. 5.9a,d were also excluded in Fig. 5.10. Similar to the results found in Sect. 5.4.2, the 2D algorithm attained the best numerical indicators in both the stable and unstable atmospheric regimes, whereas the HW algorithm could only

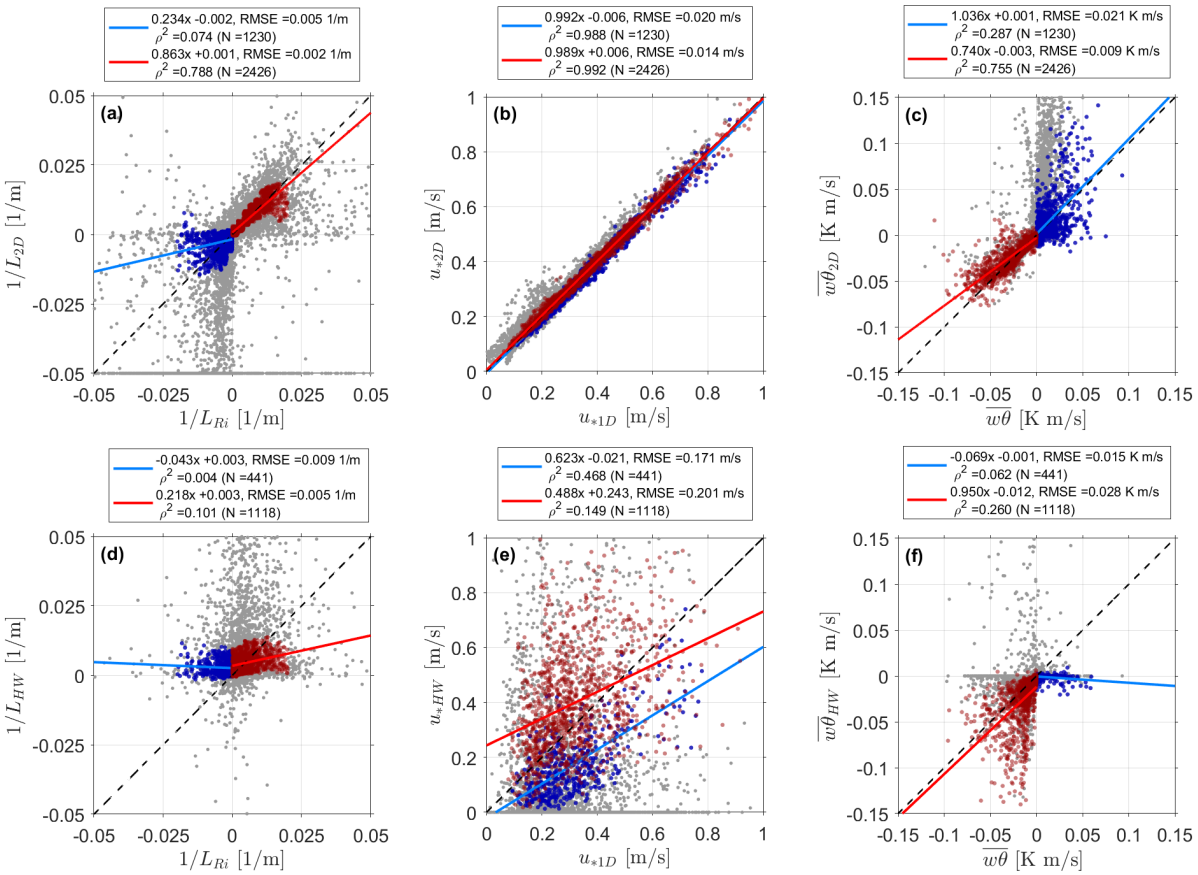

Figure 5.9: (Observational data, Sect. 5.4.3, part II) 2D and HW quantitative retrieval performances (10 min resolution): estimated reciprocal Obukhov length, friction velocity and heat flux against reference metmast retrievals. **(a, b, c)** 2D-algorithm performance. **(d, e, f)** HW-algorithm performance. **(Red and blue dots)** Colour-coded reference Obukhov length as $1/L_{Ri} > 0\ [1/m]$ and $1/L_{Ri} < 0\ [1/m]$, respectively. **(Red and blue lines)** Corresponding regression lines. **(Black-dashed line)** 1:1 ideal reference line. **(Grey dots)** Outlier samples. ρ^2 is the coefficient of determination. N stands for number of samples used in the linear regression. $RMSE$ stands for root-mean-squared error.

assess the friction velocity in the unstable one. Without histogrammed filtering, the HW-retrieved friction velocity results yielded coefficients of determination of $\rho^2 = 0.26$ and $\rho^2 = 0.1$ for the unstable and stable types, respectively, which are virtually the same results as those found with synthetic data at 8% noise level (observational median noise level) in Fig. 5.7b ($\rho^2 = 0.25$ and $\rho^2 = 0.0$, respectively). Note that $u_{*_{sonic}}$ is the *local* friction velocity at 85 m, which might be different from the surface-layer value (Sect. 5.3.3). Therefore, reference sonic-anemometer retrievals closer to the surface would be necessary to increase the validity of our

findings.

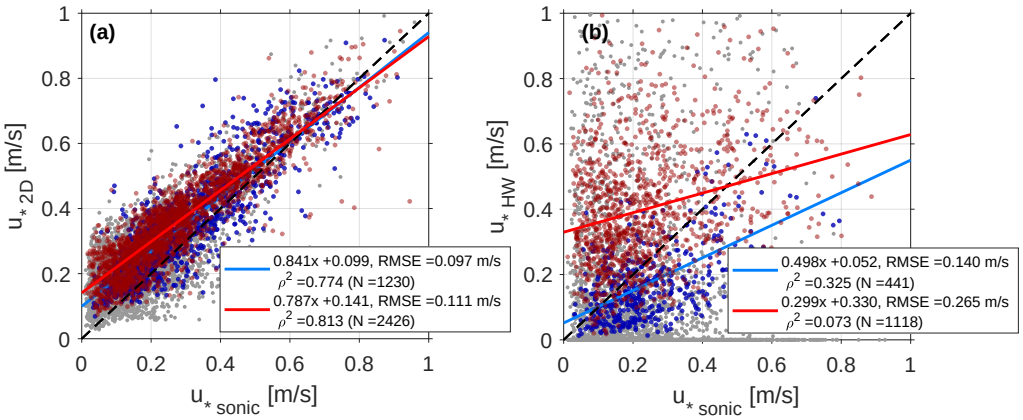

Figure 5.10: (Observational data, Sect. 5.4.3, part III) 2D and HW friction-velocity estimates versus reference sonic-anemometer ones (10 min resolution, Eq. 5.10). (a) 2D estimates. (b) HW estimates. Same format as in Fig. 5.9.

5.5 Summary and conclusions

Two retrieval algorithms aimed at estimating surface-layer parameters from solely wind profiles, namely, the 2D and the Hybrid-Wind methods, were compared. Their performances for estimating the *Obukhov length*, *friction velocity* and *heat flux* were assessed by means of *synthetic* data and *observational* data gathered at the IJmuiden meteorological site.

In order to assess 2D and HW performances with reference to synthetic data, a method to computationally generate surface-layer parameters was devised. By modelling the so-called c-factor (i.e., the proportionality factor between the Obukhov length and the cube of the friction velocity, Eq. 5.11) and the friction velocity as random variables with log-normal-like PDFs, statistically meaningful Obukhov-length and friction-velocity pairs were reproduced (Fig. 5.3). Synthetic noisy wind profiles were generated from these pairs via MOST and the addition of Gaussian perturbational noise to the theoretical MOST profiles. For algorithm intercomparison, 5,000,000 synthetic wind profiles with 20 noise levels spanning from $N_{RMSE} \simeq 0.01\%$ to $N_{RMSE} = 60\%$ were generated.

As for the assessment of 2D and HW performances with reference to observational data, FDWL-measured wind profiles were used as the only input to the algorithms. Reference parameters were retrieved from the metmast instrumentation (Sec. 5.3.3).

Retrieval performance of the 2D and HW methods as a function of the noise level was studied by using both synthetic and observational data. It was found that:

(i) Regarding *synthetic* data, performance results obtained are summarised in Figs. 5.6-5.7. For noise-free synthetic profiles ($N_{RMSE} \rightarrow 0$), the 2D and the HW performed equally. Out of this idealised condition, 2D and HW friction-velocity retrievals were more accurate than Obukhov-length and heat-flux ones (Fig. 5.7). Moreover, neither the 2D nor the HW were able to satisfactorily estimate the Obukhov length (L) or the kinematic heat flux ($\overline{\omega\theta}$) in unstable regimes (Fig. 5.7a,c). Conversely, under stable conditions, the 2D was the only method able to retrieve meaningful Obukhov-length and heat-flux estimates. Overall, the 2D outperformed the HW for the three surface-layer parameters considered.

From a numerical perspective, the smaller errors obtained in the retrieval of the friction velocity by both algorithms (Fig. 5.1) obey to the fact that the MOST model (Eq. 5.1) is very sensitive to the friction velocity. Concerning the HW, there are two key reasons accounting for its poorer performance: First, the HW is a two-step processing algorithm itself, in which a variable Obukhov length is first estimated and, subsequently, a variable friction velocity from the previous Obukhov-length estimate, hence propagating errors. Second, the HW algorithm relies on the MOST assumption of nearly constant momentum and heat fluxes within the surface layer (Stull, 1988), which is used to compute the ratio of the wind-speed differences and, eventually, to estimate the Obukhov length from this ratio (Eq. 5.9). Instead, the 2D algorithm directly fits the MOST wind-profile model to the measured profile, which is equivalent to extrapolating the model up to the highest measurement height.

(ii) Regarding cross-examination with *observational* data, Figs. 5.9–5.10 were in agreement with the results derived from synthetic data (Fig. 5.7), hence validating the representativeness of the latter. Thus, at $N_{RMSE} = 8\%$, which was the observational median noise level in Ijmuiden campaign, 2D friction-velocity retrievals from either observational or synthetic data showed $\rho^2 > 0.9$ under stable and unstable atmospheric conditions (Fig. 5.7b). In contrast, HW friction-velocity retrievals from observational data yielded coefficients of determination of $\rho^2 = 0.1$ (stable) and $\rho^2 = 0.26$ (unstable) [$\rho^2 = 0.15$ *(s)* and $\rho^2 = 0.47$ *(u)* with histogrammed filtering, Fig. 5.9e] versus $\rho^2 = 0.0$ *(s)* and $\rho^2 = 0.25$ *(u)* from synthetic data (Fig. 5.7b). As for the Obukhov-length and heat-flux estimates, the 2D was the only method able to achieve acceptable performance in stable regimes ($\rho^2 \simeq 0.8$). Furthermore, the 2D also prevailed over the HW when comparing their estimates

against reference sonic anemometer measurements or derived Richardson-number approximations (see Sect. 4.3.4) from the sonics (Fig. 5.10 and Fig. 5.9, respectively).

When addressing 2D and HW *atmospheric stability typing performance*, our results are two-fold: On the long time scale (82-day average, i.e., the Ijmuiden campaign duration) observational data showed that both methods output similar median wind-speed profiles for each stability class (Fig. 5.8), the 2D exhibiting narrower error bars. On the short time scale (10-min estimates), observational data (Fig. 5.9a) showed that the 2D method was the only one able to achieve acceptable performance in stable regimes (see point (ii) above).

As far as *data availability* is concerned, it is important to highlight that the 2D method can fit a lidar wind profile with any number of measurement heights whereas the HW is limited to about three. Because of MOST implicit assumption that wind speeds monotonically increase with height, the larger the number of heights, the more likely measurement samples break the monotonicity requirement, therefore, risking to run out of valid MOST-compliant samples.

All in all, we highlight the 2D algorithm as an attractive method for estimating the Obukhov length, friction velocity and turbulent fluxes utilizing only wind-speed profile measurements in and close to the surface layer (25 to 85 m in this work). As further steps, comparisons against momentum and heat flux at lower altitudes (i.e., below 25 m) would be advisable.

Chapter 6

Conclusions and Outlook

Concluding remarks and future research lines concerning the over-land and over-sea dimensions of this Ph.D. are given in the following.

6.1 Conclusions

This PhD thesis focused on the investigation of remote-sensing techniques and retrieval methods for over-land atmospheric boundary-layer and over-sea off-shore surface-layer observation:

I. Over-land dimension.- Regarding the over-land dimension of this work (Chapter 3), this PhD presented a synergistic MLH retrieval algorithm for optimally tracking the ABL diurnal cycle based on combined ceilometer and MWR observations and compared the synergistic performance of the method against the individual performances of the involved instruments and methods in isolation.

MLH retrieval methods using backscattered lidar signals from a ceilometer (Jenoptik CHM-15k Nimbus) and temperature profiles from a Microwave Radiometer (MWR, HATPRO RPG) were compared in terms of their complementary capabilities and associated uncertainties. The Extended Kalman Filter (EKF) was used for MLH retrieval from backscattered lidar signals and the parcel method was used for MLH retrieval from MWR-derived potential-temperature profiles.

The two principal sources of uncertainty in ceilometer-based MLH estimates were: (i) incorrect layer attribution ($\sim$ hundreds of meters) and (ii) noise-induced errors (about 50 m). MWR MLH uncertainties comprised: (i) the total uncertainty in the retrieved potential temperature profile and (ii) ± 0.5 K uncertainty in the surface temperature. Ceilometer- and MWR-based MLH estimates were in turn compared with reference to MLH estimates from radiosoundings. Twenty one measurement days from the HOPE campaign at Jülich, Germany, were considered.

It was shown that the MWR can track the full Mixed Layer (ML) diurnal cycle (i.e., including morning and evening transitions) with height-increasing error bars. The ceilometer-EKF MLH estimates yielded much smaller error bars than those from the MWR under the well-developed clear-sky ML. The ceilometer-EKF is prone to ambiguous tracking some multilayer scenarios (e.g., the residual layer). We therefore introduced the synergistic MLH retrieval approach that combines both ceilometer and MWR estimates in order to optimize the benefits of both.

The SYN method used a maximum likelihood algorithm to combine the MLH-MWR and MLH-LC-EKF methods in order to come up with new estimate (MLH-SYN) that overcame the inherent weaknesses of these two methods in isolation. In summary, the MLH-SYN algorithm makes the most of the fine spatial resolution of the MLH-LC-EKF in the convective time interval, and falls back on the MLH-MWR outside of this interval. In this way, MLH can be tracked automatically and reliably, around the clock.

II. Over-sea dimension.- As far as the off-shore over-sea dimension is concerned (Chapters 4 and 5), this PhD conceived a new method based on MOST, the so-called the 2D parametric-solver algorithm for estimating the Obukhov length (as key atmospheric stability indicator), friction velocity and kinematic heat flux from *solely* floating Doppler wind lidar (FDWL) observations. The PhD also developed a new methodology for studying the sensitivity of the 2D-algorithm retrievals with reference to synthetic and observational data. Specific data-screening procedures were also detailed.

In Chapter 4, the performance of the stability estimates derived from the 2D algorithm was assessed with reference to wind-speed and temperature observations from the IJmuiden metmast (North Sea) during the 82-day campaign of the same name. A fixed-to-mast Doppler wind lidar (DWL) was also available, which provided a reference for wind-speed observations free from sea-motion perturbations.

When comparing FDWL- and mast-derived mean wind speeds, the obtained determination coefficient was as high as that of the fixed-to-mast DWL against the mast ($\rho^2 = 0.996$) with a root mean square error (RMSE) of 0.25 m/s. From the measurement campaign at IJmuiden (10,833 10 min records), the 2D algorithm showed that the atmosphere was neutral (31% of the cases), stable (28%), or near-neutral stable (19%) during the campaign. These figures satisfactorily agreed with values estimated from the mast measurements (31%, 27%, and 19%, respectively).

The procedure to generate synthetic wind profiles was presented in Chapter 5. This High-Performance-Computing procedure generates synthetic noise-corrupted

wind profiles based on estimation of the probability density functions for MOST-related variables (e.g., friction velocity) and the statistics of the noise-corrupting perturbational amplitude found during the IJmuiden observational campaign.

Furthermore, in Chapter 5 the 2D algorithm was compared with the well-known Hybrid-Wind (HW) algorithm by using both synthetic and observational data for their quantitative assessment. Both the HW and the 2D algorithms retrieve surface-layer parameters from only wind-profile observations at different heights. Overall, the 2D algorithm outperformed the HW in the estimation of all the three parameters above (i.e., Obukhov length, friction velocity and heat flux). For instance, when assessing the friction-velocity retrieval performance with reference to sonic anemometers, determination coefficients of $\rho^2_{2D} = 0.77$ and $\rho^2_{HW} = 0.33$ were found under unstable atmospheric stability conditions, and $\rho^2_{2D} = 0.81$ and $\rho^2_{HW} = 0.07$ under stable conditions. Therefore, we highlight the 2D algorithm as an attractive method for estimating these surface-layer parameters utilising only wind-speed profile measurements in and close to the surface layer (25 to 85 m in this work).

All in all, the *over-land dimension* of this Ph.D. thesis showed the importance of synergistic remote-sensing techniques for ABLH estimation, which, when combined with advanced signal-processing techniques such as the Kalman filter and maximum likelihood estimation, provide unprecedented features of high-spatial resolution and high accuracy. The *over-sea dimension* of this thesis successfully demonstrated the potential of FDWLs for offshore wind resource assessment as stand-alone instruments and the ability of specific algorithms (the 2D algorithm) to estimate surface-layer parameters from the FDWL wind-profiles only.

6.2 Outlook

In the *over-land dimension*, future work regarding the MLH synergistic method should extend this methodology over the whole diurnal cycle, particularly during the night-time stable boundary layer. Towards this end, the synergistic approach could be expanded by incorporating other instruments to the standard methodology, for instance, the case of synergistic MLH estimation based on ceilometer, MWR and DWL retrievals. Moreover, it would be advisable to explore the synergy with other pairs of instruments (e.g., ceilometer-DWL, MWR-DWL) according to the observational site availability in order to identify their pros and cons and, therefore, the most robust combination. Not to mention validation in other sites and multi-layer scenarios. In the stable boundary layer, ABLH estimation

blending Kalman-filter predictive analytics with a minimum-variance-based decision threshold is also a prospective line.

As to the *over-sea dimension*, the 2D parametric-solver algorithm should be tested against: (i) direct measurements of both momentum and heat fluxes taken over the same range of heights as those of the FDWL, and (ii) at lower altitudes (i.e., below 25 m) where sonic-anemometer-derived fluxes were available. Application of the 2D method to mast-based wind observations from e.g., FINO-1 or FINO-3, the research platforms in the North Sea, and FINO-2 in the Baltic Sea, would be highly valuable and work is under way.

Furthermore, the methodology developed for the 2D-algorithm could be explored for the onshore case. Nonetheless, that would mean a "3D" formulation instead, in which three MOST wind-model variables rather than two would have to be optimised, namely, friction velocity, Obukhov length and roughness length. The Charnock relation only is valid over the sea.

Appendix A

List of Publications

A.1 Journals

1. **Araújo da Silva, M. P.**, Salcedo-Bosch, A., Rocadenbosch, F., and Peña, A., "On the retrieval of surface-layer parameters from lidar wind-profile measurements". Remote Sens. 2023, Submitted.

2. Salcedo-Bosch, A., Farré-Guarné, J., **Araújo da Silva, M. P.** and Rocadenbosch, F. A Unified Formulation for the Computation of the Six-Degrees-of-Freedom-Motion-Induced Errors in Floating Doppler Wind LiDARs. Remote Sens. 2023, 15, 1478. doi.org/10.3390/rs15061478.

3. **Araújo da Silva, M. P.**, Rocadenbosch, F., Farré-Guarné, J., Salcedo-Bosch, A., González-Marco, D. and Peña, A., "Assessing Obukhov Length and Friction Velocity from Floating Lidar Observations: A Data Screening and Sensitivity Computation Approach". Remote Sens. 2022, 14, 1394. doi.org/10.3390/rs-14061394

4. **Araújo da Silva, M. P.**, Rocadenbosch, F., Tanamachi, R. L., and Saeed, U., "Motivating a synergistic mixing-layer height retrieval method using backscatter lidar returns and microwave radiometer temperature observations," in IEEE Trans. Geosci. Remote Sens., vol. 60, pp. 1-18, 2022, Art no. 4107418, doi:10.1109/TGRS.2022.3158401.

5. de Abreu, L.P., Gonçalves, W.A., Mattos, E.V., Mutti, P.R., Rodrigues, D.T., **Araújo da Silva, M.P.**, "Clouds' Microphysical Properties and Their Relationship with Lightning Activity in Northeast Brazil". Remote Sens. 2021, 13, 4491. doi.org/10.3390/rs13214491.

A.2 International Conferences

1. **Araújo da Silva, M. P.**, Rocadenbosch, F., Salcedo-Bosch, A., and Peña, A., "On the use of wind profiles to assess surface boundary-layer parameters". IGARSS 2023 - 2023 IEEE International Geoscience and Remote Sensing Symposium, Pasadena, CA, USA, 16 - 21 July, 2023. Accepted.

2. **Araújo da Silva, M. P.**, Rocadenbosch, F., Salcedo-Bosch, A., and Peña, A., "Retrieving Monin-Obukhov dimensionless wind shear and stability from floating lidar observations". IGARSS 2023 - 2023 IEEE International Geoscience and Remote Sensing Symposium, Pasadena, CA, USA, 16 - 21 July, 2023. Accepted.

3. Salcedo-Bosch, A., **Araújo da Silva, M. P.**, Rocadenbosch, F., "Atmospheric stability classification from floating doppler wind lidar measurements: a machine learning approach". IGARSS 2023 - 2023 IEEE International Geoscience and Remote Sensing Symposium, Pasadena, CA, USA, 16 - 21 July, 2023. Accepted.

4. **Araújo da Silva, M. P.**, Rocadenbosch, F., Tanamachi, R. L., and Saeed, U., "Synergistic Mixed-Layer Height Retrieval Method Using Microwave Radiometer and Lidar Ceilometer Observations", IGARSS 2022 - 2022 IEEE International Geoscience and Remote Sensing Symposium, Kuala Lumpur, Malaysia, 2022. pp. 6566-6569, doi:10.1109/IGARSS46834.2022.9883098.

5. **Araújo da Silva, M. P.**, Rocadenbosch, F.; Farré-Guarné, J., Salcedo-Bosch, A., González-Marco, D. and Peña, A., "Floating Lidar Assessment of Atmospheric Stability in the North Sea". IGARSS 2022 - 2022 IEEE International Geoscience and Remote Sensing Symposium, Kuala Lumpur, Malaysia, 2022. pp. 7313-7316, doi: 10.1109/IGARSS46834.2022.9883680.

6. **Araújo da Silva, M. P.**, Rocadenbosch, F.; Farré-Guarné, J., Salcedo-Bosch, A., González-Marco, D. and Peña, A., "Offshore atmospheric stability estimation from floating lidar wind profiles" EGU General Assembly 2022, Vienna, Austria, 23–27 May 2022, EGU22-8241, doi.org/10.5194/egusphere-egu22-8241.

7. **Araujo da Silva, M. P.**, Muñoz-Porcar, C., Saeed, U., Rey, F., Pay, M. T., and Rocadenbosch, F. , "On stable boundary-layer height estimation using backscatter lidar data and variance processing", EGU General Assembly 2021,

online, 19–30 Apr 2021, EGU21-8765, 2021 doi.org/10.5194/egusphere-egu21-8765.

8. Muñoz-Porcar, C., **Araujo da Silva, M. P.**, Saeed, U., Rey, F., Pay, M. T., and Rocadenbosch, F., "Variance processing for stable boundary-layer height estimation using backscatter lidar data: a discussion", IGARSS 2021 - 2021 IEEE International Geoscience and Remote Sensing Symposium, Brussels, Belgium, 2021. pp. 8045-8048, doi:10.1109/IGARSS47720.2021.9554707.

9. Villalonga, J., Beveridge, S. L., **Araujo da Silva, M. P.**, Tanamachi, R. L., Rocadenbosch, F., Turner, D. D., and Frasier, S. J. "Convective boundary-layer height estimation from combined radar and Doppler lidar observations in VORTEX-SE," in Remote Sensing of Clouds and the Atmosphere XXV, A. Comerón, E. I. Kassianov, K. Schäfer, R. H. Picard, K. Weber, and U. N. Singh, Eds., vol. 11531, International Society for Optics and Photonics. SPIE, 2020, pp. 115310X, 1-10. [Online]. Available: doi.org/10.1117/12.2576046

10. Rocadenbosch, F., Tanamachi, R. L., **Araujo da Silva, M. P.**, Villalonga, J., Frasier, S. J., and Turner, D. D., "Atmospheric boundary layer height disambiguation using synergistic remote sensing observations: case examples from VORTEX-SE," in Remote Sensing of Clouds and the Atmosphere XXV, A. Comerón, E. I. Kassianov, K. Schäfer, R. H. Picard, K. Weber, and U. N. Singh, Eds., vol. 11531, International Society for Optics and Photonics. SPIE, 2020, pp. 11310L, 1-12. [Online]. Available: doi.org/10.1117/12.2576093

11. Rocadenbosch, F., Tanamachi, R. L., **Araujo da Silva, M. P.**, Villalonga, J., Frasier, S. J., and Turner, D. D., "Atmospheric boundary layer height disambiguation using synergistic remote sensing observations: case examples from VORTEX-SE," in 11 European Conference on Radar in Meteorology & Hidrology, ERAD-2020, 2020, p. 316.

12. Villalonga, J., Beveridge, S. L., **Araujo da Silva, M. P.**, Tanamachi, R. L., Rocadenbosch, F., Turner, D. D., and Frasier, S. J., "Convective boundary-layer height estimation from combined radar and doppler lidar observations in VORTEX-SE," in 11 European Conference on Radar in Meteorology & Hidrology, ERAD-2020, 2020, p. 306.

13. **Araújo da Silva, M. P.**, Salcedo-Bosch, A., Gutierrez-Antunano, M. A., and Rocadenbosch, F. , "Offshore Doppler Wind LiDAR Assessment of Atmospheric Stability," IGARSS 2020 - 2020 IEEE International Geoscience and Remote Sensing Symposium, Waikoloa, HI, USA, 2020, pp. 6081-6084, doi: 10.1109/IGARSS39084.2020.9324044

Appendix B

Measures of central tendency and variability

The mean of the 30-min MLH for the instrument/method combination, X, denoted $\mu_{MLH,X}(t_h)$, is computed at time t_h as

$$\mu_{MLH,X}(t_h) = \frac{1}{N}\sum_{i=1}^{N} MLH_X(t_h, d_i), \tag{B.0.1}$$

where $N = 21$ is the total number of selected days (statistical sample) and d_i denotes the i-th day, $i = 1, \ldots, N$. The variability of the estimated MLH in Eq. (B.0.1) above is computed as the standard deviation over the sample population,

$$\sigma_{MLH,X}(t_h) = \sqrt{\frac{1}{N}\sum_{i=1}^{N} (MLH_X(t_h, d_i) - \mu_{MLH,X}(t_h))^2}. \tag{B.0.2}$$

The mean of the MLH bias (Eq. 3.17) between MLH estimates from two different instruments/datasets denoted X and Y is computed at each time t_h as

$$\mu^{X,Y}_{bias}(t_h) = \frac{1}{N}\sum_{i=1}^{N} bias^{X,Y}(t_h, d_i). \tag{B.0.3}$$

The variability of the MLH bias given by Eq. (B.0.3) above is computed as the standard deviation,

$$\sigma^{X,Y}_{bias}(t_h) = \sqrt{\frac{1}{N}\sum_{i=1}^{N} \left(bias^{X,Y}(t_h, d_i) - \mu^{X,Y}_{bias}(t_h)\right)^2}. \tag{B.0.4}$$

Bibliography

Alblas, L., Bierbooms, W., & Veldkamp, D. (2014). Power output of offshore wind farms in relation to atmospheric stability. *Journal of Physics: Conference Series*, volume 555, 012004.

Araujo da Silva, M. P., Muñoz, C., Saeed, U., Rey, F., Pay, M., & Rocadenbosch, F. (2021). On stable boundary-layer height estimation using backscatter lidar data and variance processing. *EGU General Assembly*. https://doi.org/10.5194/egusphere-egu21-8765

Araújo da Silva, M. P., Rocadenbosch, F., Farré-Guarné, J., Salcedo-Bosch, A., González-Marco, D., & Peña, A. (2022a). Floating lidar assessment of atmospheric stability in the north sea. *IGARSS 2022-2022 IEEE International Geoscience and Remote Sensing Symposium*, 7313–7316. https://doi.org/10.1109/IGARSS46834.2022.9883680

Araújo da Silva, M. P., Rocadenbosch, F., Tanamachi, R. L., & Saeed, U. (2022b). Synergistic mixed-layer height retrieval method using microwave radiometer and lidar ceilometer observations. *IGARSS 2022-2022 IEEE International Geoscience and Remote Sensing Symposium*, 6566–6569. https://doi.org/10.1109/IGARSS46834.2022.9883098

Araújo da Silva, M. P., Rocadenbosch, F., Farré-Guarné, J., Salcedo-Bosch, A., González-Marco, D., & Peña, A. (2022a). Assessing Obukhov length and friction velocity from floating lidar observations: A data screening and sensitivity computation approach. *Remote Sensing*, 14(6). https://doi.org/10.3390/rs14061394

Araújo da Silva, M. P., Rocadenbosch, F., Salcedo-Bosch, A., & Peña, A. (2023). On the retrieval of surface-layer parameters from lidar wind-profile measurements. *Remote Sensing*. Paper under review.

Araújo da Silva, M. P., Rocadenbosch, F., Tanamachi, R. L., & Saeed, U. (2022b). Motivating a synergistic mixing-layer height retrieval method using backscatter lidar returns and microwave-radiometer temperature observations. *IEEE Trans. Geosci. Remote Sens.*, 60, 1–18. https://doi.org/10.1109/TGRS.2022.3158401

Archer, C. L., Colle, B. A., Veron, D. L., Veron, F., & Sienkiewicz, M. J. (2016). On the predominance of unstable atmospheric conditions in the marine boundary layer offshore of the u.s. northeastern coast. *Journal of Geophysical Research: Atmospheres*, 121(15), 8869–8885. https://doi.org/10.1002/2016JD024896

Arranz, P. G. (2011). Measurements in complex terrain using a lidar. Technical report, CENER. Project UpWind:DELIVERABLE D6.6.2.

Banks, R. F., Tiana-Alsina, J., Baldasano, J. M., Rocadenbosch, F., Papayannis, A., Solomos, S., & Tzanis, C. G. (2016). Sensitivity of boundary-layer variables to pbl schemes in the wrf model based on surface meteorological observations, lidar, and radiosondes during the hygra-cd campaign. *Atmospheric Research*, 176-177, 185–201. https://doi.org/https://doi.org/10.1016/j.atmosres.2016.02.024

Banks, R. F., Tiana-Alsina, J., Rocadenbosch, F., & Baldasano, J. M. (2015). Performance evaluation of the boundary-layer height from lidar and the weather research and forecasting model at an urban coastal site in the north-east iberian peninsula. *Boundary-Layer Meteorology*, 157(2), 265–292.

Barlow, R. J. (1989). Errors. *Statistics: A Guide to the Use of Statistical Methods in The Physical Sciences*, (Chapter 4, 48–67). Wiley.

Barrera-Verdejo, M., Crewell, S., Löhnert, U., Orlandi, E., & Girolamo, P. D. (2016). Ground-based lidar and microwave radiometry synergy for high vertical resolution absolute humidity profiling. *Atmospheric Measurement Techniques*, 9(8), 4013–4028.

Barthelmie, R. (1999). The effects of atmospheric stability on coastal wind climates. *Meteorological Applications: A journal of forecasting, practical applications, training techniques and modelling*, 6(1), 39–47.

Basu, S. (2018). A simple recipe for estimating atmospheric stability solely based on surface-layer wind speed profile. *Wind Energy*, 21(10), 937–941.

Basu, S. (2019). Hybrid profile–gradient approaches for the estimation of surface fluxes. *Boundary-layer meteorology*, 170(1), 29–44.

Belegante, L., Nicolae, D., Nemuc, A., Talianu, C., & Derognat, C. (2014). Retrieval of the boundary layer height from active and passive remote sensors. comparison with a nwp model. *Acta Geophysica*, 62(2), 276–289.

Beljaars, A. C. M., Holtslag, A., & Van Westrhenen, R. (1989). *Description of a software library for the calculation of surface fluxes*. KNMI De Bilt, Netherlands.

Berkowicz, R. & Prahm, L. P. (1982). Evaluation of the profile method for estimation of surface fluxes of momentum and heat. *Atmospheric Environment (1967)*, 16(12), 2809–2819.

Boers, R. & Eloranta, E. W. (1986). Lidar measurements of the atmospheric entrainment zone and the potential temperature jump across the top of the mixed layer. *Bound.-Layer Meteor*, 34, 357–375.

Borvarán, D., Peña, A., & Gandoin, R. (2021). Characterization of offshore vertical wind shear conditions in southern new england. *Wind Energy*, 24(5), 465–480.

Businger, J. A., Wyngaard, J. C., Izumi, Y., & Bradley, E. F. (1971). Flux-profile relationships in the atmospheric surface layer. *Journal of Atmospheric Sciences*, 28(2), 181–189.

Campbell Scientific (2016). Zephir 300. Technical report, ZX Lidars, Edmonton, Alberta, Canada.

Carbon Trust (2018). Carbon trust offshore wind accelerator roadmap for the commercial acceptance of floating lidar technology. Technical report, Carbon Trust.

Charnock, H. (1955). Wind stress on a water surface. *Quarterly Journal of the Royal Meteorological Society*, 81(350), 639–640.

Cheynet, E., Jakobsen, J. B., & Obhrai, C. (2017). Spectral characteristics of surface-layer turbulence in the north sea. *Energy Procedia*, 137, 414–427. https://doi.org/https://doi.org/10.1016/j.egypro.2017.10.366. 14th Deep Sea Offshore Wind R&D Conference, EERA DeepWind'2017

Cimini, D., Angelis, F. D., Dupont, J.-C., Pal, S., & Haeffelin, M. (2013). Mixing layer height retrievals by multichannel microwave radiometer observations. *Atmospheric Measurement Techniques*, 6, 4971–4998.

Cimini, D., Haeffelin, M., Kotthaus, S., Löhnert, U., Martinet, P., O'Connor, E., Walden, C., Coen, M. C., & Preissler, J. (2020). Towards the profiling of the atmospheric boundary layer at european scale—introducing the cost action probe. *Bulletin of Atmospheric Science and Technology*, 1, 23–42.

Cimini, D., Hewison, T. J., Martin, L., Güldner, J., Gaffard, C., & Marzano, F. S. (2006). Temperature and humidity profile retrievals from ground based microwave radiometers during tuc. *Meteorol. Z*, 15, 45–56.

Clifton, A., Clive, P., Gottschall, J., Schlipf, D., Simley, E., Simmons, L., Stein, D., Trabucchi, D., Vasiljevic, N., & Würth, I. (2018). Iea wind task 32: Wind lidar identifying and mitigating barriers to the adoption of wind lidar. *Remote Sensing*, 10(3), 406.

Cohn, S. A. & Angevine, W. M. (2000). Boundary layer height and entrainment zone thickness measured by lidars and wind-profiling radars. *Journal of Applied Meteorology*, 39(8), 1233–1247.

Collaud Coen, M., Praz, C., Haefele, A., Ruffieux, D., Kaufmann, P., & Calpini, B. (2014). Determination and climatology of the planetary boundary layer height above the swiss plateau by in situ and remote sensing measurements as well as by the cosmo-2 model. *Atmospheric Chemistry & Physics*, 14(23).

Cornel-Engineering (2023). *Cornel University, Cornel Engineering, Sibley School of Mechanical and Aerospace Engineering*. https://www.mae.cornell.edu/wind-energy-0. (accessed, Feb. 2023)

Council, G. W. E. (2019). Global wind report 2018. Technical report, Global Wind Energy Council, Brussels, Belgium.

CPEX-LAB (2023). *Cloud and precipitation exploration laboratory*. https://atmos.meteo.uni-koeln.de/ag_crewell/doku.php?id=sites:joyce. (accessed, Feb. 2023).

Crewell, S. & Löhnert, U. (2007). Accuracy of boundary layer temperature profiles retrieved with multifrequency multiangle microwave radiometry. *IEEE Transactions on Geoscience and Remote Sensing*, 45, 2195–2201.

de Arruda Moreira, G., Guerrero-Rascado, J. L., Bravo-Aranda, J. A., Benavent-Oltra, J. A., Ortiz-Amezcua, P., Róman, R., Bedoya-Velásquez, A. E., Landulfo, E., & Alados-Arboledas, L. (2018). Study of the planetary boundary layer by

microwave radiometer, elastic lidar and Doppler lidar estimations in southern iberian peninsula. *Atmospheric Research*, 213, 185–195.

de Bruine, M., Apituley, A., Donovan, D. P., Klein Baltink, H., & de Haij, M. J. (2017). Pathfinder: applying graph theory to consistent tracking of daytime mixed layer height with backscatter lidar. *Atmospheric Measurement Techniques*, 10(5), 1893–1909. https://doi.org/10.5194/amt-10-1893-2017

Devroye, L. (2013). *Non-Uniform Random Variate Generation*. Springer New York. https://books.google.co.cr/books?id=9tLcBwAAQBAJ

Dirksen, R., Sommer, M., Immler, F., Hurst, D., Kivi, R., & Vömel, H. (2014). Reference quality upper-air measurements: GRUAN data processing for the Vaisala RS92 radiosonde. *Atmospheric Measurement Techniques*, 7(12).

DTU-Wind (2023). *DTU Wind Energy and Energy Systems*. https://wind.dtu.dk/. (accessed, Feb. 2023)

Dyer, A. J. (1974). A review of flux-profile relationships. *Boundary-Layer Meteorology*, 7(3), 363–372.

Emeis, S. (2010). *Surface-based Remote Sensing of the Atmospheric Boundary Layer*. Springer Science & Business Media.

Emeis, S. & Türk, M. (2009). Wind-driven wave heights in the german bight. *Ocean Dynamics*, 59, 463–475. https://doi.org/10.1007/s10236-008-0178-x

Endlich, R., Ludwig, F., & Uthe, E. (1967). An automatic method for determining the mixing depth from lidar observations. *Atmospheric Environment*, 13, 1051–1056.

Eresmaa, N., Karppinen, A., Joffre, S. M., Räsänen, J., & Talvitie, H. (2006). Mixing height determination by ceilometer. *Atmospheric Chemistry and Physics*, 6, 1485–1493.

Fisher, B. (1998). *Harmonisation of the pre-processing of meteorological data for atmospheric dispersion models*. Office for Official Publications of the European Communities.

Flamant, C., Pelon, J., Flamant, P. H., & Durand, P. (1997). Lidar determination of the entrainment zone thickness at the top of the unstable marine atmospheric boundary-layer. *Bound.-Layer Meteor*, 83, 247–284.

Fritsch, F. N. & Carlson, R. E. (1980). Monotone piecewise cubic interpolation. *SIAM Journal on Numerical Analysis*, 17(2), 238–246.

Fujii, T. & Fukuchi, T. (2005). *Laser Remote Sensing*. CRC Press.

Gao, Z., Qian, X., & Wang, T. (2021). Spectral partition characteristics of wind turbine load response under different atmospheric stability. *Sustainable Energy Technologies and Assessments*, 47, 101421.

Ghaisas, N. S., Archer, C. L., Xie, S., Wu, S., & Maguire, E. (2017). Evaluation of layout and atmospheric stability effects in wind farms using large-eddy simulation. *Wind Energy*, 20(7), 1227–1240.

Göçmen, T., Van der Laan, P., Réthoré, P.-E., Diaz, A. P., Larsen, G. C., & Ott, S. (2016). Wind turbine wake models developed at the technical university of denmark: A review. *Renewable and Sustainable Energy Reviews*, 60, 752–769.

Golbazi, M. & Archer, C. L. (2019). Methods to estimate surface roughness length for offshore wind energy. *Advances in Meteorology*, 2019, 5695481. https://doi.org/10.1155/2019/5695481

Gottschall, J., Wolken-Möhlmann, G., & Lange, B. (2014). About offshore resource assessment with floating lidars with special respect to turbulence and extreme events. *Journal of Physics: Conference Series*, 555(1), 12–43.

Grachev, A. & Fairall, C. (1997). Dependence of the monin–obukhov stability parameter on the bulk richardson number over the ocean. *Journal of Applied Meteorology*, 36(4), 406–414.

Gryning, S.-E., Batchvarova, E., Brümmer, B., Jørgensen, H., & Larsen, S. (2007). On the extension of the wind profile over homogeneous terrain beyond the surface boundary layer. *Boundary-layer meteorology*, 124(2), 251–268.

Güldner, J. & Spänkuch, D. (2001). Remote sensing of the thermodynamic state of the atmospheric boundary layer by ground-based microwave radiometry. *Journal of Atmospheric and Oceanic Technology*, 18, 925–933.

Gutiérrez, M. A., Tiana-Alsina, J., Bischoff, O., Cateura, J., & Rocadenbosch, F. (2015). Performance evaluation of a floating doppler wind lidar buoy in mediterranean near-shore conditions. *Geoscience and Remote Sensing Symposium Proceedings*.

Gutiérrez-Antuñano, M., Tiana-Alsina, J., Salcedo, A., & Rocadenbosch, F. (2018). Estimation of the Motion-Induced Horizontal-Wind-Speed Standard Deviation in an Offshore Doppler Lidar. *Remote Sens.*, 10(12), 2037. https://doi.org/10.3390/rs10122037

Gutiérrez-Antuñano, M. A., Tiana-Alsina, J., & Rocadenbosch, F. (2017). Performance evaluation of a floating lidar buoy in nearshore conditions. *Wind energy*, 20(10), 1711–1726.

Gutierrez-Antunano, M. A., Tiana-Alsina, J., Rocadenbosch, F., Sospedra, J., Aghabi, R., & Gonzalez-Marco, D. (2017). A wind-lidar buoy for offshore wind measurements: First commissioning test-phase results. *2017 IEEE International Geoscience and Remote Sensing Symposium (IGARSS-2017)*, 1607–1610. https://doi.org/10.1109/igarss.2017.8127280

Gutiérrez-Antuñano, M. A. (2019). *Doppler wind LIDAR systems data processing and applications : an overview towards developing the new generation of wind remote-sensing sensors for off-shore wind farms*. Universitat Politècnica de Catalunya.

GWEC (2016). Global wind energy outlook 2016. Technical report, Global Wind Energy Council.

GWEC (2019). Global wind report 2018. Technical report, Global Wind Energy Council.

GWEC (2022). Global wind report 2022. Technical report, Global Wind Energy Council.

Haeffelin, M., Angelini, F., Morille, Y., Martucci, G., Frey, S., Gobbi, G., Lolli, S., O'Dowd, C., Sauvage, L., Xueref-Rémy, I., Wastine, B., & Feist, D. (2012). Evaluation of mixing-height retrievals from automatic profiling lidars and ceilometers in view of future integrated networks in Europe. *Boundary-Layer Meteorology*, 143, 49–75.

Hevia-Koch, P. & Jacobsen, H. (2019a). Comparing offshore and onshore wind development considering acceptance costs. *Energy Policy*, 125, 9–19.

Hevia-Koch, P. & Jacobsen, H. K. (2019b). Comparing offshore and onshore wind development considering acceptance costs. *Energy Policy*, 125, 9–19.

Hogan, R. J., Grant, A. L. M., Illingworth, A. J., Pearson, G. N., & O'Connor, E. J. (2009). Vertical velocity variance and skewness in clear and cloud-topped boundary layers as revealed by Doppler lidar. *Quarterly Journal of the Royal Meteorological Society*, 135(640), 635–643.

Högström, U. (1988). Non-dimensional wind and temperature profiles in the atmospheric surface layer: A re-evaluation. *Topics in Micrometeorology. A Festschrift for Arch Dyer*, 55–78. Springer.

Holtslag, M. C., Bierbooms, W. A. A. M., & Van Bussel, G. J. W. (2014). Estimating atmospheric stability from observations and correcting wind shear models accordingly. *Journal of Physics: Conference Series*, volume 555, 012052.

Holtslag, M. C., Bierbooms, W. A. A. M., & Van Bussel, G. J. W. (2015). Validation of surface layer similarity theory to describe far offshore marine conditions in the dutch north sea in scope of wind energy research. *Journal of Wind Engineering and Industrial Aerodynamics*, 136, 180–191.

Holtslag, M. C., Bierbooms, W. A. A. M., & Van Bussel, G. J. W. (2016). Wind turbine fatigue loads as a function of atmospheric conditions offshore. *Wind Energy*, 19(10), 1917–1932.

Holzworth, G. (1964). Estimates of mean maximum mixing depths in the contiguous United States. *Monthly Weather Review*, 92, 235–242.

Hooper, W. P. & Eloranta, E. W. (1986). Lidar measurements of wind in the planetary boundaryndary layer: The method, accuracy and results from joint measurements with radiosonde and Kytoon. *J. Climate Appl. Meteor*, 25, 990–100.

IEA-Wind (2023). *International energy agency wind technology collaboration programme - Task 52*. https://iea-wind.org/task52/

IRENA (2019). Future of Wind: Deployment, investment, technology, grid integration and socio-economic aspects. Technical report, International Renewable Energy Agency, Abu Dhabi.

Kahaner, D., Moler, C., & Nash, S. (1989). *Numerical methods and software*. Prentice-Hall, Inc.

Kalman, R. E. (1960). A New Approach to Linear Filtering and Prediction Problems. *Journal of Basic Engineering*, 82(1), 35–45. https://doi.org/10.1115/1.3662552

Kelberlau, F., Neshaug, V., Lønseth, L., Bracchi, T., & Mann, J. (2020). Taking the Motion out of Floating Lidar: Turbulence Intensity Estimates with a Continuous-Wave Wind Lidar. *Remote Sens.*, 12(898).

Kelly, M. (2021). Direct solution of various micrometeorological problems via the lambert-w function. *Boundary-Layer Meteorology*, 179(1), 163–168. https://doi.org/10.1007/s10546-020-00592-z

Kim, D.-Y., Kim, Y.-H., & Kim, B.-S. (2021). Changes in wind turbine power characteristics and annual energy production due to atmospheric stability, turbulence intensity, and wind shear. *Energy*, 214, 119051. https://doi.org/https://doi.org/10.1016/j.energy.2020.119051

Klug, W. (1967). Determination of turbulent fluxes of heat and momentum from the wind profile. *Quarterly Journal of the Royal Meteorological Society*, 93(395), 101–104.

Kotthaus, S., Bravo-Aranda, J. A., Collaud Coen, M., Guerrero-Rascado, J. L., Costa, M. J., Cimini, D., O'Connor, E. J., Hervo, M., Alados-Arboledas, L., Jiménez-Portaz, M., et al. (2022). Atmospheric boundary layer height from ground-based remote sensing: a review of capabilities and limitations. *Atmospheric Measurement Techniques Discussions*, 1–88.

Kretschmer, M., Schwede, F., Guzmán, R. F., Lott, S., & Cheng, P. (2018). Influence of atmospheric stability on the load spectra of wind turbines at alpha ventus. *Journal of Physics: Conference Series*, volume 1037, 052009.

Lange, B., Larsen, S., Højstrup, J., & Barthelmie, R. (2004). Importance of thermal effects and sea surface roughness for offshore wind resource assessment. *Journal of wind engineering and industrial aerodynamics*, 92(11), 959–988.

Lange, D., Rocadenbosch, F., Tiana-Alsina, J., & Frasier, S. (2015). Atmospheric boundary-layer-height estimation using a Kalman filter and a frequency-modulated continuous-wave radar returns. *IEEE Transactions on Geoscience and Remote Sensing*, 53, 3338–3349.

Lange, D., Tiana-Alsina, J., Saeed, U., Tomás, S., & Rocadenbosch, F. (2014). Atmospheric-boundary-layer height monitoring using a Kalman filter and backscatter lidar returns. *IEEE Transactions on Geoscience and Remote Sensing*, 52(8), 4717–4728.

LeMone, M. A., Angevine, W. M., Bretherton, C. S., Chen, F., Dudhia, J., Fedorovich, E., Katsaros, K. B., Lenschow, D. H., Mahrt, L., Patton, E. G., Sun, J., Tjernström, M., & Weil, J. (2018). 100 years of progress in boundary layer meteorology. *Meteorological Monographs*, 59, 9.1–9.85.

Lenschow, D., Wyngaard, J. C., & Pennell, W. T. (1980). Mean-field and second-moment budgets in a baroclinic, convective boundary layer. *Journal of the Atmospheric Sciences*, 37(6), 1313–1326.

Lo, A. K. (1979). On the determination of boundary-layer parameters using velocity profile as the sole information. *Boundary-Layer Meteorology*, 17, 465–484.

Löhnert, U. & Crewell, S. (2003). Accuracy of cloud liquid water path from ground-based microwave radiometry - Part I: Dependency on cloud model statistics and precipitation. *Radio Science*, 38(3). https://doi.org/https://doi.org/10.1029/2002RS002654

Löhnert, U. & Maier, O. (2012). Operational profiling of temperature using ground-based microwave radiometry at Payerne: Prospects and challenges. *Atmospheric Measurement Techniques*, 5, 1121–1134.

Löhnert, U., Schween, J., Acquistapace, C., Ebell, K., Maahn, M., Barrera-Verdejo, M., Hirsikko, A., Bohn, B., Knaps, A., O'connor, E., et al. (2015a). Joyce: Jülich observatory for cloud evolution. *Bulletin of the American Meteorological Society*, 96(7), 1157–1174.

Löhnert, U., Schween, J. H., Acquistapace, C., Ebell, K., Maahn, M., Barrera-Verdejo, M., Hirsikko, A., Bohn, B., Knaps, A., O'Connor, E., Simmer, C., Wahner, A., & Crewell, S. (2015b). JOYCE: Jülich Observatory for Cloud Evolution. *Bulletin of the American Meteorological Society*, 96(7), 1157–1174.

Lopez-Villalobos, C., Martínez-Alvarado, O., Rodriguez-Hernandez, O., & Romero-Centeno, R. (2022). Analysis of the influence of the wind speed profile on wind power production. *Energy Reports*, 8, 8079–8092. https://doi.org/https://doi.org/10.1016/j.egyr.2022.06.046

Löhnert, U., Crewell, S., & Simmer, C. (01 Sep. 2004). An integrated approach toward retrieving physically consistent profiles of temperature, humidity, and cloud liquid water. *Journal of Applied Meteorology*, 43(9), 1295 – 1307. https://doi.org/10.1175/1520-0450(2004)043⟨1295:AIATRP⟩2.0.CO;2

Löhnert, U., Turner, D. D., & Crewell, S. (01 May. 2009). Ground-based temperature and humidity profiling using spectral infrared and microwave observations. part i: Simulated retrieval performance in clear-sky conditions. *Journal of Applied Meteorology and Climatology*, 48(5), 1017 – 1032. https://doi.org/10.1175/2008JAMC2060.1

Machefaux, E., Larsen, G. C., Koblitz, T., Troldborg, N., Kelly, M. C., Chougule, A., Hansen, K. S., & Rodrigo, J. S. (2016). An experimental and numerical study of the atmospheric stability impact on wind turbine wakes. *Wind Energy*, 19(10), 1785–1805.

MacIsaac, C. & Naeth, S. (2013). Triaxys next wave ii directional wave sensor the evolution of wave measurements. *2013 OCEANS - San Diego*, 1–8.

Macke, A., Seifert, P., Baars, H., Barthlott, C., Beekmans, C., Behrendt, A., Bohn, B., Brueck, M., Bühl, J., Crewell, S., Damian, T., Deneke, H., Düsing, S., Foth, A., Girolamo, D., P., H., E., H., R., H., A., K., J., K., N., K., S., K., M., L., U., M., L., B., Maurer, V., Muppa, S. K., Schween, J., Serikov, I., Siebert, H., Simmer, C., Späth, F., Steinke, S., Träumner, K., Trömel, S., Wehner, B., Wieser, A., Wulfmeyer, V., & Xie, X. (2017). The HD(CP)^2 Observational Prototype Experiment (HOPE) – an overview. *Atmospheric Chemistry and Physics*, 17, 4887–4914.

Mathisen, J. P. (2013). Measurement of wind profile with a buoy mounted lidar. *Energy Procedia*, 00(00), 12.

Measures, R. M. (1992). Laser-remote sensor equations. *Laser Remote Sensing: Fundamentals and Applications*, (Chapter 7, 237–280). John Wiley & Sons.

Melfi, S. H., Spinhirne, J. D., Chou, S.-H., & Palm, S. P. (1985). Lidar observations of vertically organized convection in the planetary boundary layer over the ocean. *J. Climate Appl. Meteor*, 24, 806–821.

Menut, L., Flamant, C., Pelon, J., & Flamant, P. H. (1999). Urban boundary-layer height determination from lidar measurements over the paris area. *Appl. Opt*, 38, 945–954.

Monin, A. S. & Obukhov, A. M. (1954). Basic laws of turbulent mixing in the surface layer of the atmosphere. *Contrib. Geophys. Inst. Acad. Sci. USSR*, 151(163), e187.

Motta, M., Barthelmie, R. J., & Vølund, P. (2005). The influence of non-logarithmic wind speed profiles on potential power output at danish offshore sites. *Wind Energy: An International Journal for Progress and Applications in Wind Power Conversion Technology*, 8(2), 219–236.

Msigwa, G., Ighalo, J. O., & Yap, P.-S. (2022). Considerations on environmental, economic, and energy impacts of wind energy generation: Projections towards sustainability initiatives. *Science of the Total Environment*, 157755.

Münkel, C., Eresmaa, N., Räsänen, J., & Karppinen, A. (2007). Retrieval of mixing height and dust concentration with lidar ceilometer. *Boundary-Layer Meteorology*, 124(1), 117–128.

Muñoz-Porcar, C., Araujo da Silva, M., Saeed, U., Rey, F., Pay, M. T., & Rocadenbosch, F. (2021). Variance processing for stable boundary-layer height estimation using backscatter lidar data: A discussion. *2021 IEEE International Geoscience and Remote Sensing Symposium IGARSS*, 8045–8048.

Nicholls-Lee, R. (2013). A low motion floating platform for offshore wind resource assessment using lidars. *International Conference on Offshore Mechanics and Arctic Engineering*, volume 55423, V008T09A036.

O'Connor, E. J., Illingworth, A. J., Brooks, I. M., Westbrook, C. D., Hogan, R. J., Davies, F., & Brooks, B. J. (2010). A method for estimating the turbulent kinetic energy dissipation rate from a vertically pointing Doppler lidar, and independent evaluation from balloon-borne in situ measurements. *Journal of Atmospheric and Oceanic Technology*, 27(10), 1652–1664.

Panofsky, H. A. (1973). Tower micrometeorogy. *Haugeb DA (ed) Workshop on Micrometeorolgy, American Meteorology Society*, 151—176

Pearson, G., Davies, F., & Collier, C. (2010). Remote sensing of the tropical rain forest boundary layer using pulsed Doppler lidar. *Atmospheric Chemistry and Physics*, 10, 5891–5901.

Pearson, G. N. & Collier, C. G. (1999). A pulsed coherent CO2 lidar for boundary-layer meteorology. *Quarterly Journal of the Royal Meteorological Society*, 125(559), 2703–2721.

Peña, A. & Gryning, S.-E. (2008). Charnock's roughness length model and non-dimensional wind profiles over the sea. *Boundary-layer meteorology*, 128(2), 191–203.

Peña, A., Gryning, S.-E., & Hasager, C. B. (2008). Measurements and modelling of the wind speed profile in the marine atmospheric boundary layer. *Boundary-layer meteorology*, 129(3), 479–495.

Peña, A., Hasager, C., Lange, J., Anger, J., Badger, M., Bingöl, F., Bischoff, O., Cariou, J.-P., Dunne, F., Emeis, S., Harris, M., Hofsäss, M., Karagali, I., Laks, J., Larsen, S., Mann, J., Mikkelsen, T., Pao, L., Pitter, M., Rettenmeier, A., Sathe, A., Scanzani, F., Schlipf, D., Simley, E., Slinger, C., Wagner, R., & Würth, I. (2013). *Remote Sensing for Wind Energy*. DTU Wind Energy.

Peña, A., Hasager, C. B., Gryning, S. E., Courtney, M., Antoniou, I., & Mikkelsen, T. (2009). Offshore wind profiling using light detection and ranging measurements. *Wind Energy*, 12, 105–124.

Peña, A., Mann, J., Angelou, N., & Jacobsen, A. (2022). A motion-correction method for turbulence estimates from floating lidars. *Remote Sensing*, 14(23), 6065.

Pichugina, Y., Banta, R., Brewer, W., Sandberg, S., & Hardesty, R. (2012). Doppler lidar–based wind-profile measurement system for offshore wind-energy and other marine boundary layer applications. *J. Appl. Meteorol. Climatol*, 51(2), 327–349. https://doi.org/10.1175/JAMC-D-11-040.1

Poltera, Y., Martucci, G., Collaud Coen, M., Hervo, M., Emmenegger, L., Henne, S., Brunner, D., & Haefele, A. (2017). Pathfinderturb: an automatic boundary layer algorithm. development, validation and application to study the impact on in situ measurements at the jungfraujoch. *Atmospheric Chemistry and Physics*, 17(16), 10051–10070. https://doi.org/10.5194/acp-17-10051-2017

Reif, K., Gunther, S., Yaz, E., & Unbehauen, R. (1999). Stochastic stability of the discrete-time extended kalman filter. *IEEE Transactions on Automatic Control*, 44(4), 714–728. https://doi.org/10.1109/9.754809

Rocadenbosch, F. (2003). Lidar-wind, raman, and other sensing. *Encyclopedia of optical engineering*, 1114–1127. Marcel Dekker.

Rocadenbosch, F., Barragán, R., Frasier, S. J., Waldinger, J., Turner, D. D., Tanamachi, R. L., & Dawson, D. T. (2020). Ceilometer-based rain-rate estimation: A case-study comparison with s-band radar and disdrometer retrievals in the context of vortex-se. *IEEE Transactions on Geoscience and Remote Sensing*, 58(12), 8268–8284. https://doi.org/10.1109/TGRS.2020.2984458

Rocadenbosch, F., Soriano, C., Comerón, A., & Baldasano, J. (1999). Lidar inversion of atmospheric backscatter and extinction-to-backscatter ratios by use of a Kalman filter. *Applied Optics*, 38, 3175–3189.

Rocadenbosch, F., Tanamachi, R. L., Araujo da Silva, M. P., Villalonga, J., Frasier, S. J., & Turner, D. D. (2020). Atmospheric boundary layer height disambiguation using synergistic remote sensing observations: case examples from VORTEX-SE. *Remote Sensing of Clouds and the Atmosphere XXV*, volume 11531, 115310L, 1–12. https://doi.org/10.1117/12.2576093

Rose, T., Crewell, S., Löhnert, U., & Simmer, C. (2005). A network suitable microwave radiometer for operational monitoring of the cloudy atmosphere. *Atmospheric Research*, 75, 183–200.

RPG (2023). *Rpg-radiometer physics gmbh - technical instrument manual*. https://www.radiometer-physics.de/downloadftp/pub/PDF/Radiometers/General_documents/Manuals/2015/RPG_MWR_STD_Technical_Manual_2015.pdf. (accessed, Feb. 2023).

Saeed, U. (2016). *Atmospheric-Boundary-Layer Height Retrieval using Microwave Radiometer and Lidar Sensors: Algorithms and Error Estimation*. Universitat Politècnica de Catalunya.

Salcedo-Bosch, A. (2020). Wind LIDAR (laser radar) remote sensing: Application to the off-shore wind energy. Universitat Politècnica de Catalunya.

Salcedo-Bosch, A., Farré-Guarné, J., Sala-Álvarez, J., Villares-Piera, J., Rocadenbosch, F., & Tanamachi, R. L. (2021a). Floating doppler wind lidar simulator for horizontal wind speed measurement error assessment. *2021 IEEE International Geoscience and Remote Sensing Symposium (IGARSS-2021)*. Presented.

Salcedo-Bosch, A., Gutierrez-Antunano, M. A., Tiana-Alsina, J., & Rocadenbosch, F. (2020). Floating Doppler wind lidar measurement of wind turbulence: a cluster analysis. *2020 IEEE International Geoscience and Remote Sensing Symposium (IGARSS-2020)*.

Salcedo-Bosch, A., Rocadenbosch, F., Gutiérrez-Antuñano, M. A., & Tiana-Alsina, J. (2021b). Estimation of wave period from pitch and roll of a lidar buoy. *Sensors*, 21(4). https://doi.org/10.3390/s21041310

Salcedo-Bosch, A., Rocadenbosch, F., & Sospedra, J. (2021c). A robust adaptive unscented kalman filter for floating doppler wind-lidar motion correction. *Remote Sensing*, 13(20). https://doi.org/10.3390/rs13204167

Sathe, A., Gryning, S.-E., & Peña, A. (2011). Comparison of the atmospheric stability and wind profiles at two wind farm sites over a long marine fetch in the north sea. *Wind Energy*, 14(6), 767–780.

Sathe, A. & Mann, J. (2013). A review of turbulence measurements using ground-based wind lidars. *Atmospheric Measurement Techniques*, 6(11), 3147–3167. https://doi.org/10.5194/amt-6-3147-2013

Sathe, A., Mann, J., Barlas, T., Bierbooms, W., & Van Bussel, G. (2013). Influence of atmospheric stability on wind turbine loads. *Wind Energy*, 16(7), 1013–1032.

Schuon, F., González, D., Rocadenbosch, F., Bischoff, O., & Jané, R. (2012). KIC InnoEnergy Project Neptune: Development of a Floating LiDAR Buoy for Wind, Wave and Current Measurements. *Proceedings DEWEK 2012 German Wind Energy Conference*.

Schween, J. H., Hirsikko, A., Löhnert, U., & Crewell, S. (2014). Mixing-layer height retrieval with ceilometer and Doppler lidar: from case studies to long-term assessment. *Atmospheric Measurement Techniques*, 7(11), 3685–3704. https://doi.org/10.5194/amt-7-3685-2014

Seibert, P., Beyrich, F., Gryning, S.-E., Joffre, S., Rasmussen, A., & Tercier, P. (2000). Review and intercomparison of operational methods for the determination of the mixing height. *Atmospheric Environment*, 34, 1352–2310.

Seidel, D. J., Ao, C. O., & Li, K. (2010). Estimating climatological planetary boundary layer heights from radiosonde observations: Comparison of methods and

uncertainty analysis. *Journal of Geophysical Research: Atmospheres*, 115(D16). https://doi.org/https://doi.org/10.1029/2009JD013680

Senff, C., Bösenberg, J., Peters, G., & Chaberl, T. S. (1996). Remote sensing of turbulent ozone fluxes and the ozone budget in the convective boundary layer with dial and radar-rass: a case study. *Contributions to Atmospheric Physics/Beitraege zur Physik der Atmosphaere*, 61(9), 161–176.

Stull, R. (2017). *Practical Meteorology: an algebra-based survey of atmospheric science*. Univ. of British Columbia. https://www.eoas.ubc.ca/books/Practical_Meteorology/

Stull, R. B. (1988). *An introduction to boundary layer meteorology*, volume 13. Springer Science & Business Media.

Stull, R. B. (2015). *Practical meteorology: an algebra-based survey of atmospheric science*. University of British Columbia.

Subramanian, B., Chokani, N., & Abhari, R. S. (2018). Impact of atmospheric stability on wind turbine wake evolution. *Journal of Wind Engineering and Industrial Aerodynamics*, 176, 174–182.

Swinbank, W. (1964). The exponential wind profile. *Quarterly Journal of the Royal Meteorological Society*, 90(384), 119–135.

Tanamachi, R. L., Frasier, S. J., Waldinger, J., LaFleur, A., Turner, D. D., & Rocadenbosch, F. (2019). Progress toward characterization of the atmospheric boundary layer over northern alabama using observations by a vertically pointing, s-band profiling radar during vortex-southeast. *Journal of Atmospheric and Oceanic Technology*, 36(11), 2221–2246.

Tiana-Alsina, J., Rocadenbosch, F., & Gutierrez-Antunano, M. A. (2017). Vertical Azimuth Display simulator for wind-Doppler lidar error assessment. *2017 IEEE International Geoscience and Remote Sensing Symposium (IGARSS)*, 1614–1617. https://doi.org/10.1109/igarss.2017.8127282

Träumner, K., Kottmeier, C., Corsmeier, U., & Wieser, A. (2011). Convective boundary-layer entrainment: Short review and progress using Doppler lidar. *Boundary-Layer Meteorology*, 141(3), 369–391.

TRIAXYS (2018). *Triaxys^{TM} wave & current buoy*. Retrieved from https://axys.com/triaxys-wave-current-buoy/. (Accessed on 24/02/2023).

Tucker, S. C., Senff, C. J., Weickmann, A. M., Brewer, W. A., Banta, R. M., Sandberg, S. P., Law, D. C., & Hardesty, R. M. (2009). Doppler lidar estimation of mixing height using turbulence, shear, and aerosol profiles. *Journal of Atmospheric and Oceanic Technology*, 26(4), 673–688.

Türk, M. & Emeis, S. (2010). The dependence of offshore turbulence intensity on wind speed. *Journal of Wind Engineering and Industrial Aerodynamics*, 98(8-9), 466–471.

Tzadok, T., Ronen, A., Rostkier-Edelstein, D., Agassi, E., Avisar, D., Berkovic, S., & Manor, A. (2022). Profiling the planetary boundary layer wind with a streamline xr doppler lidar: Comparison to in-situ observations and wrf model simulations. *Remote Sensing*, 14(17), 4264.

UMass (2023). *University of Massachusetts Wind Energy Center*. https://www.umass.edu/windenergy/home. (accessed, Feb. 2023)

Van Wijk, A., Beljaars, A., Holtslag, A., & Turkenburg, W. (1990). Evaluation of stability corrections in wind speed profiles over the north sea. *Journal of Wind Engineering and Industrial Aerodynamics*, 33(3), 551–566.

Vickers, D., Mahrt, L., & Andreas, E. L. (2015). Formulation of the sea surface friction velocity in terms of the mean wind and bulk stability. *Journal of Applied Meteorology and Climatology*, 54(3), 691 – 703. https://doi.org/10.1175/JAMC-D-14-0099.1

Villalonga, J. (2020). Atmospheric remote sensing and adaptive processing: Boundary-layer radar observation in the context of U.S. VORTEX project. Universitat Politècnica de Catalunya.

Villalonga, J., Beveridge, S. L., Araujo da Silva, M. P., Tanamachi, R. L., Rocadenbosch, F., Turner, D. D., & Frasier, S. J. (2020). Convective boundary-layer height estimation from combined radar and Doppler lidar observations in VORTEX-SE. *Remote Sensing of Clouds and the Atmosphere XXV*, volume 11531, 115310X, 1–10. https://doi.org/10.1117/12.2576046

Wagner, R., Mikkelsen, T., & Courtney, M. (2009). Investigation of turbulence measurements with a continuous wave, conically scanning lidar. Technical report, DTU.

Wagner, T. J., Klein, P. M., & Turner, D. D. (2019). A new generation of ground-based mobile platforms for active and passive profiling of the boundary layer. *Bulletin of the American Meteorological Society*, 100(1), 137–153. https://doi.org/10.1175/BAMS-D-17-0165.1

Wallace, J. M. & Hobbs, P. V. (2006a). 3 - Atmospheric Thermodynamics. *Atmospheric Science (Second Edition)*, 78. Academic Press, (second edition ed.). https://doi.org/https://doi.org/10.1016/B978-0-12-732951-2.50008-9

Wallace, J. M. & Hobbs, P. V. (2006b). *Atmospheric Science: An Introductory Survey*. Elsevier.

Weitkamp, C. (2006). *Lidar: range-resolved optical remote sensing of the atmosphere*, volume 102. Springer Science & Business.

Werkhoven, E. J. & Verhoef, J. P. (2012). Offshore Meteorological Mast IJmuiden: Abstract of Instrumentation Report. Technical report, Energy Research Centre of the Netherlands (ECN). https://www.windopzee.net/wp-content/uploads/2019/07/ecn-wind_memo-12-010_abstract_of_instrumentatierapport_meetmast_ijmuiden.pdf

Wharton, S. & Lundquist, J. (2012). Assessing atmospheric stability and its impacts on rotor-disk wind characteristics at an onshore wind farm. *Wind Energy*, 15, 525–546. https://doi.org/10.1002/we.483

Wiener, N. (1964). *Extrapolation, Interpolation, and Smoothing of Stationary Time Series*. The MIT Press.

WindEurope (2020). Offshore wind in Europe key trends and statistics 2019. Technical report, WindEurope, Brussels, Belgium.

WindPower (2018). *Do we still need met masts?* Retrieved from https://www.windpowermonthly.com/article/1458018/need-met-masts. (Accessed on 06/04/2021).

Wingo, S. & Knupp, K. (2015). Multi-platform observations characterizing the afternoon-to-evening transition of the planetary boundary layer in northern alabama, usa. *Boundary-Layer Meteor*, 155, 29–53.

Wulfmeyer, V., Hardesty, R. M., Turner, D. D., Behrendt, A., Cadeddu, M. P., Di Girolamo, P., Schlüssel, P., Van Baelen, J., & Zus, F. (2015). A review of the remote sensing of lower tropospheric thermodynamic profiles and its indispensable role for the understanding and the simulation of water and energy cycles. *Reviews of Geophysics*, 53(3), 819–895. https://doi.org/https://doi.org/10.1002/2014RG000476

Xu, G., Xi, B., Zhang, W., Cui, C., Dong, X., Liu, Y., & Yan, G. (2015). Comparison of atmospheric profiles between microwave radiometer retrievals and radiosonde soundings. *Journal of Geophysical Research: Atmospheres*, 120(19), 10,313–10,323. https://doi.org/https://doi.org/10.1002/2015JD023438

Zhang, S. F. (1981). Comments on 'on the determination of boundary-layer parameters using velocity profile as the sole information' by lo (1979). *Boundary-Layer Meteorology*, 21, 127–129.

ZX-Lidars (2023). *ZX 300 onshore wind lidar*. Retrieved from https://www.zxlidars.com/wind-lidars/zx-300/. (Accessed on 24/02/2023).